A STUDY OF THE LOCALIZED AND COLLECTIVE EFFECTS IN MAGNETICALLY ORDERED SYSTEMS

by

Lit-Kwan Leung

A thesis submitted to the Faculty of Graduate Studies of the University of Manitoba in partial fulfilment of the requirements for the degree of Doctor of Philosophy.

Winnipeg: 15th March, 1972.

to my parents

PREFACE

In solid state physics, there are two main approaches to describe the outer electrons in solids, namely crystal field theory and band theory, which describe localized and collective phenomena respectively. The applicability of these theories to any solid depends on mainly its physical characteristics. In this thesis, an attempt is made to examine the magnetic behavior of some systems which can be adequately described by one or a combination of these two theories. The experimental methods fall roughly into two categories. Firstly, measurements were made of the following macroscopic properties: electrical resistivity, using the conventional four-probe method, and magnetization and Curie temperature using a vibrating sample magnetometer. Secondly, Nuclear Magnetic Resonance (NMR) and Mössbauer techniques are used in probing the microscopic behavior.

In chapter I, a brief introduction to the magnetic exchange interactions applicable to this study is given. Chapter II is devoted to the system $La_{1-X}Pb_XMnO_3$ with $0.26 \leq X \leq 0.44$, and concerns its single crystal growth, structure determination, magnetization, Curie temperature, and NMR spectra. Chapter III describes the results of Mössbauer, NMR and other measurements on this system with various amounts of Fe^{57} substituted for Mn. Chapter IV concerns a different(but related spin structure)

system $Ni_{1-x}Zn_xFe_2O_4$. Here Mössbauer spectra with and without an external field are reported and discussed. Finally a summary of the more important findings is given in the last chaper.

I am grateful to my supervisor, Professor A. H. Morrish for the many precious hours he had given up in our numerous discussions and the guidance and encouragement during this study. In the early stage of this study, I collaborated with Professor C. W. Searle in the magnetization measurement, and Dr. B. J. Evans in the Mössbauer work. To them I am extending my gratitude for their assistance in setting up the experiments as well as their valuable suggestions. Thanks are also due to Dr. A. Hirai during his visit here from Kyoto University for the help in NMR measurement. I am also grateful to my fellow graduate students and staff members for their help and advice. In particular, I wish to mention Mr. G. Dean, Dr. D. C. Price and Mr. J. Davis.

Since June 1967 when the research was started, I have received financial support from the University of Manitoba through assistantship and fellowship, and the Defence Research Board of Canada through the grant of my supervisor.

Finally, I would like to express my gratitude to my wife, Grace, for her patience and encouragement during the entire period of this study. The excellent typing was also done by her.

CONTENTS

ABSTRACT

In this thesis we report on experiments with three compounds of the iron transition group. It is suggested that the 3d electrons are responsible for the magnetic and electrical properties which differ greatly depending on whether the character of the 3d electrons is collective or localized.

Single crystals of $La_{1-X}Pb_XMnO_3$ with $0.26 \leq X \leq 0.44$ have been grown by the flux technique. X-ray fluorescence, wet chemical, and electron microprobe analyses indicate the crystals are homogeneous and stoichiometric. The crystal structure was determined to be a rhombohedrally distorted perovskite with double cell edges. The static magnetization has been measured from close to absolute zero to about $800^{\circ}K$. The compounds are ferromagnetic, with Curie temperatures ranging from 315 to $350^{\circ}K$. At absolute zero, the magnetization agrees to within 3% of that expected from the average spin per formula unit. The spontaneous magnetization decreases more rapidly than predicted by the Brillouin function for a normal ferromagnet for $0.9 < T/T_c < 1$. Just above the Curie temperature, the reciprocal susceptibility versus temperature curve exhibits a slight curvature; at higher temperatures, the susceptibility follows the Curie-Weiss Law. The average spin obtained from the Curie constant agrees well with that obtained from the chemical formula. The conductivity determined with the conventional four-probe method is of the order of $\sim 10^2$ mho/cm. Together with the compelling fact of the thermal coefficient of the resistivity below T_c determined by

Searle and Wang, we conclude that the ferromagnetism has its origin primarily in the itinerant d-electrons that lie in a narrow double-exchange band. In other words, the outer d-electrons have a collective behavior. This fact is further supported by the Mn^{55} NMR result which shows a single absorption line and this is identified to associate with neither Mn^{3+} nor Mn^{4+} ions but an average of the two ions.

With Fe substitution into the system, the magnetization is found to be lower and is explicable if the Fe spin can be assumed to be antiparallel to the Mn spin. The Curie temperature is greatly suppressed. A linear extrapolation of the saturation magnetization for different substitutions suggests that system ceases to be ferromagnetic at about 45 atomic percent substitution. The Fe^{57} Mössbauer results confirm the antiparallel spin arrangement between the Mn and Fe spins, but this is only true when the Fe ion has no other Fe ions at its nearest neighbouring sites. The hyperfine field is $\sim$510 kOe for Fe ions with all Mn ions as their nearest neighbours and becomes much lower as some of these Mn ions are substituted by other Fe ions. The concept of the " supertransferred hyperfine field " does not seem to give a satisfactory explanation in this case. The Mössbauer spectra can be fitted reasonably well by a statistical model based on the number of nearest Mn neighbours being substituted by Fe ions. It is concluded that this is simply the result of the core-polarization by the d-band electrons. This further strengthens the idea of the collective behavior of the d-electrons in the undoped system. However,

the Mn^{55} NMR spectra which show three absorption lines instead of one for the undoped system suggest some localization of the d-electrons in the Mn^{3+} and Mn^{4+} sites. It is found that the localization increases as a function of the Fe substitution. We propose the formation of trapping centres for the d-holes due to the presence of Fe ions whose d-electrons are known to be more localized than those of Mn ions. This clearly indicates the simultaneous existence of the localized and collective behavior of the d-electrons. In other words, the transition of localized↔collective can be regulated by the amount of Fe substitutions. The fact that the rapid decrease of the magnetization versus temperature curve near the Curie temperature becomes less obvious as the amount of substitution increases suggests the presence of other exchange mechanism which is most likely the " superexchange interaction ", a well known interaction between localized spins. This further supports the above interpretation.

Finally, the Mössbauer results of the mixed ferrite system, $Zn_XNi_{1-X}Fe_2O_4$, which is known to be an insulator are presented. It is found that for $X \leq 0.5$ the Fe ions have a collinear spin arrangement between the two sublattices and for $X > 0.5$ a spin arrangement similar to that found by Chappert and Frankel in their study of the $NiCr_{1.7}Fe_{0.3}O_4$ system. The average canting angle of the Fe spins is found to be smaller than the angle reported by Satya Murthy et al. using the neutron diffraction technique. An explanation based on the relative strength of the exchange constants J_{AB} and J_{BB} is given to account for this difference. Within the limit of experimental errors the cation distributions calculated from the well resolved spectra

in a 50 kOe external field are proven for the first time to follow the formula $(Zn_XFe_{1-X})[Ni_{1-X}Fe_{1+X}]O_4$ for $0 \leq X \leq 1$. The hyperfine field at the A-site is almost constant for the entire range of X values and this is consistent with the finding of the Sb substituted $LiFe_5O_8$ reported by Evans and Swartzendouber. The decrease of the B-site hyperfine field is explained in terms of the concept of the "supertransferred hyperfine field" which is known to exist in some well localized d-electron systems.

I INTRODUCTION

1.1 DOUBLE EXCHANGE

This mechanism was first proposed by Zener [1] in suggesting that ferromagnetism arises from the indirect coupling of incomplete d-shells via the conduction electrons. He postulated that magnetic behavior of transition metals was determined by the relative strength of three types of spin coupling, namely, between d-shell electrons, d-shell and conduction electrons, and conduction and conduction electrons. The total spin energy was then

$$E_{spin} = \tfrac{1}{2}\alpha S_d^2 - \beta S_d S_c + \tfrac{1}{2}\gamma S_c^2 \qquad (1)$$

where α, β and γ were constants in energy units. By minimizing E_{spin} with respect to the conduction electron spin S_c he obtained

$$E_{spin} = \tfrac{1}{2}\left[\alpha - (\beta^2/\gamma)\right] S_d^2. \qquad (2)$$

Therefore the magnetic behavior will be solely determined by the relative magnitudes of β^2 and $\alpha\gamma$, that is

$$\beta^2 \begin{cases} > \\ < \end{cases} \alpha\gamma \qquad \begin{matrix} \text{ferromagnetism} \\ \text{antiferromagnetism.} \end{matrix} \qquad (3)$$

He applied this concept to the system $(La_{1-x} A_x) MnO_3$

where A represents Ca, Sr, or Ba. Here, instead of having direct exchange between d electrons there is an oxygen in the middle. He suggested that the extra electron on the Mn^{3+} ion can move back and forth between the two Mn ions if the transfer does not change the electron spin direction and if the spins of the ions are parallel. The exchange energy ϵ is given by the integral

$$\int \psi_1^* (H - \epsilon_0) \psi_2 \, d\tau \qquad \begin{matrix} \neq 0 & \text{spins parallel} \\ = 0 & \text{otherwise} \end{matrix} \qquad (4)$$

where ψ_1 is Mn^{3+}-O-Mn^{4+} and ψ_2 Mn^{4+}-O-Mn^{3+}. This he called " Double Exchange ". Anderson and Hasegawa [3] have investigated this mechanism in greater detail and with considerably more general assumptions. They, using a semiclassical approach, derived the energy of the system to be

$$E = -JS \pm b \, (\cos \theta/2) \qquad (5)$$

for $JS \gg b$ where J is the intra-atomic exchange integral, b the transfer integral, S the spin of the ion and θ the angle between two ionic spins in adjacent sites. Here the energy is linear in S while for superexchange interaction it is quadratic in S. The angular dependence is also different.

1.2 SUPEREXCHANGE

This exchange mechanism was originally proposed by Kramers

[4] and subsequently investigated by other workers [5]. No attempt is made here to discuss it in detail except to point out some of the major contributions to this exchange. We consider only the case of indirect exchange. (i) Correlation Effect: This mechanism [6,7] takes into account the simultaneous partial bond formation on each side of the anion. This formation occurs whenever there is an empty cation d orbital overlapping with a full anion p orbital. This can be explained simply as follows. If the cation has an oriented net magnetic moment, the two p electrons will not have an equal probability of being shared by the cation. According to Hund's rule, if the d shell is extended by the s and p orbitals to form hybrid orbitals in the lattice, the anion electron whose spin is parallel to the net cation spin will spend more time on the cation than that with antiparallel spin. This bond is predominated by a single electron and is sometimes called " semicovalent ". For example, in the case of d^5-O-d^5, only pσ orbitals with spins antiparallel to the cation spin can participate in bond formation in accordance with Hund's rule and thus the cation spins are coupled antiferromagnetically. Of course the pπ orbitals also contribute to the antiparallel coupling but this is considerably weaker than the σ bonds. In the case of d^3-O-d^3, on the other hand only pσ orbitals with spins parallel to the cation spins can contribute significantly in the bond formation and the cation spins are antiparallel.

This coupling is weaker than the first case because it in-

volves a third-order rather than second-order perturbation theory [8]. The transferred spin involves a further exchange coupling within the ion, that is, the coupling between the e_g and t_{2g} orbitals. Finally for the case d^5-O-d^3, the spins on one side are parallel and on the other antiparallel and consequently the cation spins are ferromagnetically coupled.

(ii) Delocalization: In this mechanism, an electron is assumed to drift from one cation site to the other, so it depends sensitively on the amount of orbital overlapping. Since there is no direct overlapping between cations, the transfer integral, b_{ij}, is proportional to the square of the overlapping of the cation and anion orbitals or J is proportional to the fourth power of the overlapping. For the first case discussed in (i), the cation spins are strongly antiferromagnetically coupled, same as the direct superexchange between two e_g orbitals. The second case is weakly antiferromagnetic because only the π bondings contribute. The third case corresponds to the direct exchange between half-filled and empty orbitals and is ferromagnetic but the weak antiferromagnetic bonding is also present.

Of course, we can have indirect superexchange involving more or less than half-filled orbitals and they can be discussed in similar terms.

II $La_{1-X}Pb_XMnO_3$

2.1. INTRODUCTION

In early 1950's, Jonker and Van Santen [9] studied polycrystalline materials with the general formula $(La^{3+}_{1-X}M^{2+}_X)$ $Mn^{3+}_{1-X}Mn^{4+}_X O_3$ where M is a divalent cation, either Ca, Sr, Ba, Cd or Pb. These materials crystallize in perovskite structure. The La and M ions are positioned at the corners (0,0,0) of the simple ideal perovskite cell, the Mn ions at the cube centers $(\frac{1}{2},\frac{1}{2},\frac{1}{2})$ and the O ions at the face centers $(\frac{1}{2},0,\frac{1}{2})$. The end members, $X = 0$ or 1 are antiferromagnets and insulators. For certain ranges of X, usually in the region $X \gtrsim 0.3$ the compounds were found to be essentially ferromagnets with a pronounced higher electrical conductivity [9]. To account for the ferromagnetic interaction, Zener [1] introduced the theory of double exchange wherein free or quasifree d-band carriers are exchanged between Mn^{3+} and Mn^{4+} ions. This theory was further developed by Goodenough [6], Anderson and Hasegawa [3] and De Gennes [10]. On the experimental side, transport measurements of polycrystalline $(LaSr)MnO_3$ was reported by Volger [11] and neutron diffraction measurements of polycrystalline $(LaCa)MnO_3$ by Wollan and Koehler [12]. Lack of stoichiometry had been a serious drawback in these earlier studies. However, since then crystal growth technique has been greatly improved, good single crystals in a

limited range of X could be grown by the flux technique [94]. Thus a more thorough study of this family of compounds becomes possible.

Perovskites are a family of compounds having a crystal structure similar to that of the mineral perovskite $CaTiO_3$, and, in general, can be designated as ABX_3 where A = larger cation, B = smaller cation and X = anion. In order to have perovskite structure, the ions have to satisfy certain conditions. Usually, the B cations occupy corner-shared octahedra and this requires that the B cations have a preference for octahedral coordination and have an effective charge since this structure is stabilized mainly by electrostatic energy. These stable, polar octahedral-site building blocks form the skeleton of the perovskite structure. The relatively large anionic interstice which the A cation must occupy created by these blocks in turn requires a certain size for the A cation. These conditions are summerized by the tolerance factor [2]

$$t = (r_A + r_X)/[2(r_B + r_X)]^{\frac{1}{2}} \qquad (1)$$

where r_A, r_B, r_X are empirical radii of ions A, B and X respectively with the added conditions for oxides which concern us mainly in this study that $r_A > 0.90$ Å and $r_B > 0.51$ Å since A and B must be stable in twelvefold and sixfold coordinations respectively.

2.2 SINGLE CRYSTAL GROWTH

Since the phase equilibrium diagram required for the selection of suitable starting reagents for the growth of

$(LaPb)MnO_3$ single crystals was not known, a number of compositions and growing conditions were tried.

The 100 cm^3 platinum crucibles were loaded with selected amounts of La_2O_3, MnO_2 and a PbO-PbF_2 flux. These materials were in powder form and compressed with a rod under finger pressure. Each crucible was fitted with snap-on lids which, however, led to a variable evaporation of flux. The crucibles were placed inside a muffle inserted in a large top-loading furnace heated by four pairs of Norton globar resistence elements. The system was then brought to a chosen soak temperature between 1165 and 1250°C for 24 hours to ensure that all constituents were in solution. Thereafter, cooling at the rate of 1°C per hour with a stability of 1°C was achieved with a Leeds and Northorp programmed controller that fed a saturable reactor, which in turn controlled the input to a 10 kW autotransformer.

The temperature was sensed with a platinum-platinum 10% rhodium thermocouple beneath the furnace inserted through a hole into the muffle where the tip was positioned close to the bottom of the crucible. The purpose of the muffle was to reduce the thermal fluctuations and to act as a filter in reducing contamination of the furnace with flux (usually lead) fumes.

When the temperature reached 980°C, the power was turned off and the furnace top opened slightly. The crucibles were removed about 24 hours later when the furnace had cooled

almost to room temperature.

A typical run would be using 120 gm. of PbO, 120 gm. of PbF_2, 19.85 gm. of La_2O_3 and 21.15 gm. of MnO_2. The purities of PbO, MnO_2 and La_2O_3 were 99.9%, 99.8% and 99.99% respectively. No specifications were available for the PbF_2. For different values of X, different quantities of La_2O_3 and MnO_2 were used but the amount of flux material was kept usually constant. The $(LaPb)MnO_3$ crystals were removed from the solidified flux by boiling in glacial acetic acid for a minimum of 100 hours. A total of 35 runs were made and each run took, on the average, 18 days. The crystals were found throughout the flux indicating that the two densities were about equal. The total crystal yield from one run is shown in Fig.1a. The largest crystal volumes were about 0.15 cm^3, big enough for the present series of experiments. The growth habit produced cubes with {100} faces, Fig.1b.

Twinning was often found, particularly for those crystals formed near the crucible bottom (Fig.1c). However, sizable crystals can only be obtained in a limited range $0.26 \lesssim X \lesssim 0.44$. Outside this range the crystals were very much smaller and poorer in quality. Several attempts had been made but without success.

Fig.1d shows the photomicrographs of the surfaces of some single crystals. In a, b and c, the surfaces show

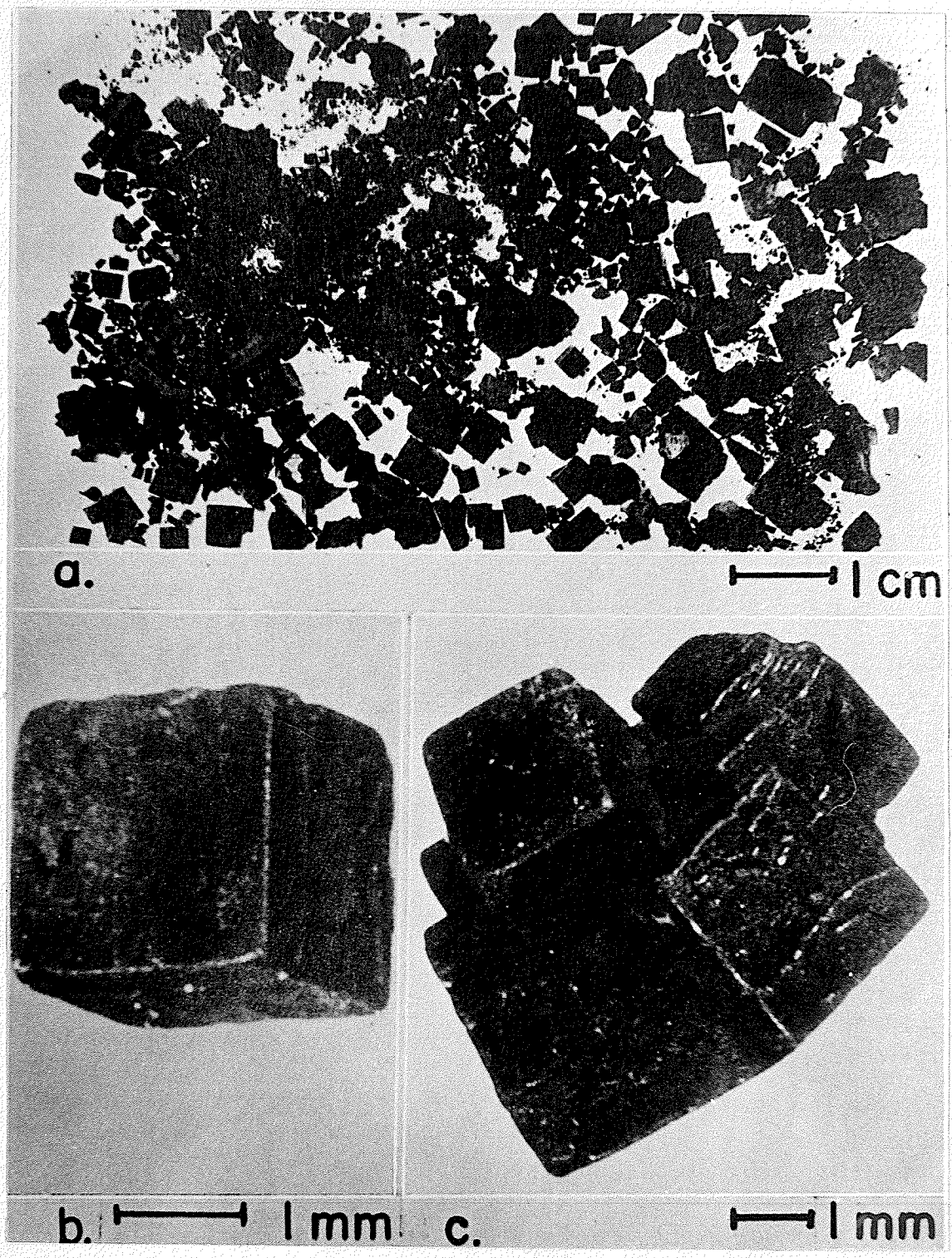

Fig. 1. Synthetic single crystals of $(LaPb)MnO_3$. (a) The yield from one crucible. (b) A typical cube-shaped crystal with 100 faces. (c) A multitwinned crystal.

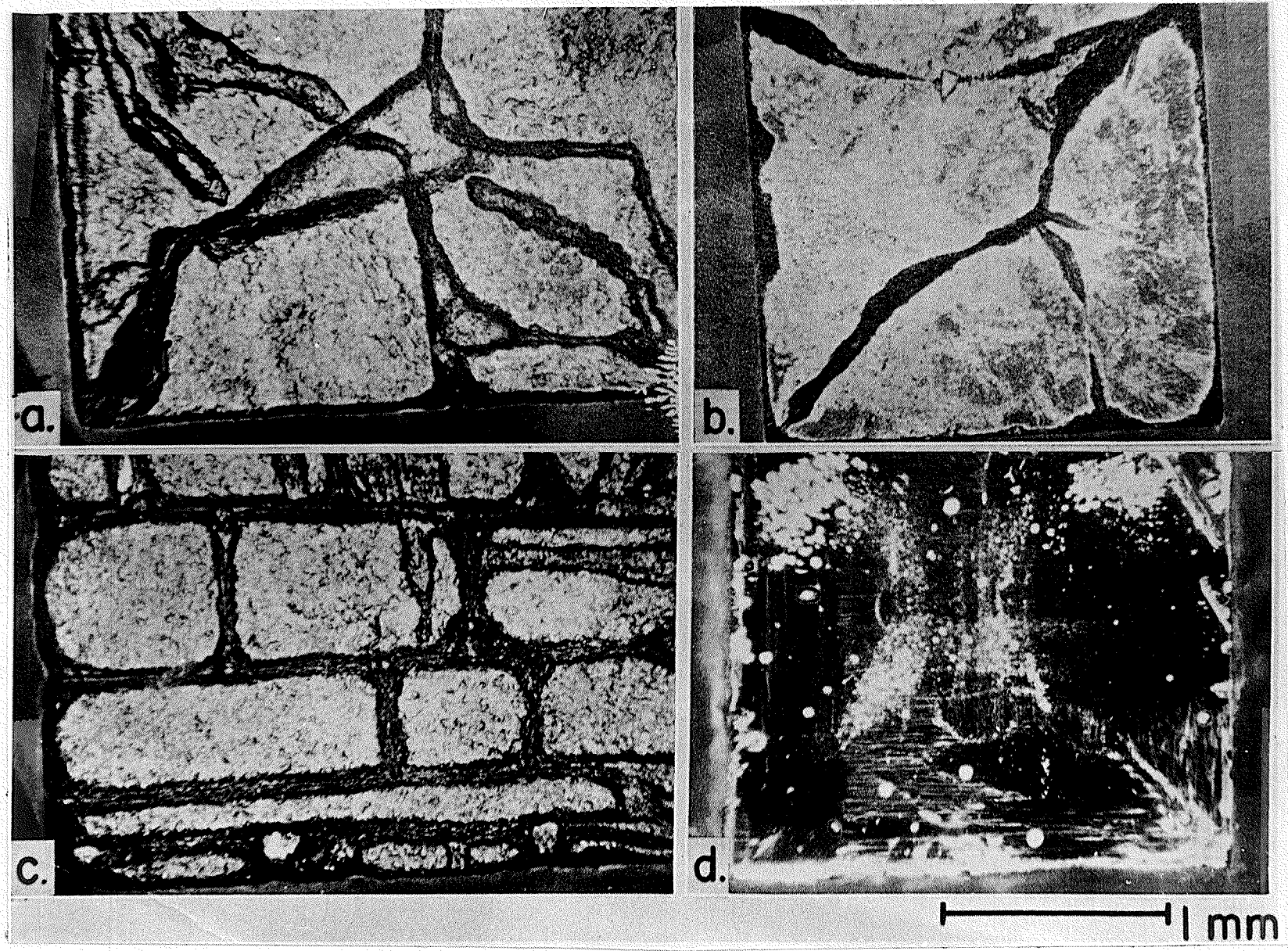

Fig. 1d. Photomicrographs of the surfaces of some single crystals.

grooves of one to two microns deep which are believed to be etched by the flux, because d shows a surface which is shiny for a run in which all the flux had evaporated. The etch pattern such as that brick-like structure shown in c does give us some ideas about the growth process.

2.3 COMPOSITION ANALYSIS

X-ray fluorescence was used to determine X. The samples were prepared by grinding about 1 gm. of single crystals into fine powder which were cleaned in acid to remove possible remaining flux and then pressed into a disk, with the addition of 0.3 gm. of B_2O_3 as a binder. Standard disks, used for comparison, were made from mixtures of La_2O_3, PbO, and MnO_2 powders.

Measurements were made in duplicate and averages were used to determine the final result. Typical plot for determining La and Pb contents is shown in Fig.2. The two weight percents were then normalized such that the sum of La and Pb atomic fractions equalled one, that is, no defects were assumed to be present.

Results on five selected runs are given in column one of Table I. The total manganese content and the relative amount of Mn^{3+} and Mn^{4+} were determined by standard volumetric techniques [13].

Prior to any wet chemical analyses, the crystals were boiled for 3 hours in 6:3 $HClO_4$–HNO_3 solution to remove any flux inclusions. The total amount of manganese present was

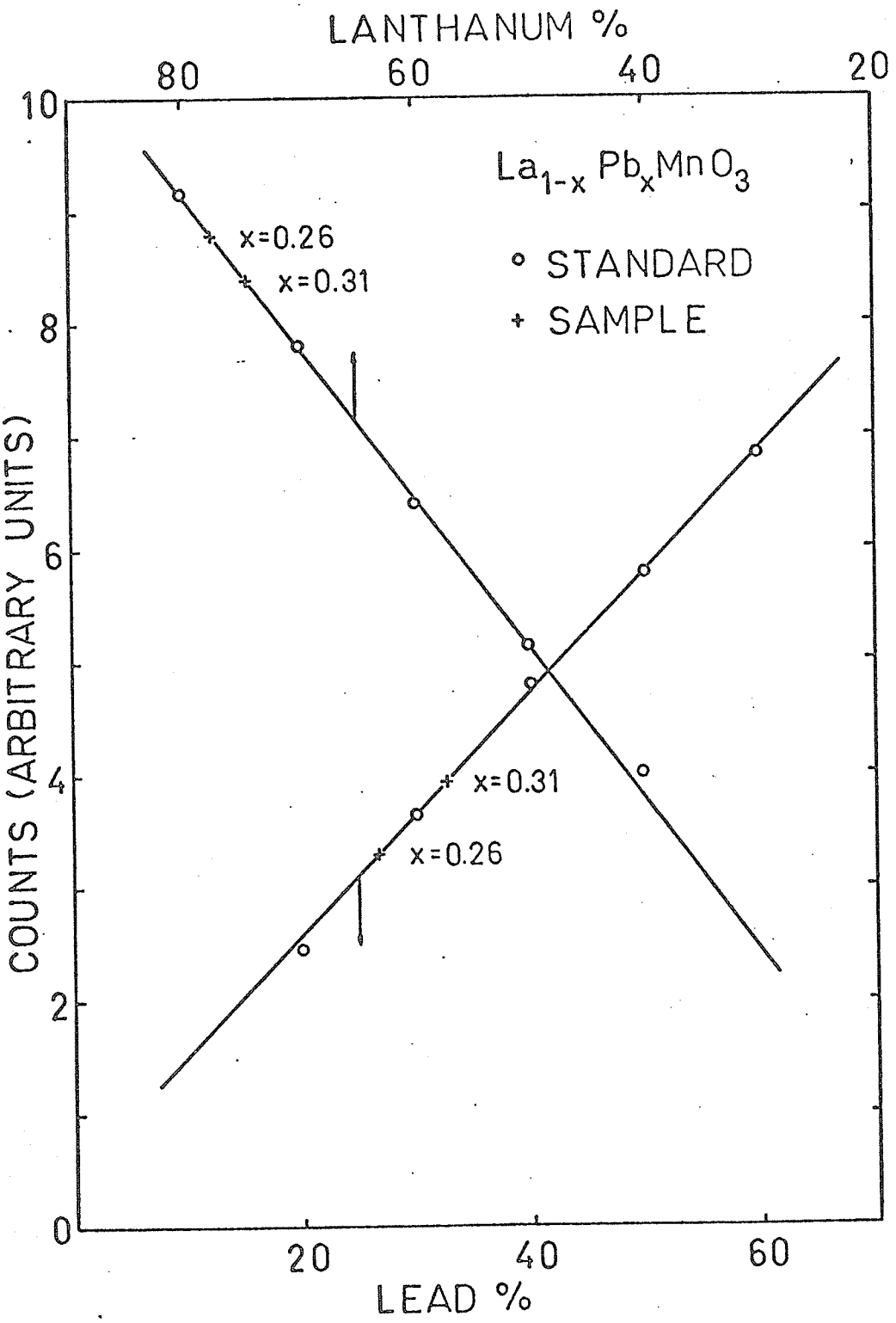

Fig. 2. Determinations of lead and lanthenum content by X-ray fluorescence technique.

determined by the bismuthate method [12]. The Mn^{3+} and Mn^{4+} contents were determined by adding an excess of standard ferrous ammonium sulfate to the samples dissolved in a dilute sulfuric acid solution, filtering off the $PbSO_4$ precipitate, and oxidizing the excess ferrous ions with standard $KMnO_4$. The weight percentages of total Mn, Mn^{3+} and Mn^{4+} thus determined are listed in Table I. Within the experimental errors inherent in the fluorescence and chemical methods, the agreement is satisfactory.

Electron microprobe [14] with a beam diameter of about 1 micron was used to determine the homogeneity of the crystals. It was found that the La and Pb contents were constant to within 1% along paths about 3 mm in length. Therefore, the lead doping can be assumed to be very uniform throughout the crystals.

2.4 CRYSTAL STRUCTURE

The lattice constants of $(LaPb)MnO_3$ were determined with a Philips 57.3 mm. radius Debye-Scherrer camera and diffractometer using both Fe-Mn and Cu-Ni radiation. A silicon standard was used to correct the line positions in the diffractometer traces. To avoid any variations in line intensities from preferred orientations, the powdered samples were mixed with gum tragacanth. The structure was found to be rhombohedrally distorted perovskite. Goodenough [6] has pointed out that the

Table I. Data on X-ray Fluorescence and Chemical Analyses for $(LaPb)MnO_3$ Single Crystals.

Nominal* Formulae	Total Manganese weight percent		Mn^{3+} weight percent		Mn^{4+} weight percent	
	Found	Expected	Found	Expected	Found	Expected
$La_{0.74}Pb_{0.26}MnO_3$	20.7	21.2	14.3	15.7	6.4	5.5
$La_{0.69}Pb_{0.31}MnO_3$	20.0	20.9	12.9	14.5	7.1	6.4
$La_{0.62}Pb_{0.38}MnO_3$	20.5	20.5	14.1	12.8	6.4	7.7
$La_{0.60}Pb_{0.40}MnO_3$	20.2	20.4	12.5	12.3	7.7	8.1
$La_{0.57}Pb_{0.43}MnO_3$	19.6	20.2	11.0	11.4	8.6	8.8

*The La and Pb weight percentages were determined experimentally and normalized such that the sum of their atomic fraction equals one.

ordering of Mn-O-Mn covalent bonding in our composition range would produce a cooperation elastic strain to rhombohedral symmetry.

The complete powder diffraction data for $La_{0.62}Pb_{0.38}MnO_3$ are given in Table II. The presence of the weak 131 line indicates that the cell edges are doubled. The lattice constants are listed in Table III for five compositions. The average error in α_{rh} is estimated to be less than $\pm$ 3 min. The theoretical density for one component, $La_{0.60}Pb_{0.40}MnO_3$ is 7.532 gm. cm^{-3} which agrees well with 7.451 gm. cm^{-3} which was determined by using the Berman balance.

2.5 STATIC MAGNETIZATION

The magnetization of five representative compositions has been measured from 4.2 to 773°K [95] which is well above the Curie temperature, Tc.

2.5.1 EXPERIMENTAL APPARATUS AND METHODS

A vibrating-sample magnetometer [14a] manufactured by the Princeton Applied Research Corp. (PAR) was used for the measurements. The electromagnet used to produce the static field was manufactured by Magnion Inc.

The low sample temperatures were achieved with a liquid-helium dewer (made available to PAR by Andonian Corp.) equipped with a needle valve to control the helium or nitrogen flow

Table II. Powder Diffraction Data for $La_{0.62}Pb_{0.38}MnO_3$.

Intensity	d_{obs}	d_{calc}	hkl
18	3.906	3.908	200
77	2.774	2.773	$2\bar{2}0$
84	2.756	2.754	220
*	2.351	2.363	$\{1\bar{3}1$ $1\bar{3}1$
26	2.261	2.261	$22\bar{2}$
11	2.239	2.240	222
52	1.953	1.954	040
9	1.754	1.751	$04\bar{2}$
9	1.741	1.744	240
50	1.598	1.602	$22\bar{4}$
23	1.585	1.586	242
14	1.385	1.386	$04\bar{4}$
20	1.374	1.377	440
28	1.237	1.237	$06\bar{2}$
38	1.232	1.234	260
3	1.181	1.182	$\{\bar{6}22$ $62\bar{2}$
3	1.172	1.173	622
6	1.129	1.125	$44\bar{4}$
3	1.117	1.120	444
2	1.086	1.087	$\bar{6}40$
3	1.078	1.080	640
14	1.046	1.048	$\bar{6}42$
14	1.041	1.047	$6\bar{4}2$
11	1.036	1.044	$64\bar{2}$
6	1.035	1.039	642

*Intensity too low to detect on diffractometer trace using Fe radiation. Line position taken from 10 hour exposure of Debye-Scherrer photograph.

into the sample chamber and a heating coil just outside the sample chamber. The temperatures from 4.2 to 77° K were measured with a gold 2.1% cobalt-copper thermocouple and from 77 to 300° K with a copper-constantan thermocouple.

Table III. Lattice Constants of Perovskite $(LaPb)MnO_3$.

Sample Formula	a_{rh} (Å)	α_{rh}
$La_{0.74}Pb_{0.26}MnO_3$	7.799 ± 0.010	90° 28'
$La_{0.69}Pb_{0.31}MnO_3$	7.798 ± 0.010	90° 23'
$La_{0.62}Pb_{0.38}MnO_3$	7.815 ± 0.004	90° 24'
$La_{0.60}Pb_{0.40}MnO_3$	7.801 ± 0.010	90° 23'
$La_{0.57}Pb_{0.43}MnO_3$	7.776 ± 0.005	90° 19'

For measurements above room temperature, the apparatus included a boron nitride sample rod and a heating coil enclosed in a vacuum jacket manufactured also by PAR; the temperature was measured with a chromel-alumel thermocouple.

Some samples were ground into spheres in order to take account of demagnetization effects. The grinding was done on the ultrasonic cutter. The grinding tip was made of brass and

was just a flat surface with a semispherical impression in the centre. This impression could be simply made by pressing the flat surface against a suitable size steel ball. However, the tip had to be changed quite often because the abrasive ground the crystal as well as the mould at the same time.

In the case of single crystal, the sample was glued to the end of a long sample rod with G.E. No. 7031 adhesive which works well even at helium temperature. In the case of powder, an aluminum holder was used for low temperature, a Boron-Nitrite holder for high temperature. The sample was placed in the centre of the pole gap and was magnetized by the static magnetic field. By Lenz law, as the sample vibrates, a current proportional to the magnetic moment of the sample is induced in a sensing coil which was positioned near the vibrating sample.

A small spectropure nickel sphere, 58.5 emu/gm. at 4.2° K (or 55.07 emu/gm. [14b] at 298° K), was used for the calibration of the magnetometer.

2.5.2 MAGNETIZATION BELOW T_c

The temperature of the sample in the magnetometer was always held constant to within $\pm$ 2°C and for some important regions, for example, near the Curie temperature, to better than $\pm$ 1°C.

Normally, the magnetic field, H, was then varied from 1 to 18 kOe and the magnetic moment per gram, σ_M,

recorded. However, the magnetization was so sensitive to the change in temperature especially when the temperature was about 50°C from the Curie point, that even 1° change caused a large change in the extrapolated moment as well as the susceptibility in this region. In order to avoid these pitfalls, we had to record the temperature as well as the magnetic moment at each applied field strength so that we could plot the magnetic moment versus the temperature at constant field value. A typical plot is shown in Fig.2a. From this plot we could then obtain σ_M value at fixed temperature accurately. A typical set of σ_M versus H curves for one chemical composition is shown in Fig.3. The curve for 4.2° K has been lowered at H = 18 kOe by almost 1% to correct for a weak moment induced in the thermocouple; the correction is negligible for temperatures above 20° K and for low fields at all temperatures.

A value of the spontaneous magnetic moment per gram was obtained by extrapolating the linear portion of the curves of the type in Fig.3 to zero internal magnetic field. Curves of σ_M (H = 0) versus temperature are plotted in Fig.4 for the five selected compositions. The magnetic moment per gram at T ≒ 0° K was obtained by extrapolation, and is listed in Table IV. A theoretical value assuming complete ferromagnetic order of the manganese spins can be calculated from the average spin ⟨S⟩ based on the Mn^{4+}/Mn^{3+} ratio. These values, also listed

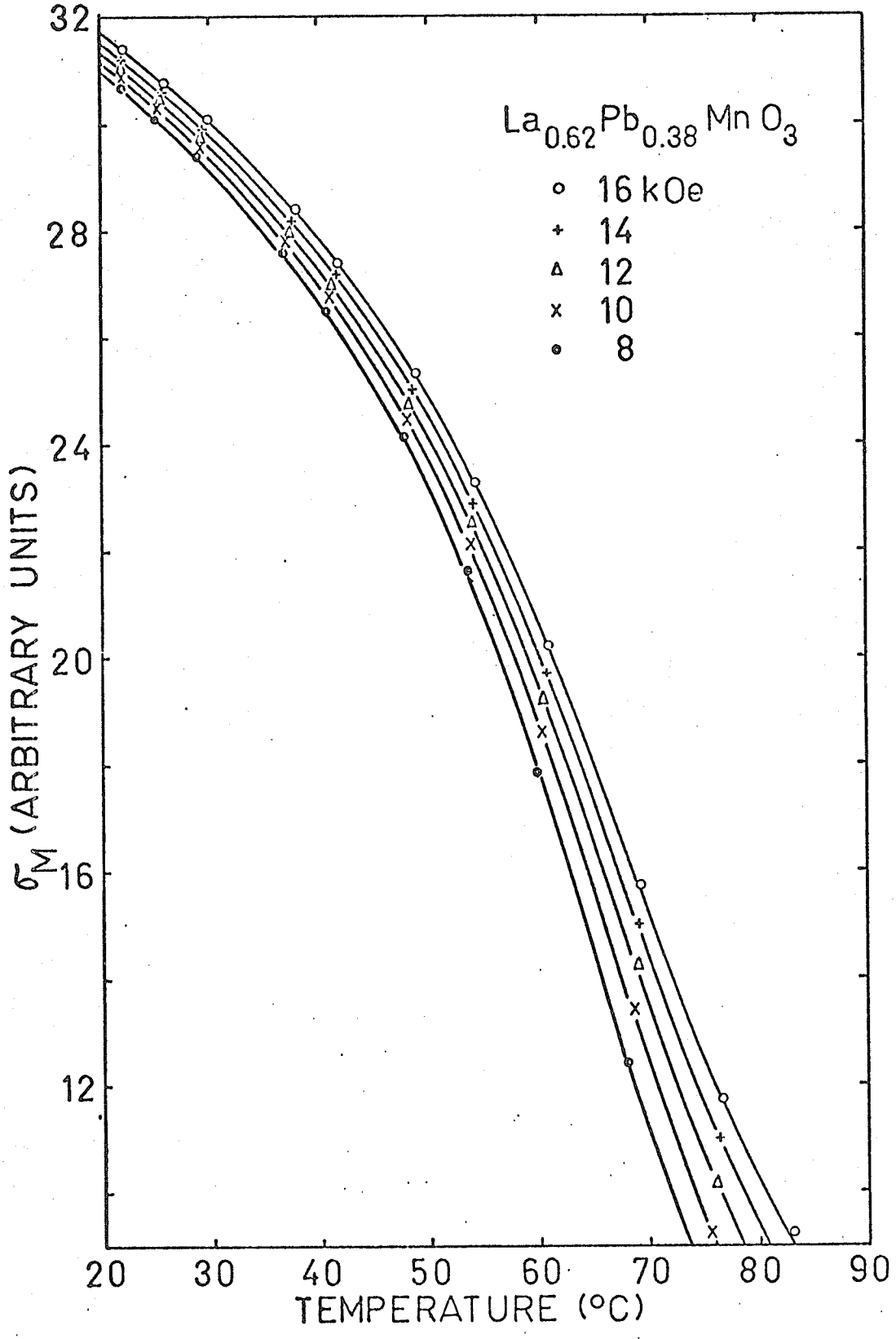

Fig. 2a. Magnetization as a function of temperature in different external fields.

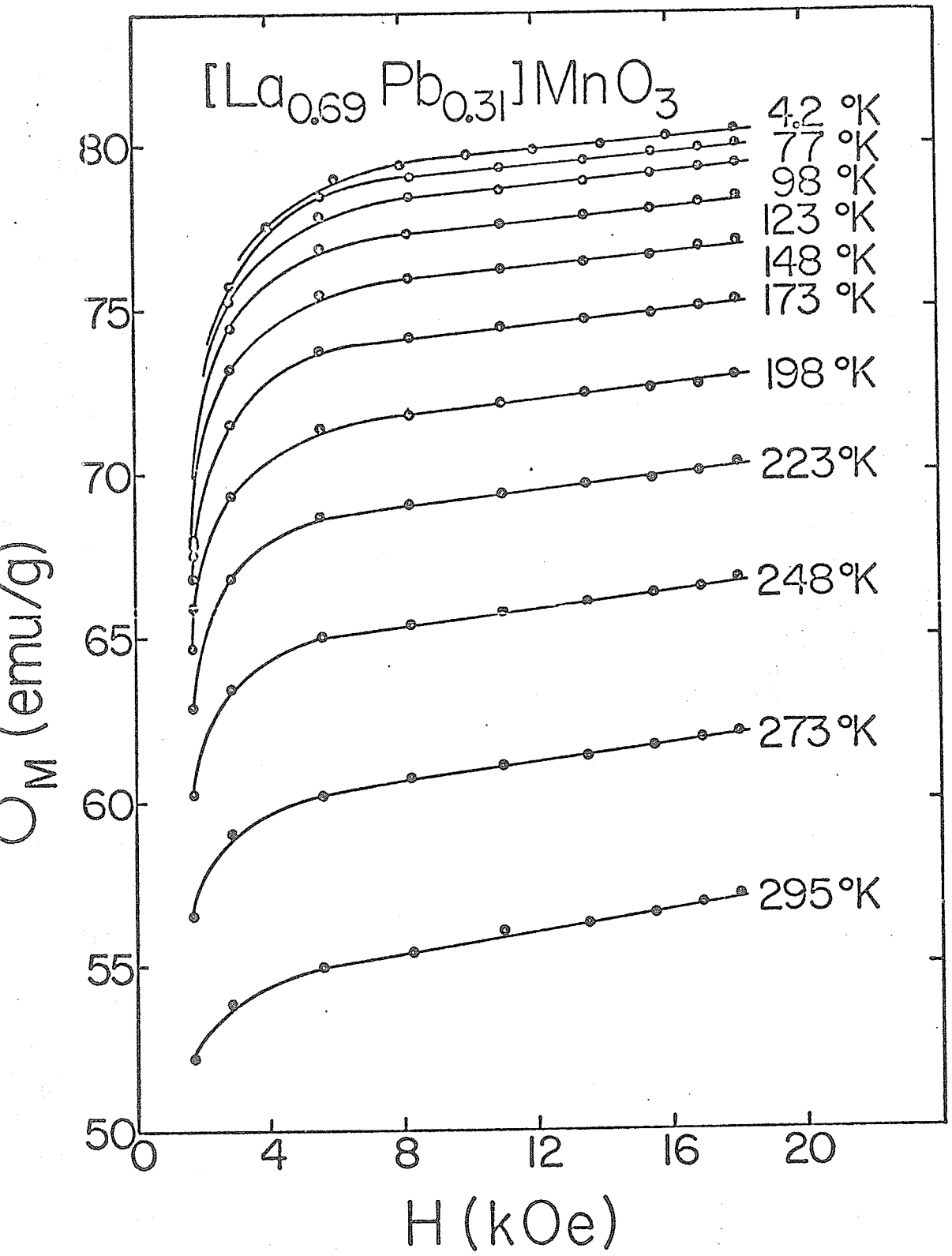

Fig. 3. Magnetization curves of $La_{0.69}Pb_{0.31}MnO_3$ with temperature as a parameter.

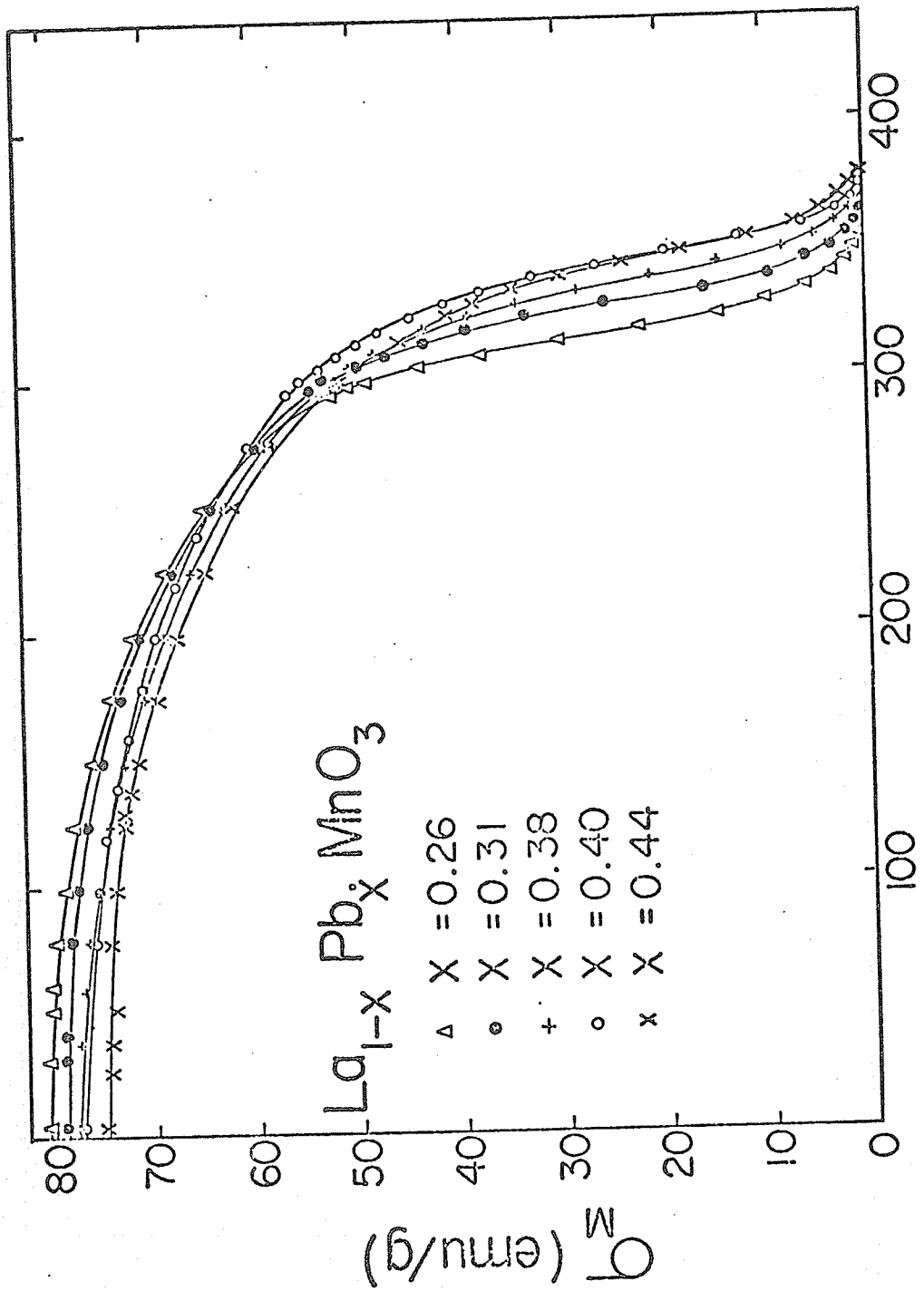

Fig. 4. Saturation magnetization of $La_{1-X}Pb_XMnO_3$ as a function of temperature.

Table IV. Magnetization Data on $La_{1-X}Pb_XMn^{3+}_{1-X}Mn^{4+}_XO_3$.

Composition x	<S> from Chemical Formula	$\sigma_M(O) = Ng\mu_B\langle S\rangle$ (emu/gm) Theoret.	$\sigma_M(O)$ (emu/gm) Exptl.	T_C (°K) Weiss and Forrer Method	T_C (°K) Belov and Goryaga Method	<S> $T>T_C$ Exptl. (±0.02)
0.26	1.87	80.5	80.4	328	318.5	1.87
0.31	1.84	78.5	78.8	337	330.5	1.85
0.38	1.81	75.6	77.6	346	340	1.84
0.40	1.80	74.6	77.2	352	348.5	1.83
0.44	1.78	73.2	74.8	355	350	1.80

in Table IV are in reasonable agreement with the experimental ones, the largest difference being 3%. It is of interest to note that the magnetization curves cross. Also in the vicinity of the Curie temperature, the curves display the well-known "tail" which is possibly due to some short-range ordering peculiar to a ferromagnet.

2.5.3 SUSCEPTIBILITY ABOVE T_c

The susceptibility per gram, χ_ρ, has been determined above T_c up to about 800° K for the five compositions from the linear σ_M versus H curves. The reciprocal of the susceptibility in units of $(\text{emu/gmOe})^{-1}$ is shown as a function of temperature in Fig.5 for the two extreme compositions (X = 0.26 and 0.44); the curves for the other compositions lie in between and have been omitted for clarity. The curves are similar to those observed for the normal metallic ferromagnets such as iron and nickel, exhibiting a curvature just above T_c and becoming linear at higher temperatures. The Curie constant,

$$C = Ng^2 \mu_B^2 \langle S \rangle (\langle S \rangle + 1)/3k, \qquad (2)$$

determined as the inverse slope of the linear portion, yields $\langle S \rangle$. The values of $\langle S \rangle$ obtained for different Mn^{4+}/Mn^{3+} ratios are also listed in Table IV; the agreement with $\langle S \rangle$ for the chemical formula is incredibly good. Indeed, to the

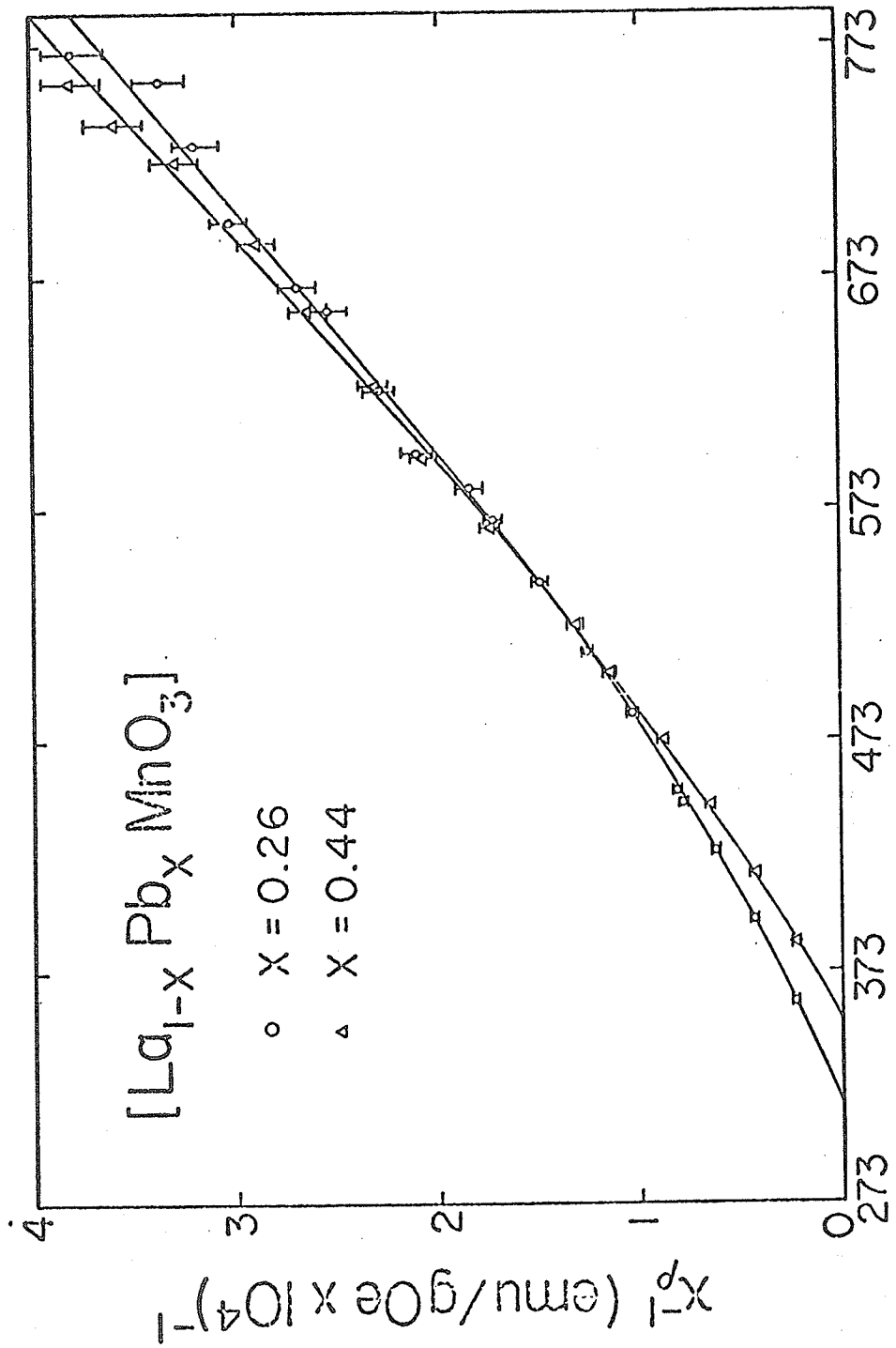

Fig. 5. The reciprocal of the susceptibility as a function of temperature for two compositions.

best of our knowledge, of the known elemental metallic ferromagnets, only for gadolinium is there comparable agreement.

2.5.4 SUSCEPTIBILITY BELOW T_c

The susceptibility determined from the linear portion of the set of curves similar to that shown in Fig.3 is plotted as a function of temperature in Fig.6. The value at low temperature, $\sim 1 \times 10^{-4}$ emu/gmOe, is unusually large when compared to metals such as iron and nickel. The anisotropy of the material is small, and hence, it would appear that technical saturation, between field strength of 10 to 18 kOe, had been reached. Since the Van Vleck and Pauli paramagnetic susceptibility is not normally this large, it may be that there is a canting of the manganese moments. However, since the extrapolated saturation moment is so close to the theoretical moment assuming total spin alignment, the canting angle if it exists, would be quite small.

2.5.5 CURIE TEMPERATURE AND CRITICAL EXPONENT DETERMINATION

In order to determine the Curie point and to examine the magnetization just below T_c, because of the "tail", the data was subjected to further analysis. First, the full curves of Fig.7 were obtained by applying the Weiss and Forrer [15] method of constant magnetization. A typical plot is shown in Fig.8. Three curves show, and the other two hint at, a small "bump" near T_c; the Curie temperatures obtained by extrapolation

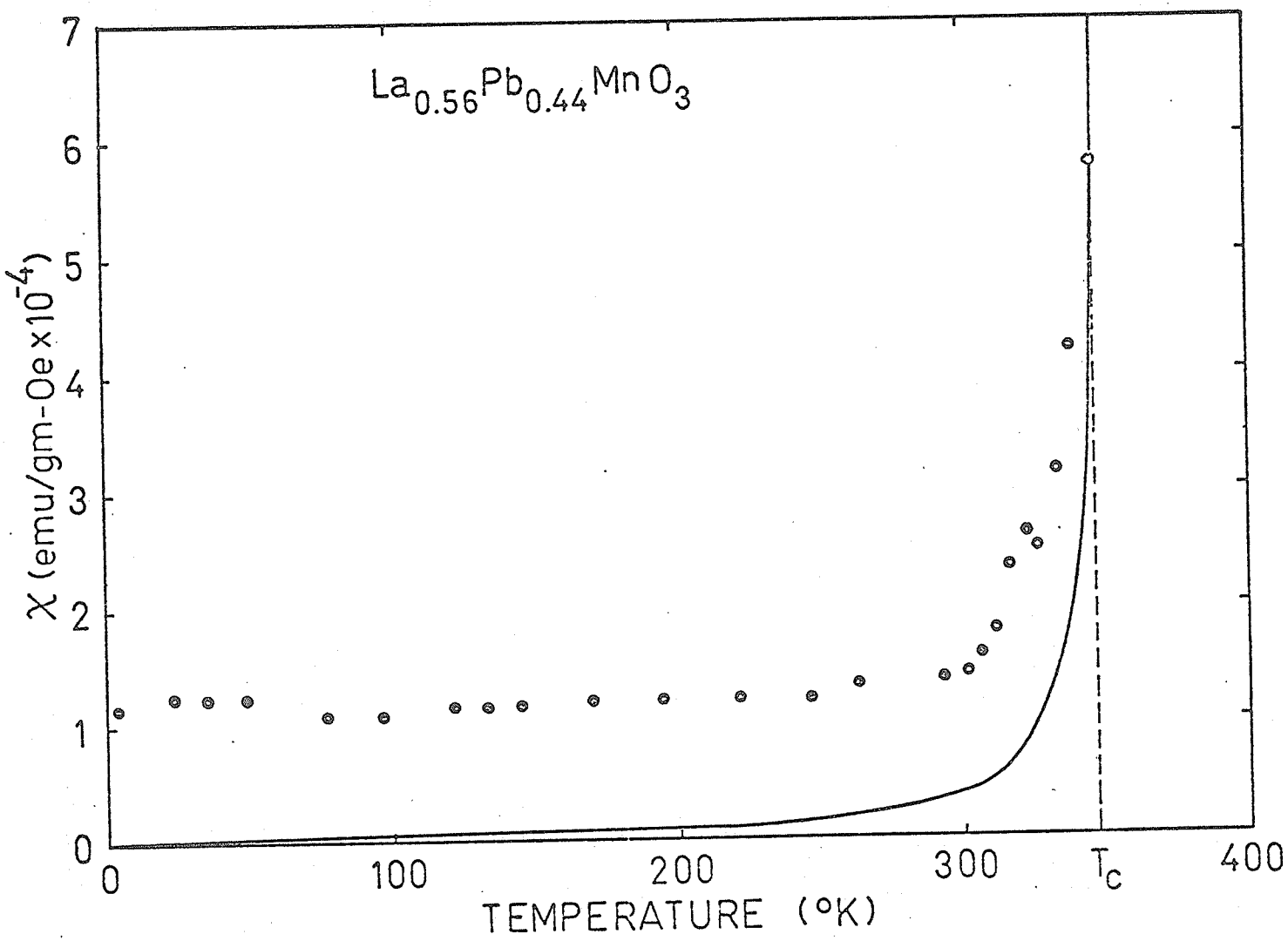

Fig. 6. Differential susceptibility as a function of temperature below T_c for $La_{0.56}Pb_{0.44}MnO_3$. The theoretical curve is obtained from the molecular field theory.

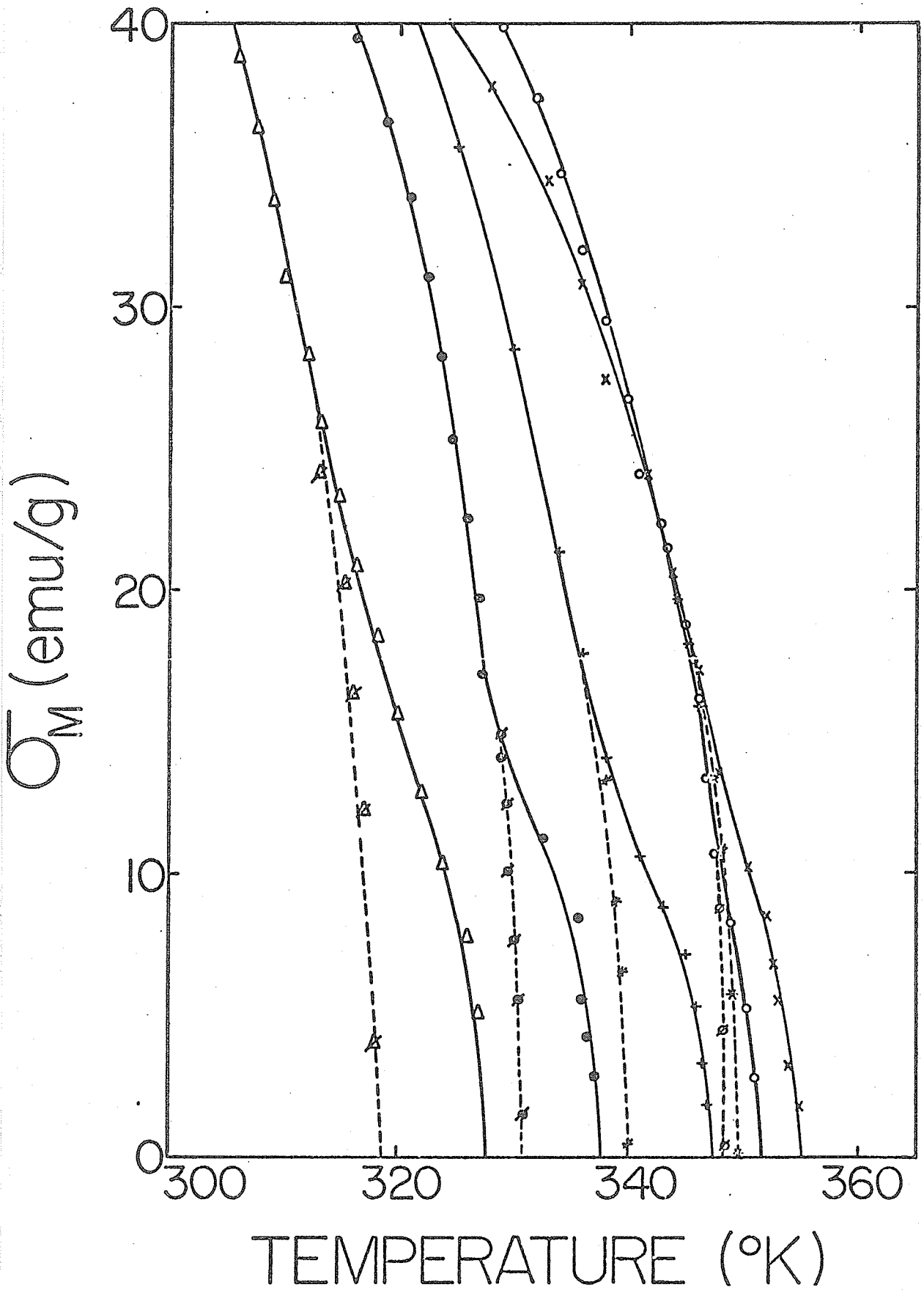

Fig. 7. Saturation magnetization near the Curie temperature. The full curves are obtained by the method of constant magnetization and the dashed curves by the thermodynamic method. The data points refer to different compositions, and these have the same meaning as given in the inset to Fig. 4.

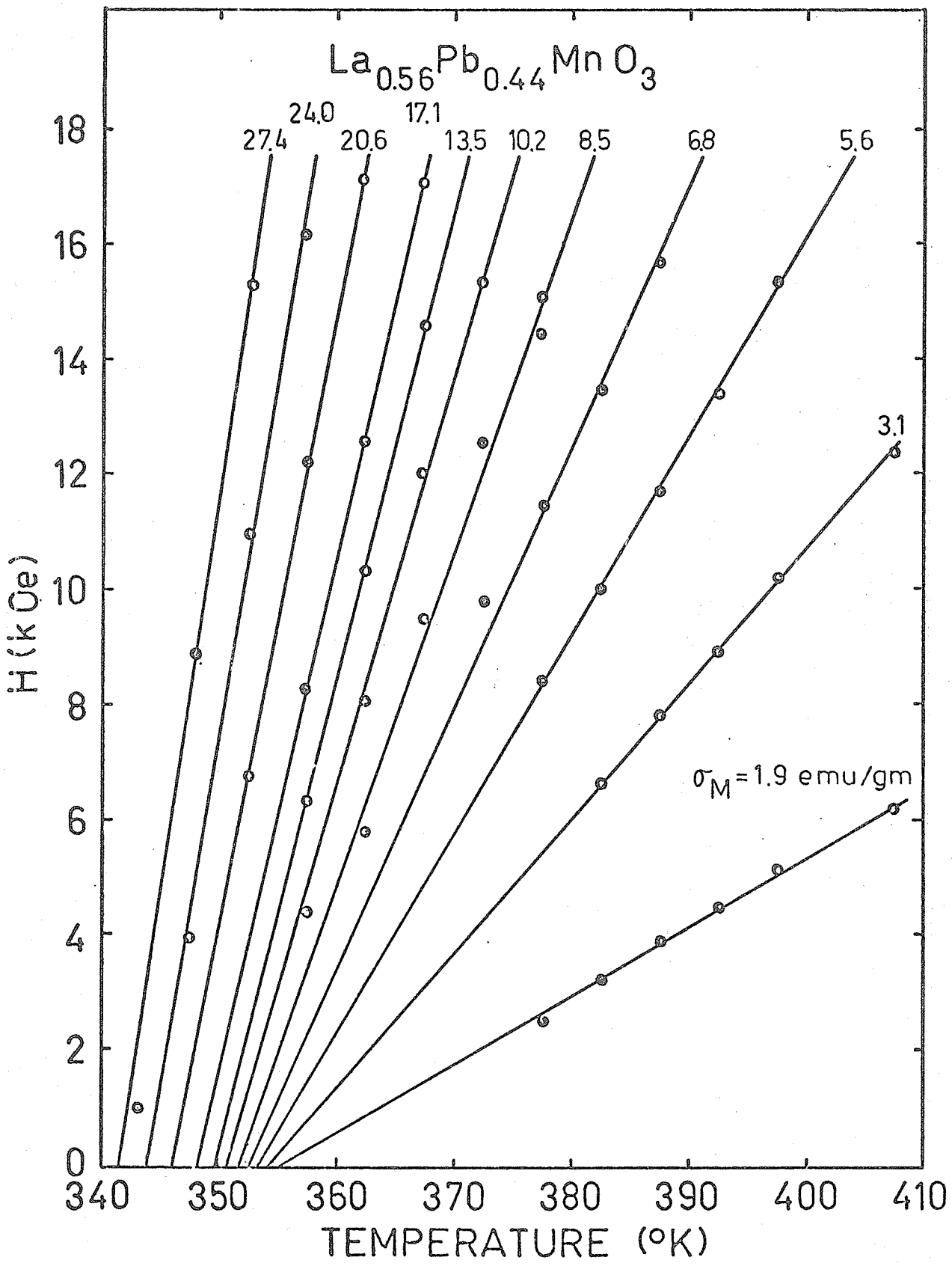

Fig. 8. Curves plotted at constant magnetization.

are given in Table IV. Second, the dashed curves of Fig.7 came from a method [16] based on thermodynamic reasoning, (Appendix A) in which σ_M^2 is plotted against H/σ_M. Now both the bump and tail are absent; the Curie temperatures found are also listed in Table IV. Another method developed by Kouvel and Fisher [19] yields results close to those of the second method. The Curie temperatures could also be determined by using the relationship [97] $\sigma_M \sim H^{1/\delta(T)}$ if $\delta(T_c)$ was known. Regardless of the method of analysis, the Curie temperature is almost a linear function of composition X over the range of Mn^{4+}/Mn^{3+} ratios studied.

The critical exponent β defined by

$$M(T)/M(0) = D(1 - T/T_c)^{\beta} \qquad (3)$$

was determined using the data on Fig.7 over the temperature range $0.95 < T/T_c < 1.0$. A typical plot is shown in Fig.9 and the results for three samples are listed in Table V.

Table V. Critical Indices for $La_{1-X}Pb_XMnO_3$.

X	D	β
0.44	2.1	0.50±0.04
0.31	3.1	0.56±0.04
0.26	3.4	0.59±0.04

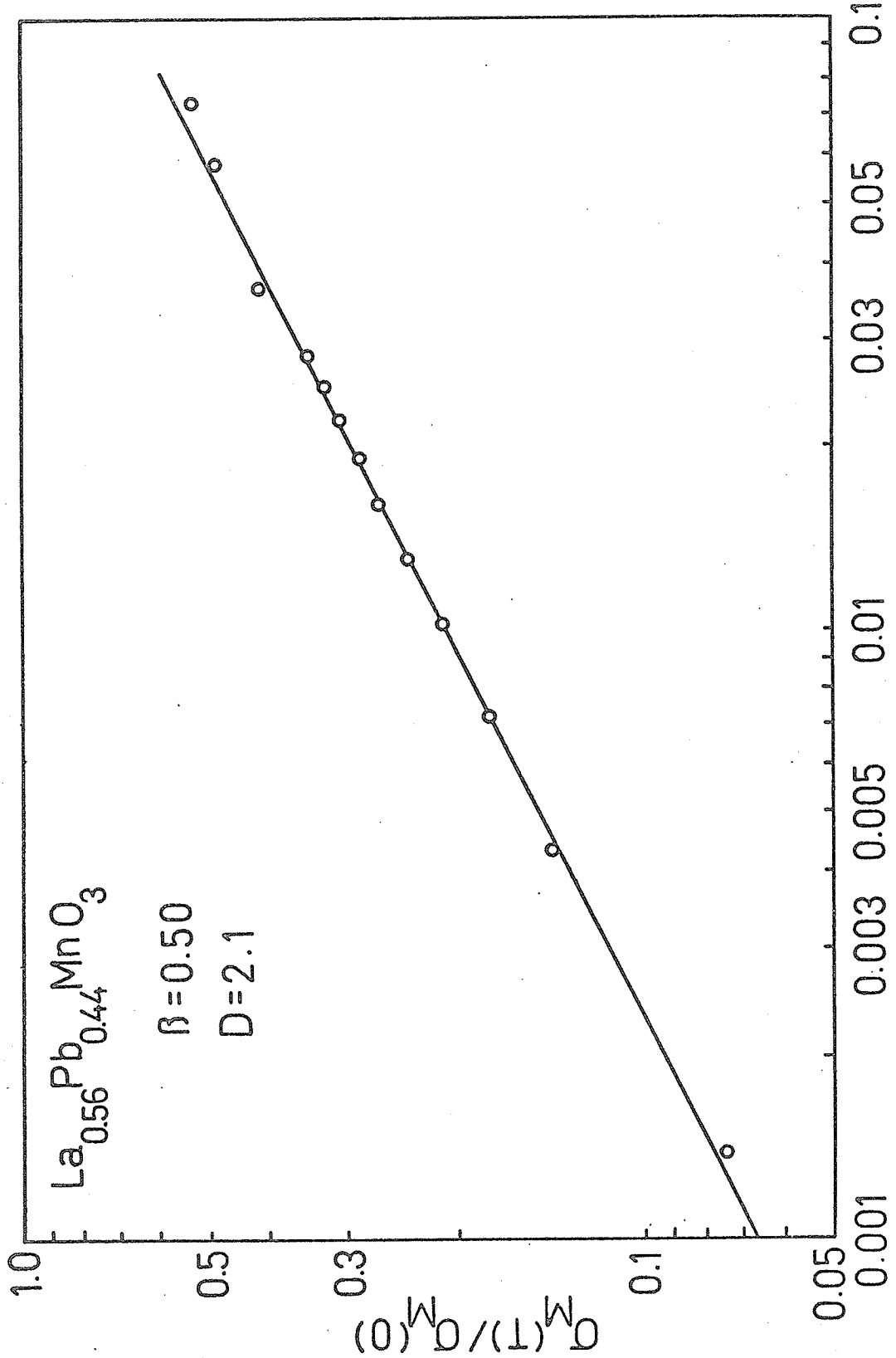

Fig. 9. Logarithmic plot of reduced saturation magnetization versus $(1-T/T_c)$.

2.6 CONDUCTIVITY

The conductivity was measured by the conventional four-probe method at room temperature. However, because of the size problem as well as the characteristic of high conductivity in this range of X, the result was accurate only up to order of magnitude. It was found that conductivity for $0.26 \leq X \leq 0.44$ is $\sim 10^2$ mho/cm. This problem was later carried on further by Searle and Wang [27] using the Van der Pauw's technique [28]. Consistent results were obtained and a typical curve of resistivity as a function of temperature is shown in Fig.10 reproduced from S. T. Wang's thesis [29].

2.7 NUCLEAR MAGNETIC RESONANCE (NMR)

2.7.1 INTRODUCTION

NMR has been widely used in chemistry as well as in Solid State Physics. The theory has been discussed in many excellent texts [30], so here no attempt is made to discuss it in detail. Basically, in nuclear paramagnetic resonance, as a result of the spatial quantization of the nuclear magnetic moments when a magnetic field H is applied, the $2I + 1$ states are split into levels with energies $m_I g_N \mu_N H$. Then transitions between the levels can be induced by the application of an alternating field with a frequency given by

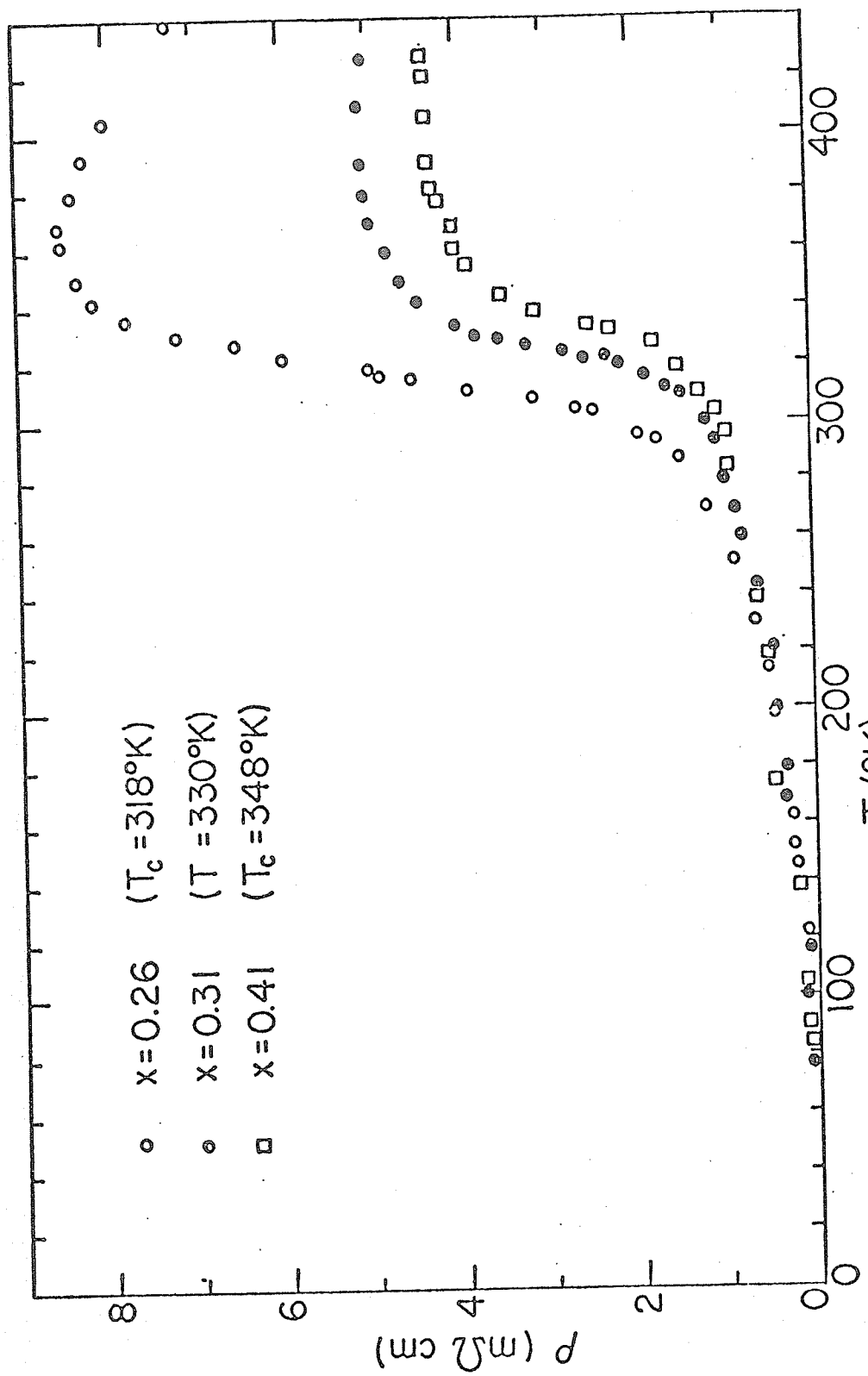

Fig. 10. Electrical resistivity as a function of temperature for three compositions of $La_{1-x}Pb_xMnO_3$.

$$\hbar\omega = -g_N \mu_N H$$
$$\text{or} \qquad \omega = -g_N eH/2M_p c. \tag{4}$$

There are many methods [31] to achieve NMR and they all have their own advantages as well as drawbacks. For a narrow absorption line the steady state method is most commonly used. However, in solid state physics, largely owing to inhomogeneity in the field, broad lines are usually expected, and the pulse method is more desirable. Thus only the latter method is further discussed.

2.7.2 SPIN-ECHO METHOD

The principle of the spin-echo method [32] can best be explained by describing the precessing magnetic moment in a rotating frame at the same angular speed as the rotating of field. The rf power is supplied as short pulses with a duration which is short compared to the relaxation times γ_1(spin-lattice) and γ_2(spin-spin). In general, the equation of motion of a nuclear moment $\vec{\mu}$ with angular momentum $\vec{G}$ in a field H is given by

$$\left(\frac{d\vec{G}}{dt}\right) = \vec{\mu} \times \vec{H} \tag{5}$$

The time rate of change of $\vec{G}$ in the rotating frame, denoted

by $\left(\frac{d\vec{G}}{dt}\right)'$, is related to $\left(\frac{d\vec{G}}{dt}\right)$ by [33]

$$\left(\frac{d\vec{G}}{dt}\right) = \left(\frac{d\vec{G}}{dt}\right)' + \vec{\omega} \times \vec{G} \tag{6}$$

Using equation (5) and $\vec{\mu} = \gamma \vec{G}$, we obtain

$$\left(\frac{d\vec{G}}{dt}\right)' = \vec{\mu} \times \vec{H}_e \tag{7}$$

where $$\vec{H}_e = \vec{H} + \frac{\vec{\omega}}{\gamma}$$

The application of a field of magnitude H_1, lying along the X^1-axis and rotating about the Z-(or Z'-) axis with frequency ω, in addition to the steady field H, produces a new effective field of magnitude

$$H_e = \left[\left(H + \frac{\omega}{\gamma}\right)^2 + H_1^2\right]^{\frac{1}{2}} \tag{8}$$

and making an angle Θ with the Z-direction given by $\tan \Theta = H_1/(H + \omega/\gamma)$. At resonance, that is, $\omega = -\gamma H$, the effective field is H_1 and the magnetic moment $\vec{\mu}$ precesses at an angular speed

$$\omega_{H_1} = \gamma H_1 \tag{9}$$

about the X^1-axis.

The spin-echo experiment starts from a situation with no rf field present and the magnetization at rest along the Z-axis (Fig.13a). At time t = 0 a rf pulse is applied during a time δt shown in Fig.12. The magnetization then rotates in the YZ-plane (Fig.13b) towards the Y-axis by an angle

$$\alpha = \omega_{H_1} \delta t \qquad (10)$$

The time δt is chosen such that $\alpha = \pi/2$. We call this a "90° pulse". Then at the instant of the removal of the pulse, the moment $\vec{M}$ will lie in the X', Y' plane (Fig.13c). A signal will be induced in the receiving coil because of the rotation of $\vec{M}$ in the laboratory system. Because of inhomogeneities in the applied field $\vec{H}$ and the distribution in local fields throughout the sample, certain regions of the sample will have slightly higher and other regions slightly lower precession frequencies. Suppose that the sample is composed of five regions, each called a spin isochromat [32]. Suppose one isochromat (labeled 0) precesses with frequency ω ($= -\gamma H$), whereas two (labeled +1 and +2) precess faster and the other two slower (labeled −1 and −2) than ω. In time the isochromats will fan out as shown in Fig.13d. Note that there will still be a net moment in the −Y'-direction; however, it is smaller than before, hence

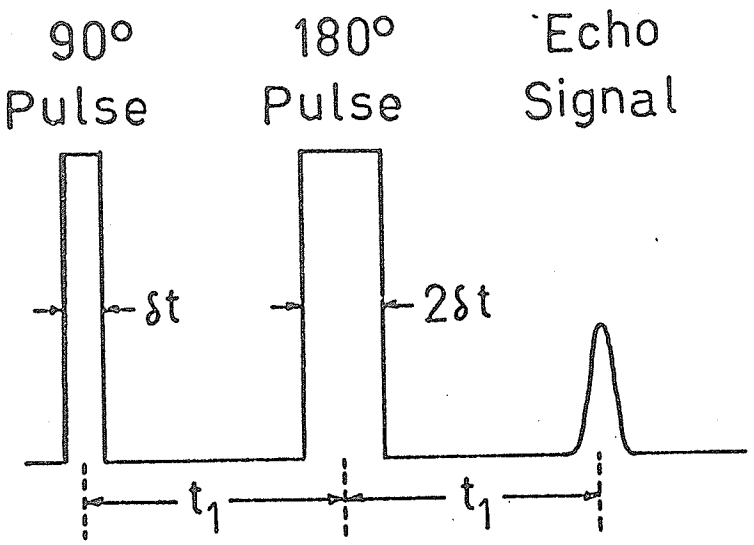

Fig. 12. A schematic diagram of the 90° and 180° rf pulses of NMR.

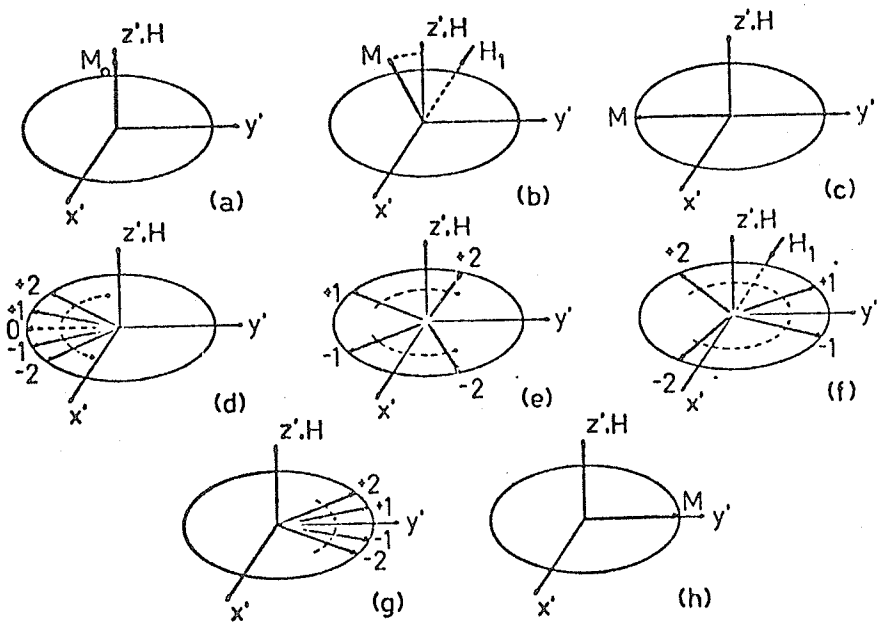

Fig. 13. A schematic diagram showing the formation of an echo in NMR (after E. L. Hahn).

the induced signal will begin to decay. At a later time $t = t_1$ the spin isochromats will be fanned out further (Fig.13e); there is no net moment in the X, Y plane and the induced signal will have decayed to zero. Now, we apply a pulse during a time $2\delta t$ (180° pulse) along X' axis. All the isochromats will thus be rotated through 180°, as shown in Fig.13f. An induced signal will appear in the receiver at the time of this rotation. The isochromats will still be precessing in the same sense, hence as time goes on, the isochromats will tend to become "unfanned" (Fig.13g). A resultant moment will be produced and a signal will begin to be induced in the receiver. At $t = 2t_1$ the isochromats will be in phase again and the echo signal will reach its maximum value. Then as time goes on, the spins will again fan out and the phase coherence will gradually be lost. This method works only if τ_2 is short compared to τ_1, and more specifically if τ_2 is mainly limited by spatial field-fluctuations rather than by spin-spin interaction. The latter interaction causes, by its random character, a loss of phase memory that cannot be restored. However, the use of a 90°-180° pulse sequence is not essential; induced spin echoes are observed for any pair of pulses [32].

2.7.2.1 DETERMINATION OF RELAXATION TIME

The height of the echo observed at time $2t_1$ is proportional to $\exp(-2t_1/\tau_2)$. Therefore by repeated application of pair

pulses with different t_1 a semi-logarithmic plot will provide a measure of the spin-spin relaxation time, τ_2. A typical plot is shown in Fig.14. This corresponds to the method A discussed by H. Y. Carr and E. M. Purcell [34].

2.7.2.2. MULTIPLE SPIN ECHOES AND AMPLITUDE MODULATION

The phenomenon, multiple spin echoes, has been observed in many magnetic materials [35] at $2t_1$, $3t_1$,..., where t_1 is the time interval between the two exciting pulses. The spin system can be described by the following general Hamiltonian in the rotating frame,

$$\mathcal{H}' = \sum_{i=1}^{N} \Delta\omega_{oi} I_{iz} + \sum_{i=1}^{N} a_i (I_{iz})^2 + \sum_{i<j}^{N} b_{ij} I_{iz} I_{jz} + \sum_{i<j}^{N} c_{ij} (\vec{I}_i \cdot \vec{I}_j) \qquad (11)$$

where the first term represents the Zeeman energy, the second term the quadrupole interaction, and the third and fourth terms describe possible spin-spin interactions. Theoretically, it is first discussed by Solomon suggesting that the formation is due to quadrupole interaction on I^{127} spin echo signal in KI. He assumed that the Zeeman energy is constant and the quadrupole coupling constantis inhomogeneously distributed. Recently, Abe *et al.* assuming just the opposite predicts, for the case where the excitation is carried out by two succeed-

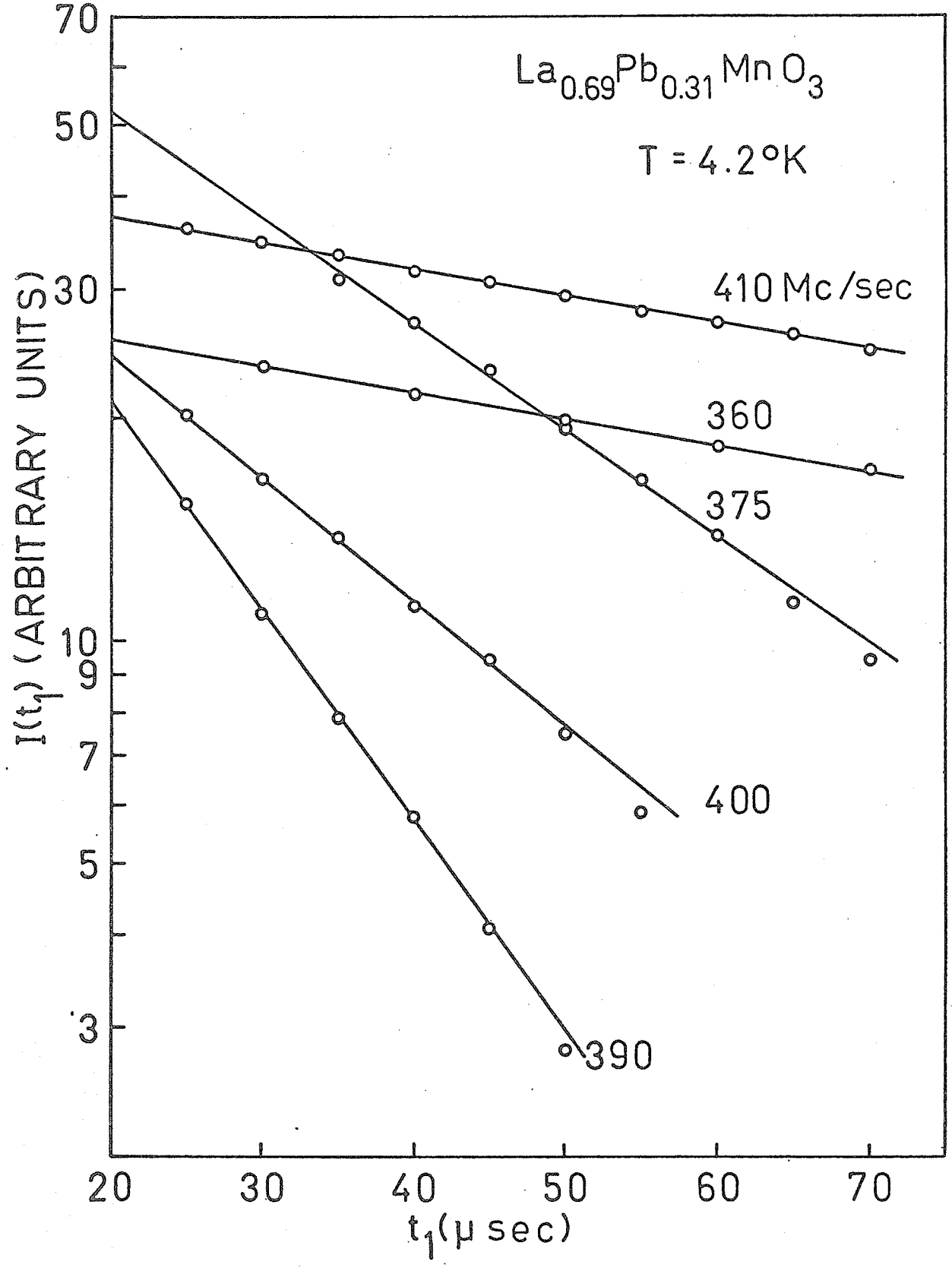

Fig. 14. A logarithmic plot of the spin echo amplitude with the time interval between the two of pulses as a parameter.

ing arbituary rf pulses, the maximum number of echoes to be 2I where I is the nuclear magnetic quantum number. The spin echo amplitude has an oscillatory behavior obeying $\Delta\nu_q \tau_m = 1$ where τ_m the modulation period and $\Delta\nu_q$ the frequency interval between two adjacent quadrupole split lines. These predictions agree very well with the results they obtained from the ferromagnetic materials MnB and Fe_2B.

More recently, Searle and Davis [35] in their mixed ferrite studies, manganese ferrite doped with nickel, observed Mn^{2+} multiple NMR spin echoes up to 22 at 1.6^{o} K and this is much bigger than 2I. They suggested that the formation of multiple echoes in this case is due to, instead of the quadrupole interaction, a nuclear spin-spin interaction, very likely the Suhl-Nakamura interaction [36] playing the part of the refocussing. The number of echoes thus predicted is infinite. Of course, the sensitivity of the instrument limits the number of observable echoes.

2.7.3. EXPERIMENTAL APPARATUS

The basic electronic setup is shown in the block diagram (Fig.15). The modulation controls the magnitude and the duration of the pulses which are generated by the pulse oscillator upon the triggering of the modulation. The cavity and the rf receiver are tuned first by using V.H.F. signal generator model 608E, and then the pulse oscillator is tuned by obtaining the maximum echo height on the oscilloscope. The dual pulse generator and

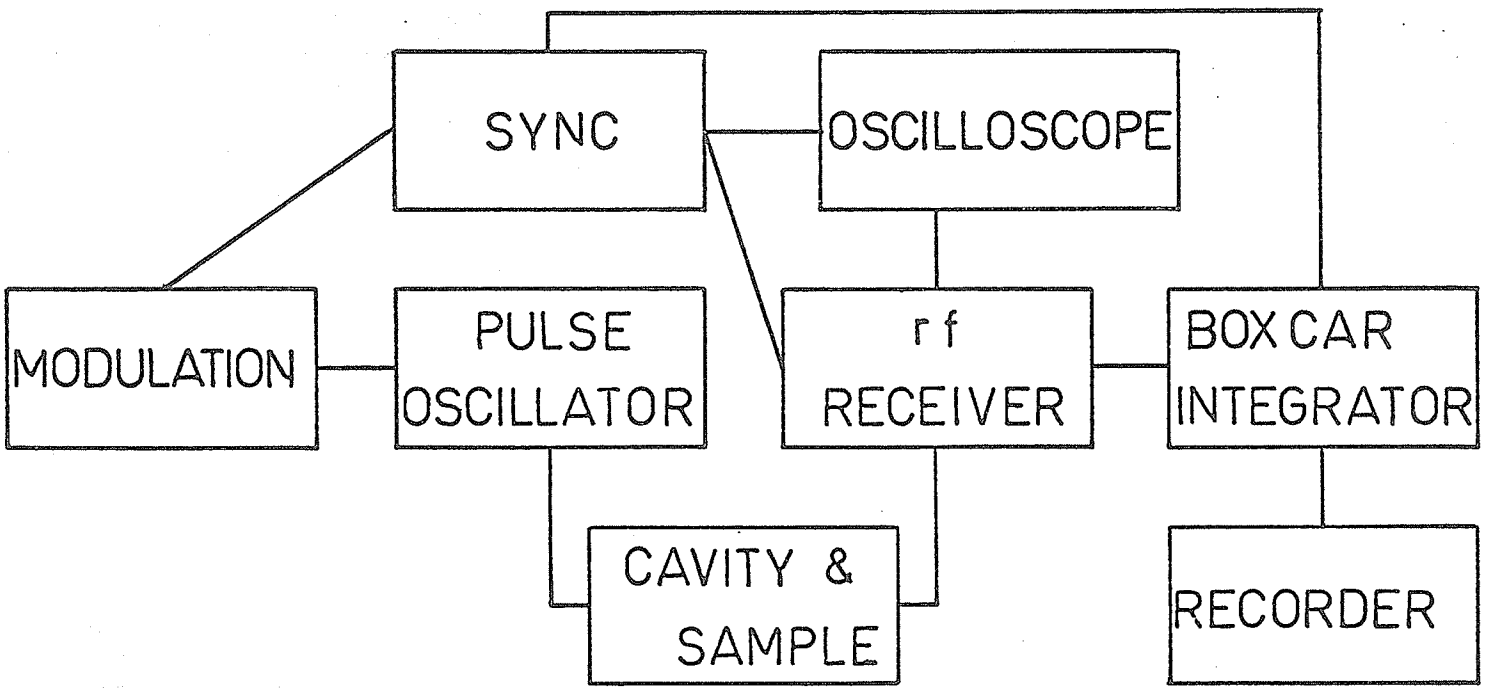

Fig. 15. A block diagram of the NMR setup.

receiver, model 6600, were manufactured by Matec Inc. The cavity used for nitrogen and helium temperature measurements without external field as well as the glass-dewar manufactured by Pope Scientific Inc. used for low temperature work are both shown in Fig.16.

The temperature below 4.2^{o} K was achieved by pumping the liquid helium with a mechanical pump and was determined by a manometer connected to the liquid helium chamber. 1.6 ± 0.1^{o} K can be attained by this simple method. The cylindrical cavity designed to be used in the electromagnet (maximum field 18 kOe) and the superconducting solenoid (50 kOe) is shown in Fig.17. The capacitor used is the air padding type manufactured by Hammarlund Mfd. Co., Inc. Because of the limited space available inside the tail piece of the dewar, the diameter of the cylindrical cavity is fixed while the length is determined by trial and error method.

2.7.4. METHODS OF DATA TAKING AND ANALYSIS

In section 2.7.2.1., we have pointed out that the amplitude of the echo at time $2t_1$ is proportional to $\exp(- 2t_1 / \tau_2)$. However, the relaxation time τ_2 is itself changing with frequency. Therefore, in making the measurement, it is not enough to use fixed t_1 and vary the frequency only, but rather we have to change the t_1 as well. The data taking thus becomes quite tedius.

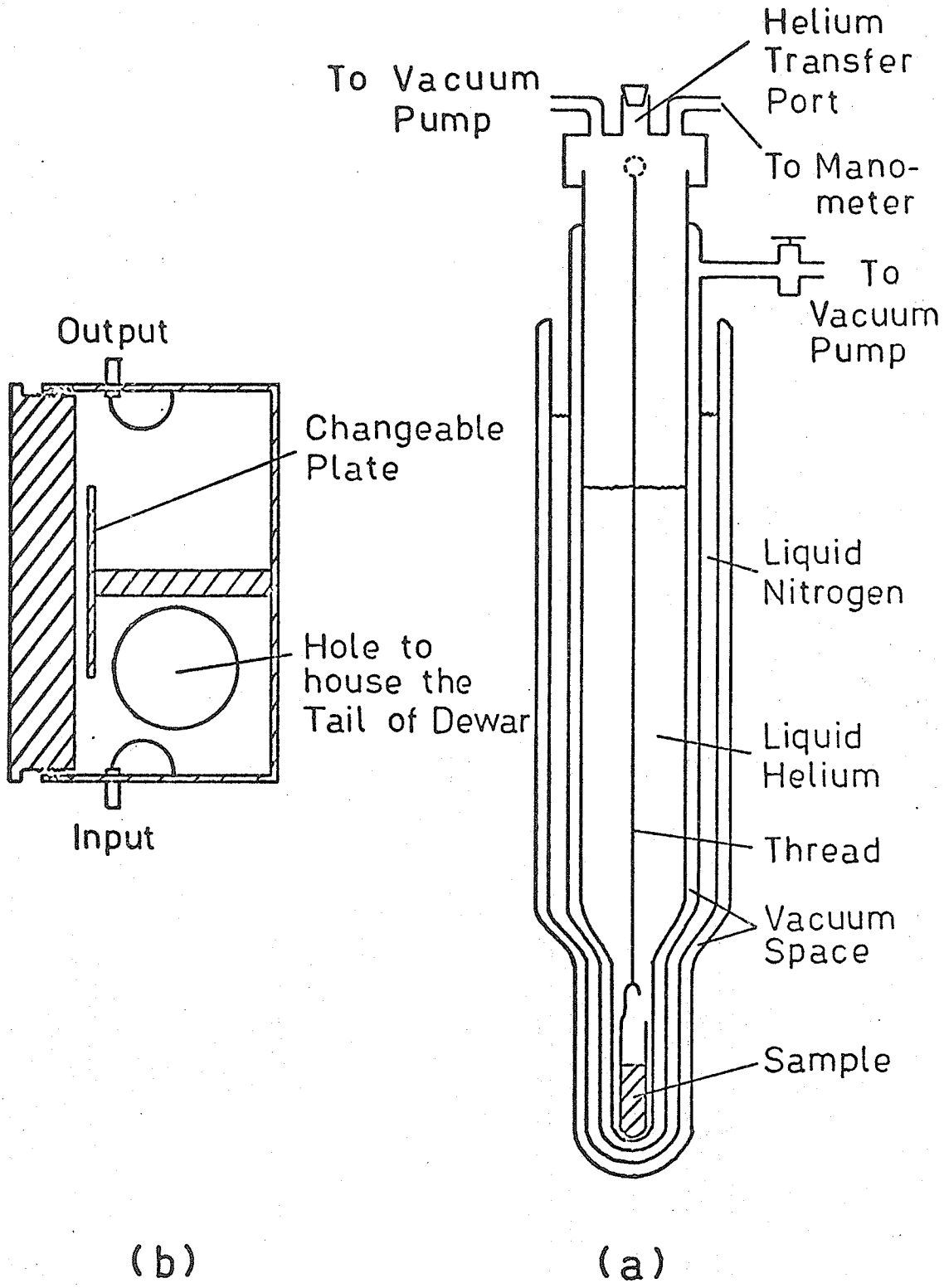

Fig. 16. Apparatus for NMR measurements . (a) A glass dewar for low temperature measurements. (b) A cylindrical cavity that can be used with the glass dewar.

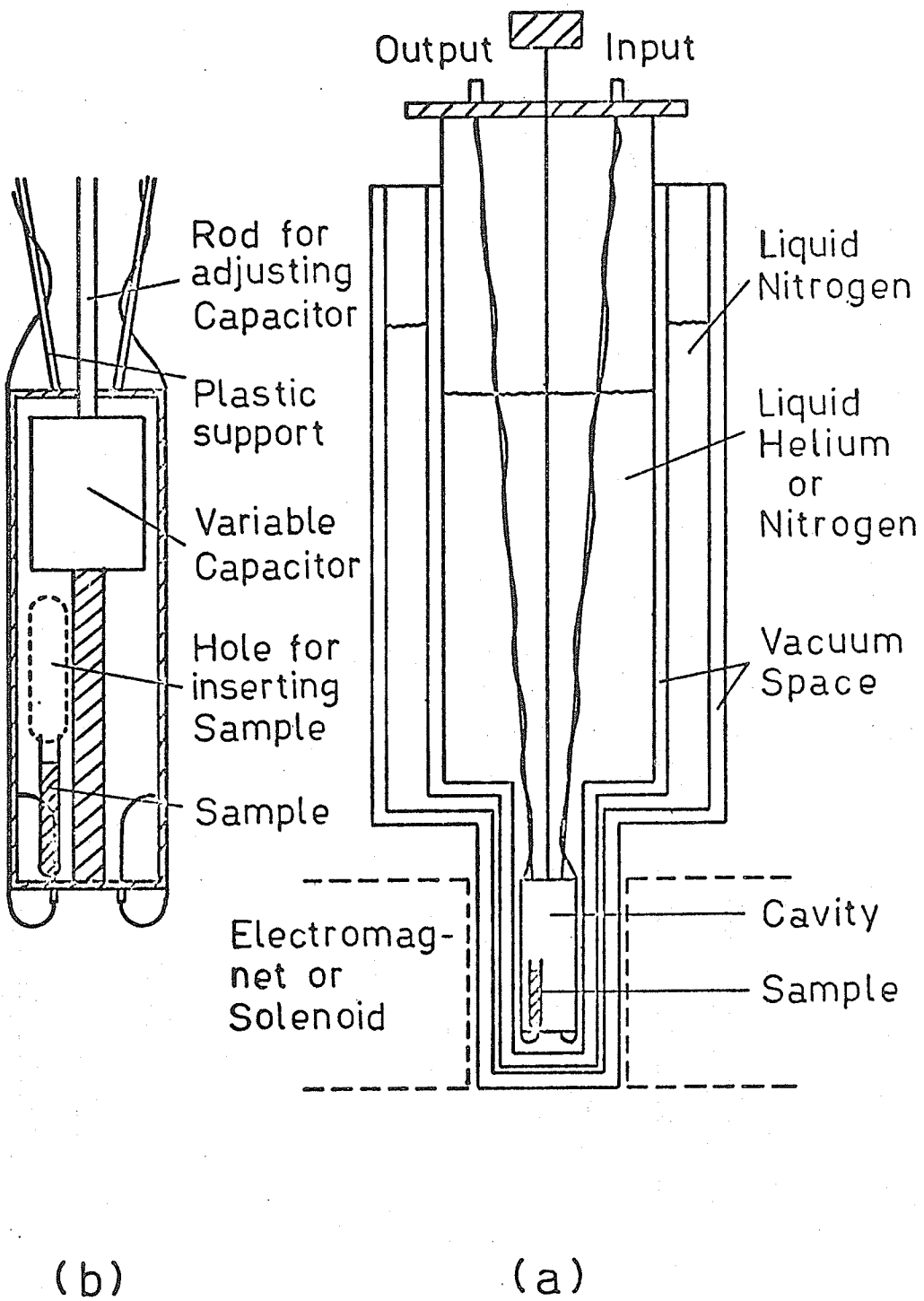

Fig. 17. Apparatus for NMR measurements. (a) A metal dewar that can be used for low temperature measurements with an electromagnet or a superconducting magnet. (b) A cylindrical cavity designed to be used inside the metal dewar.

In order to illustrate the importance of this step Fig.18a shows the data points taken at a fixed t_1 while Fig.18b shows the data points for the same sample taken with various t_1 and normalized [37] in such a way that the product of t_1 and τ_2 equals a chosen constant. The phenomenon that relaxation time varies as a function of frequency is also clearly illustrated in Fig.14. Since the power output is not very constant as the frequency is changed, certain precautions have to be made. The gain of the rf receiver and the pulse oscillator must be checked and kept constant at each frequency. However, since all these components are interconnected and interrelated and there are many other factors that will affect the pulse shape, the data thus obtained cannot be said to be completely free of error.

2.7.5. EXPERIMENTAL RESULTS

Measurements were made mainly on three samples of X values 0.26, 0.31 and 0.40 at temperatures 77° K, 4.2° K and 1.6° K.

2.7.5.1. MULTIPLE SPIN ECHOES

Multiple echoes were observed at 4.2° K but not at 77° K. In order to get the maximum number of echoes, the temperature was further lowered to $1.6 \pm 0.1^{\circ}$ K by pumping on the helium. For X = 0.26 five echoes were observed and for

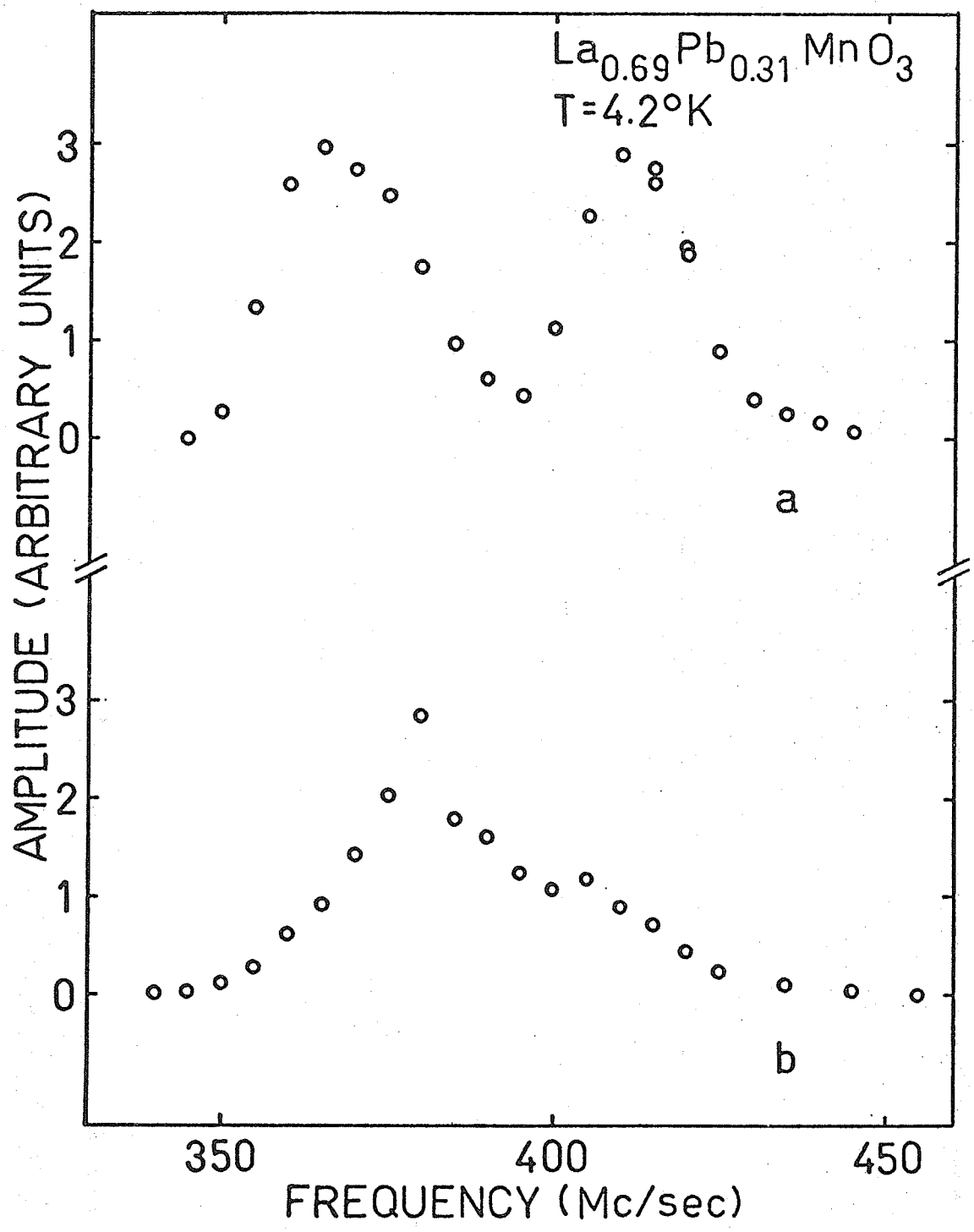

Fig. 18. NMR signals as a function of frequency. (a) With fixed time interval between the two pulses. (b) With various time intervals. However, the product of the relaxation time and the time interval between pulses is kept constant at all frequencies.

X = 0.31 only four echoes and their recorder traces are shown in Fig.19.

2.7.5.2. EXTERNAL STATIC MAGNETIC FIELD DEPENDENCE OF SPIN ECHO AMPLITUDE

Fig.20 shows the behavior of the echo amplitude, I, under the influence of an external field, H, for echo one and two. Fig.21 shows that if the data are plotted differently, the portion, at fields strong enough such that the complex contributions by domain walls can be removed, can be fitted nicely with a straight line.

2.7.5.3. RELAXATION TIME

Fig.22 is a plot of relaxation time versus frequency at 77° K and 4.2° K. It is also observed that the relaxation time is affected by the external static magnetic field and becomes longer as demonstrated in Table VI. Furthermore, the amplitude shows a sinusoidal behavior and it becomes more prominent as the external static field is increased as shown in Fig.23. If this modulation which has a period of $\sim 20\ \mu$sec. is indeed due to quadrupole interaction— the validity of which will be discussed in the following section — then according to A. Abragam [30], the Hamiltonian for the quadrupole interaction

$$\mathcal{H}_Q = \frac{e^2qQ}{4I(2I-1)}\left[\frac{1}{2}(3\cos^2\theta-1)(3I_z^2-I(I+1)) + \frac{3}{2}\sin\theta\cos\theta\right.$$
$$\left.[I_z(I_+ + I_-) + (I_+ + I_-)I_z] + \frac{3}{4}\sin^2\theta(I_+^2 + I_-^2)\right] \qquad (12)$$

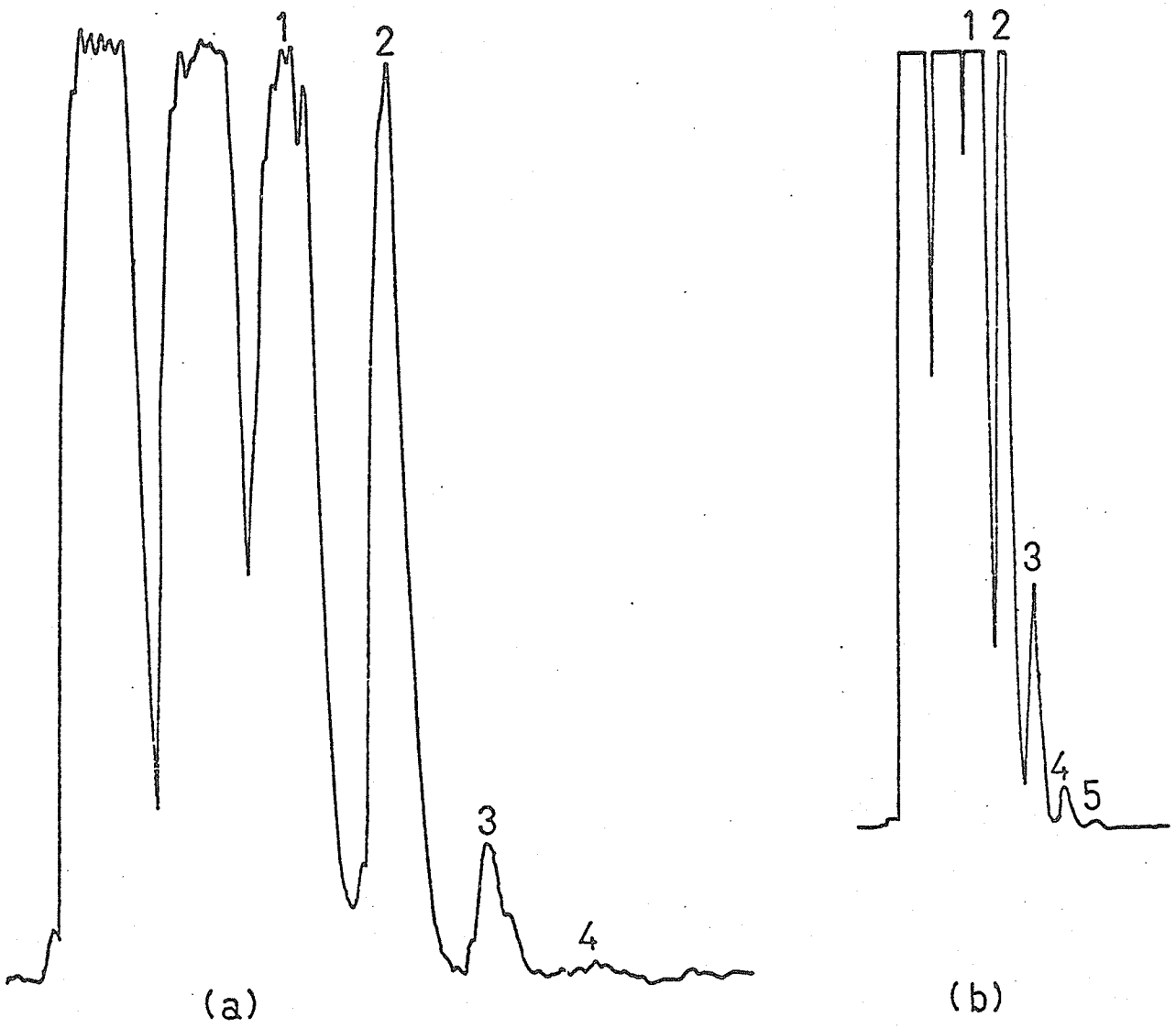

Fig. 19. Recorder trace of NMR signals for two compositions of $La_{1-X}Pb_XMnO_3$. (a) X = 0.31 (b) X = 0.26.

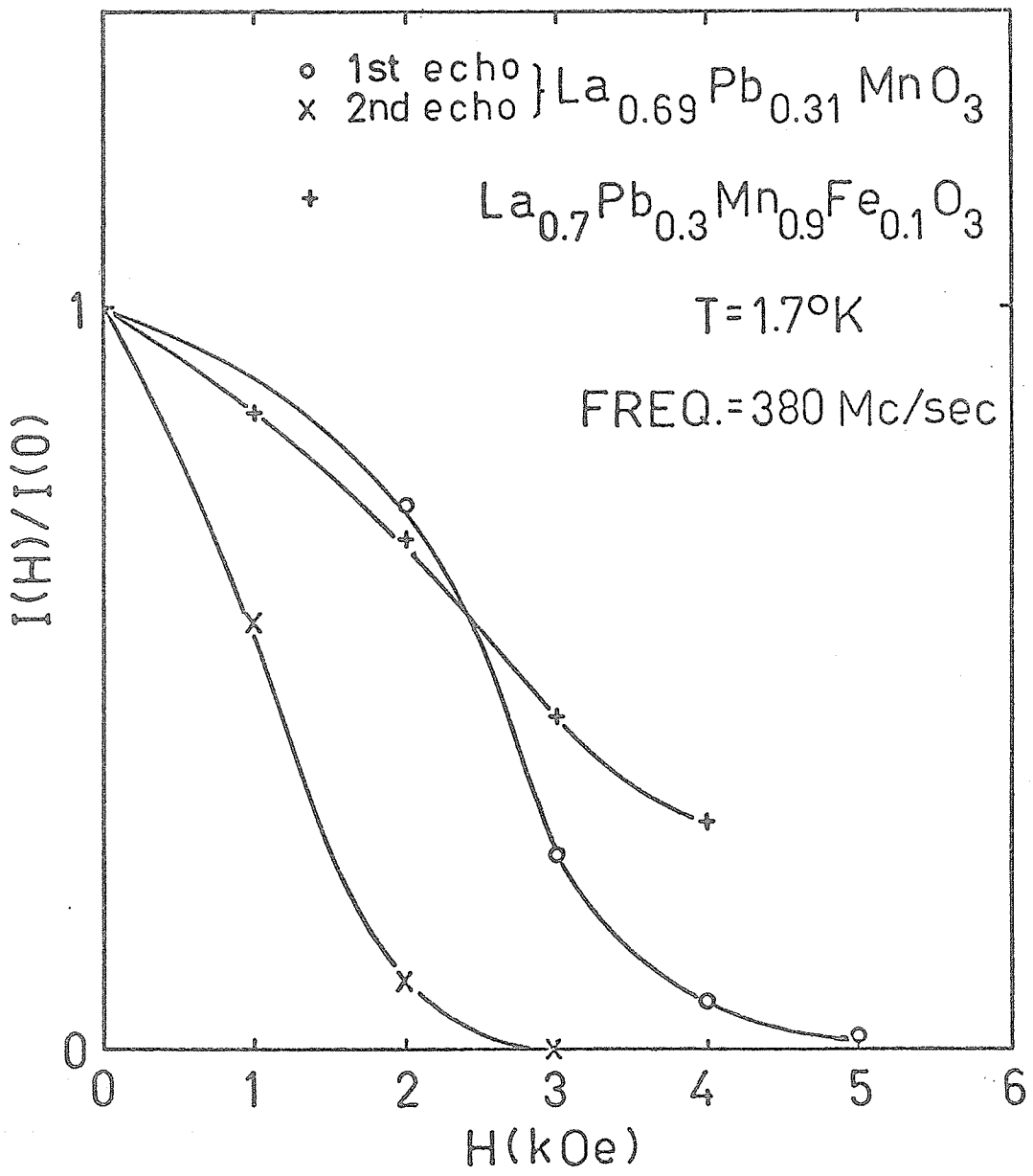

Fig. 20. Reduced intensity as a function of the applied field for the 1st and 2nd echo.

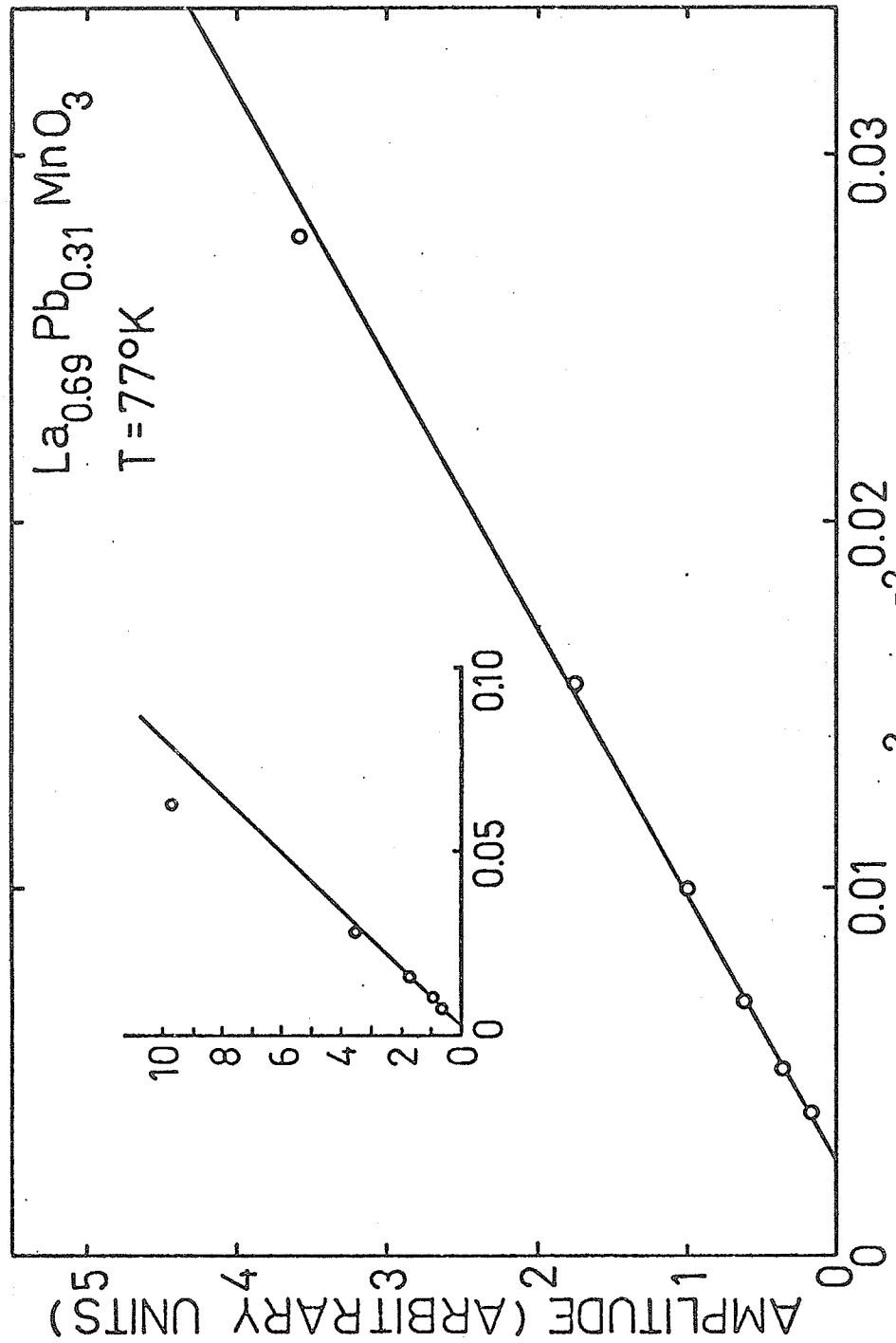

Fig. 21. Spin echo amplitude versus the inverse square of the applied field.

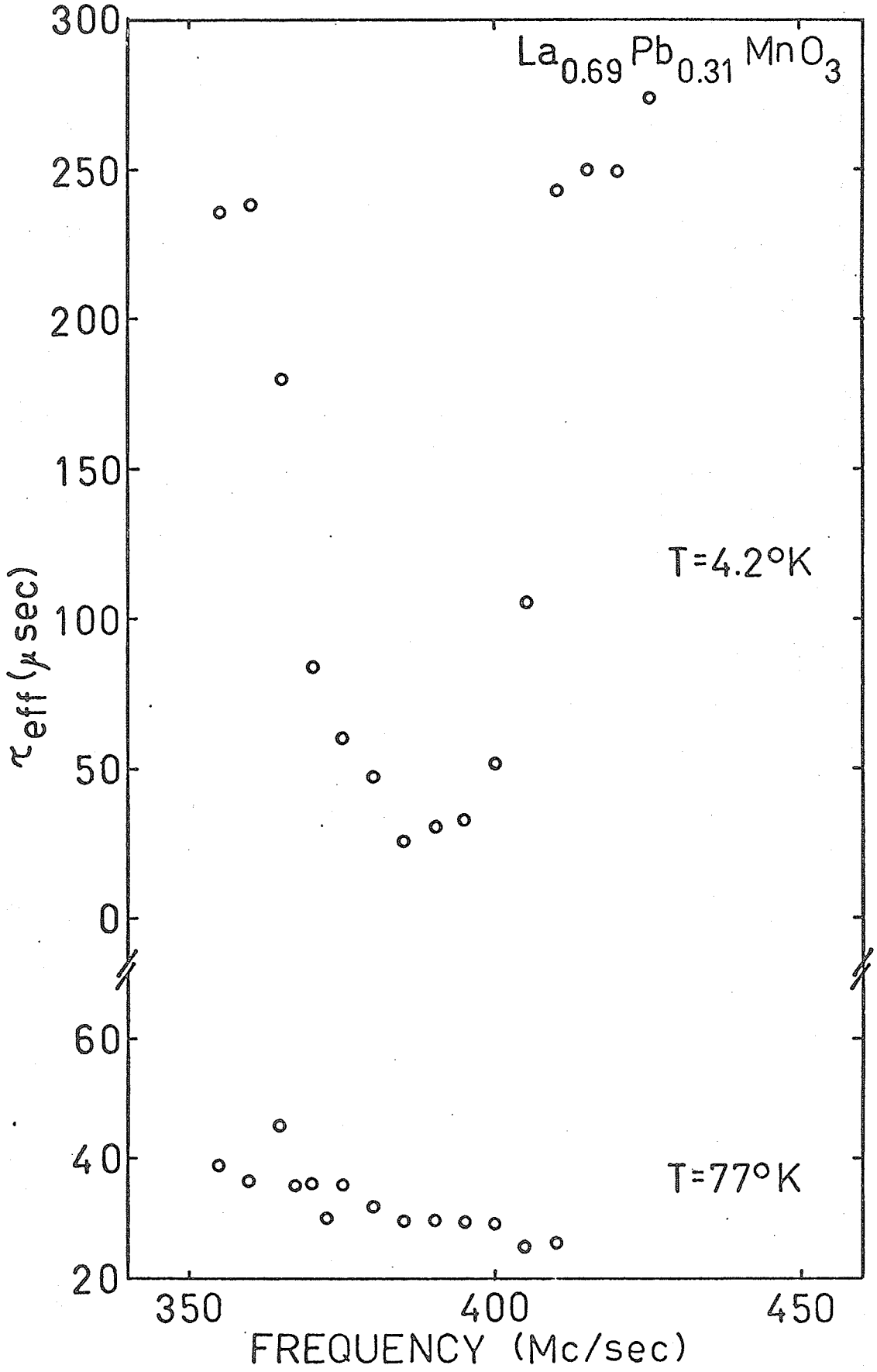

Fig. 22. . The effective relaxation time as a function of frequency.

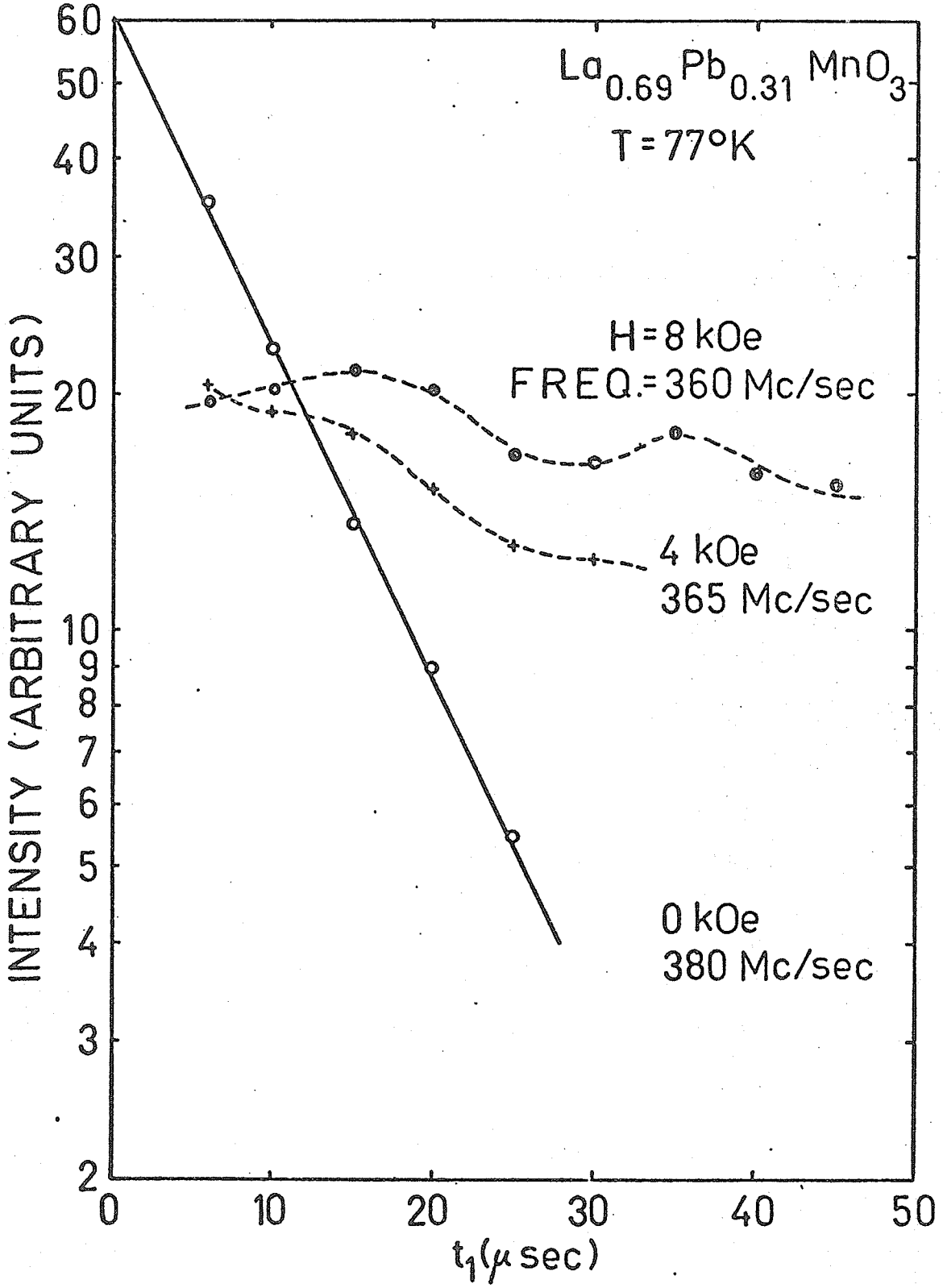

Fig. 23. The logarithmic plot of the spin echo amplitude as a function of the time interval between pulses in different external fields.

Table VI. The Resonance Frequency and Relaxation Time in Different Applied Fields.

Applied Field (kOe)	Frequency (Mc/sec)	$\tau_2 (10^{-6}$ sec)
0	380	10 ± 1
2	370	21 ± 2
4	365	46 ± 2
6	360	91 ± 5
8	360	190 ± 10
10	360	232 ± 10

and by standard first order perturbation

$$E_m^{(1)} = \frac{1}{4} h\nu_Q (3\mu^2-1)(m^2-\tfrac{1}{3}a) \qquad (13)$$

and

$$\Delta\nu_q = \frac{E_m^{(1)} - E_{m-1}^{(1)}}{h} = -\nu_Q (m-\tfrac{1}{2}) \frac{3\mu^2-1}{2} \qquad (14)$$

where

$$\nu_Q = \frac{3e^2qQ}{h2I(2I-1)} \; ; \; a = I(I+1) \; ; \; \mu = \cos\theta$$

Now if we assume the axis of hyperfine field and the symmetry axis of electric field gradient being parallel, i.e. $\Theta = 0$, and use the relation obtained by H. Abe et al.[35],

$$\Delta\nu_q \, \tau_m = 1 \qquad (15)$$

then from $\tau_m \sim 20\ \mu$sec., we find

$$e^2qQ/h \simeq 0.17 \text{ Mc/sec.} \qquad (16)$$

2.7.5.4. EXTERNAL STATIC MAGNETIC FIELD DEPENDENCE OF THE RESONANCE FREQUENCY

The enhancement of the nuclear resonance signal of a multi-domain particle is mainly due to nuclei in the domain walls and partly due to those in the domains. Here for (LaPb)MnO_3 which is known to have extremely low anisotropy [27] and strong exchange, the resonance frequencies due to nuclei in the walls and in the domains are expected to be almost the same [38]. As the applied magnetic field, H, is turned on, the domains start to align themselves along H but the effect of H is at first compensated by the demagnetizing field. Fig.24 shows that at $\sim$4 kOe applied field the sample is saturated, and from then on, the shifts in resonance frequency is due to direct interaction between H and the nuclear moment and can

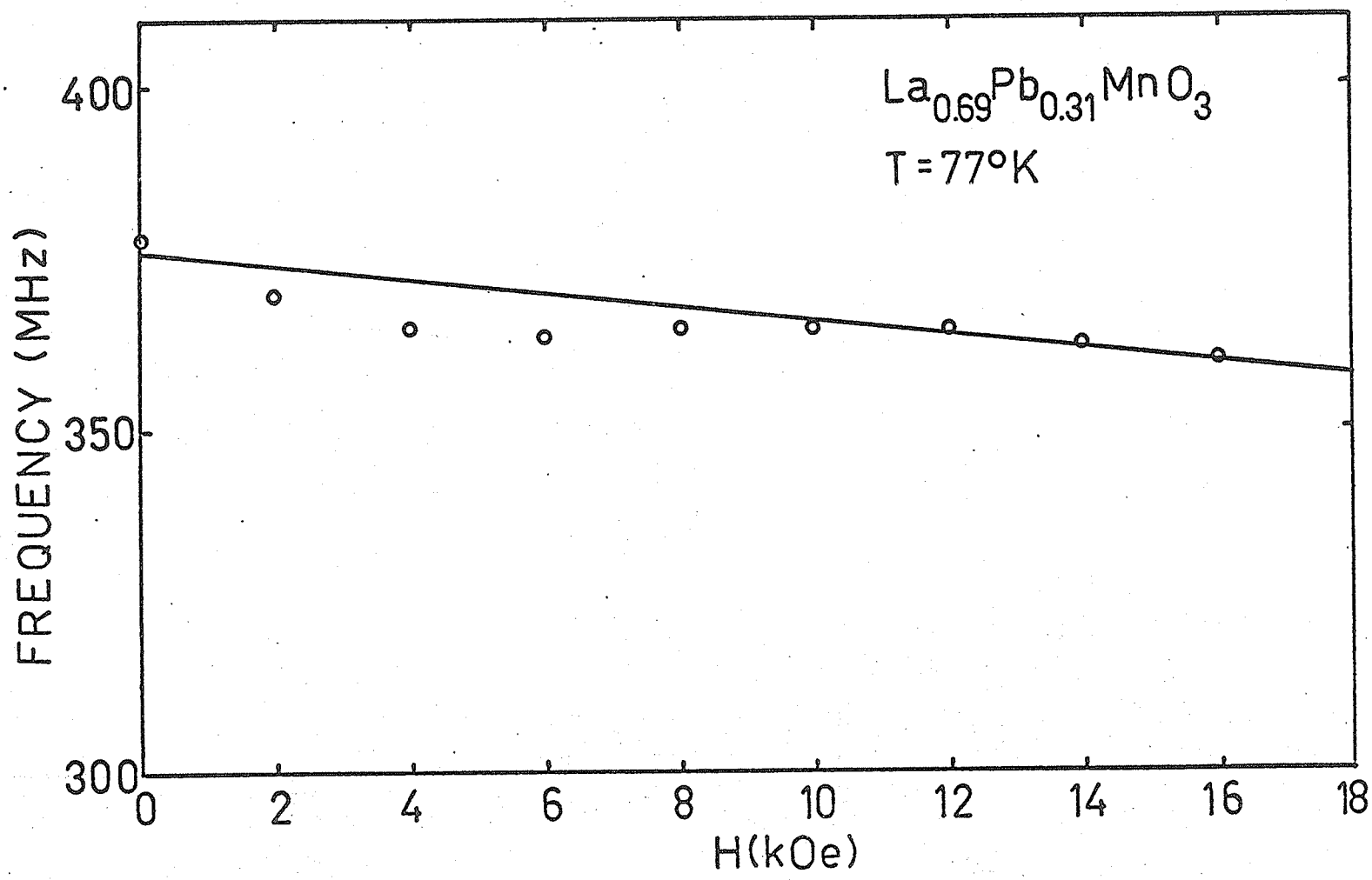

Fig. 24. Resonance frequency as a function of applied fields.

be described by the equation

$$\vec{\omega} = \gamma_N[\vec{H}_{hf} + (\vec{H} - \vec{H}_D)] \qquad (17)$$

where H_{hf} is the nuclear hyperfine field and H_D the demagnetizing field. H_D can be estimated to be between $4\pi/3M_S$ and $4\pi M_S$, which are, in this case, ~ 3 kOe and ~ 9 kOe respectively. The slope of the curve gives a gyromagnetic ratio of nuclei $\gamma_N \simeq 2\pi \times 1000(\text{Oe-sec.})^{-1}$. The negative slope indicates that the hyperfine field is indeed negative as expected.

2.7.5.5. EXTERNAL STATIC MAGNETIC FIELD DEPENDENCE OF THE SPIN ECHO LINE SHAPE

The amplitudes of the echoes at various external fields have been normalized to the same magnitude as shown in Fig.25 for the sake of easy comparison on the line width. The line width at zero external field is ~ 34Mc/sec and it decreases as the field increases. Further, it is observed that the amplitude is greatly reduced if instead of powder, whole single crystals are used.

2.7.5.6. RESONANCE FREQUENCY AND SPECTRUM

The nuclear spins are coupled to the electronic spin by the hyperfine coupling

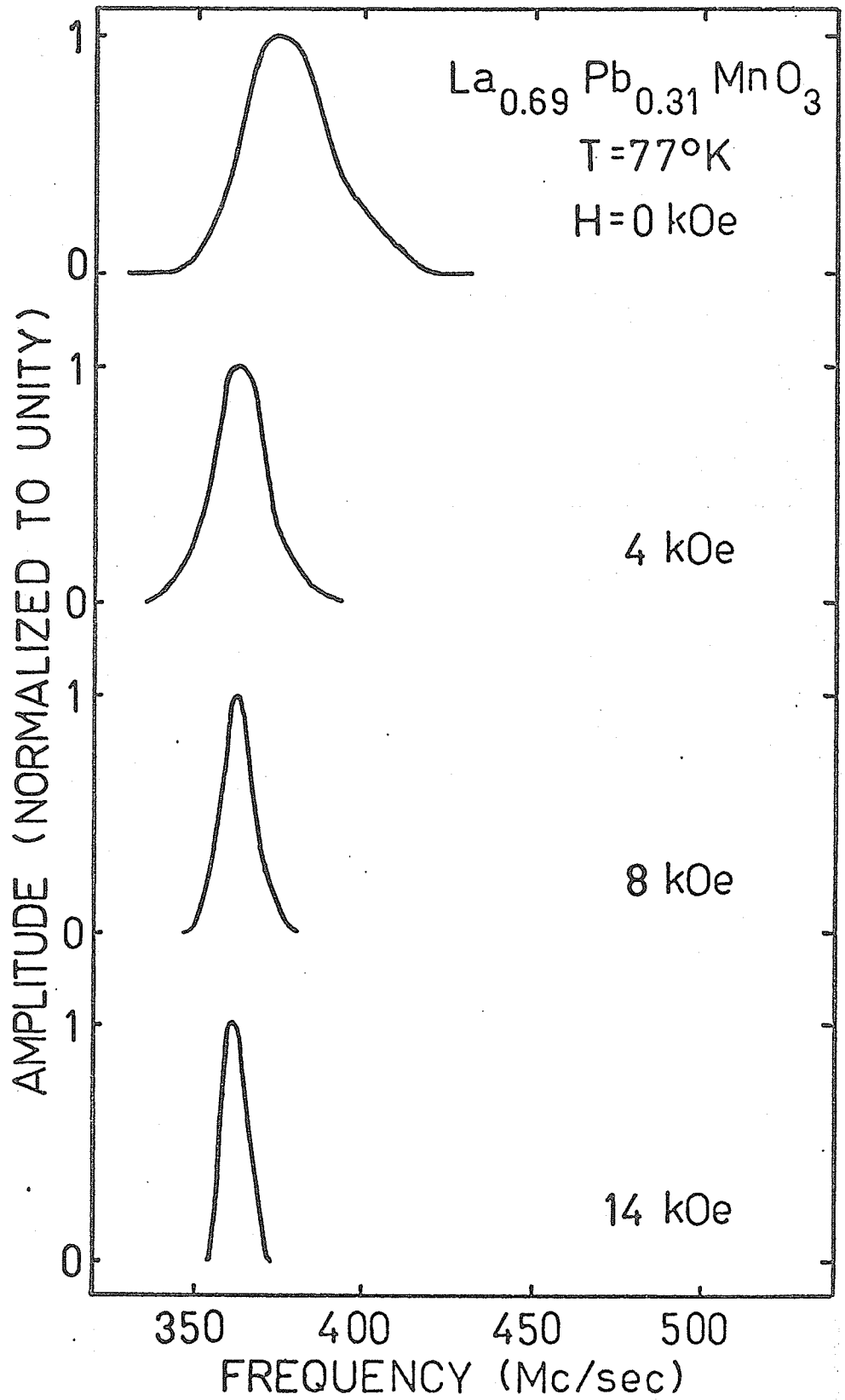

Fig. 25. The NMR spectrum in different external fields.

$$\mathcal{H}_{hf} = \sum_i A\vec{I}_i \cdot \vec{S}_i \qquad (18)$$

The nuclear resonance energy is obtained by replacing $\vec{S}$ by its mean value,

$$\langle \mathcal{H}_{hf} \rangle = \sum_i AI_z^i \langle S^i \rangle \qquad (19)$$

and then

$$\nu_i = A \langle S_z^i \rangle / h \qquad (20)$$

which is proportional to AM(T) and at very low temperature to AS. The resonance frequencies for the three chosen samples at 4.2° K and 77° K are tabulated in Table VII and the spectra

Table VII. Results of Data Analysis of NMR Spectra for $La_{1-X}Pb_XMnO_3$.

X	T ($^\circ$K)	Resonance Frequency (Mc/sec)	A ($cm^{-1} \times 10^{-3}$)	H_{hf} (kOe)
0.26	4.2	390 ± 2	7.0 ± 0.1	-377 ± 6
0.31	4.2	380 ± 2	6.9 ± 0.1	-369 ± 6
0.40	4.2	376 ± 2	6.8 ± 0.1	-365 ± 6
0.31	77.0	376 ± 2	———	-365 ± 6

are shown in Fig.26. From the magnetization, $\langle S_z \rangle$ is calculated and then the hyperfine field coupling constant, A, is deduced and also tabulated in Table VII. In the calculation g is assumed to equal two.

2.7.5.7. RELAXATION TIME OF 1st AND 2nd ECHOES

The relaxation time τ_2 near the resonance frequency for X = 0.31 was determined at temperatures 4.2° and 1.7° K for the first and second echoes and the results tabulated in Table VIII. It is observed that the relaxation time as a function

Table VIII. Relaxation Times of 1st and 2nd Echo.

	Frequency (Mc/sec)	Temperature (°K)	τ_2 (μ sec)
1st echo	385	4.2	42.6 ± 0.5
	380	1.7	44.2
2nd echo	385	4.2	15.4
	380	1.7	14.9

of temperature is almost constant within experimental error and the relaxation time of the 2nd echo is much faster ~1/3 of that of the 1st echo.

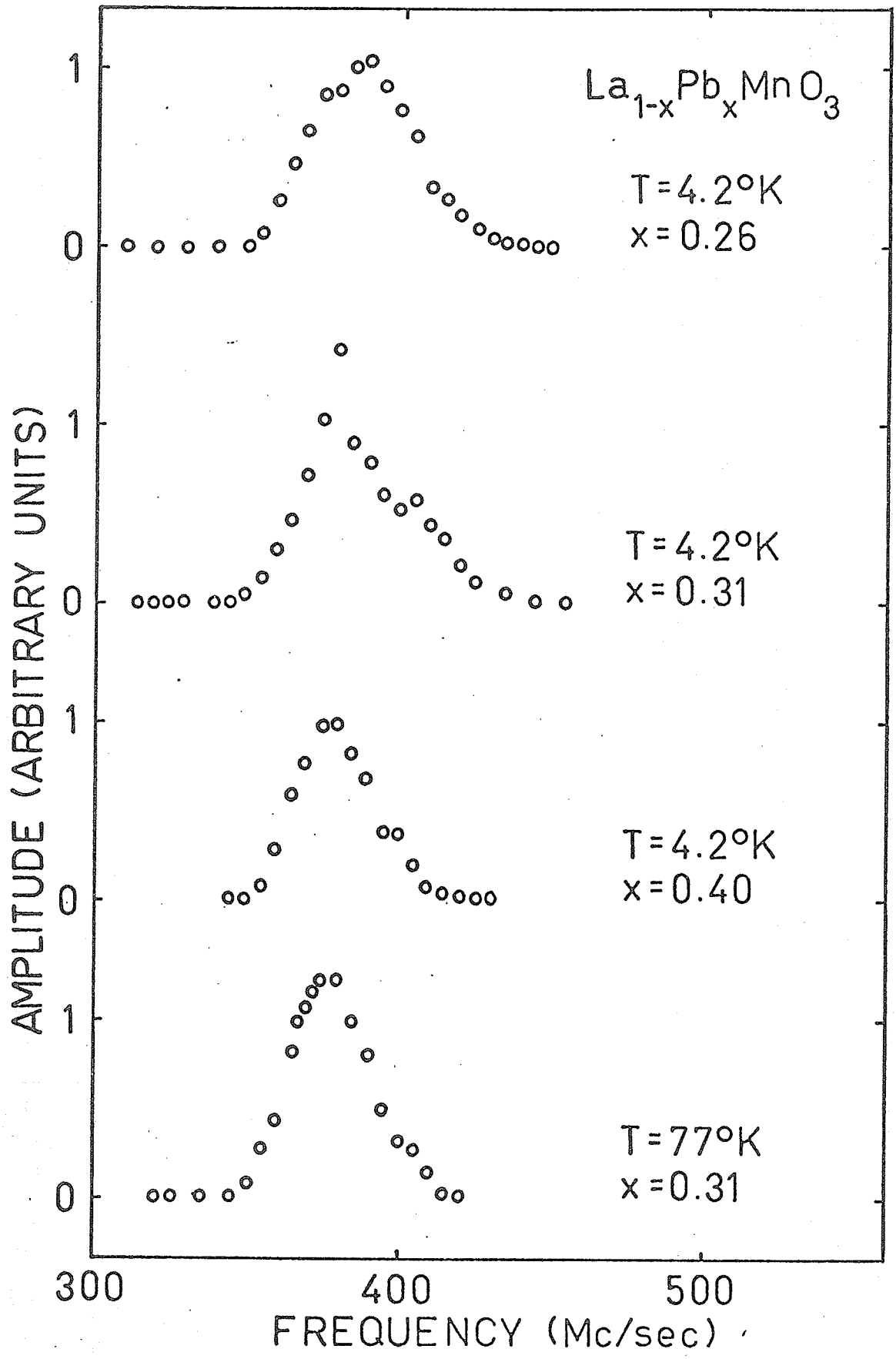

Fig. 26. NMR spectra of $La_{1-X}Pb_XMnO_3$ with $0.26 \leq X \leq 0.4$.

2.8 DISCUSSION

2.8.1 STATIC MAGNETIZATION

The shape of the magnetization versus temperature curves was considered with respect to standard theories. In Fig.27 the Brillouin function for $\langle S \rangle = 1.84$ fitted to the experimental data on $La_{0.69}Pb_{0.31}MnO_3$ at T = 0 and 250°K, is plotted as a dashed line. The agreement is respectable below 300°K ($T/T_c < 0.9$). If the data had been fitted at absolute zero and the Curie temperature, the theoretical curve would obviously have fallen well below the experimental points. A rather good fit was obtained for $0 \lesssim T/T_c \lesssim 0.9$ by using an equation [39] of the form

$$[M(0) - M(T)]/M(0) = AT^x \qquad (20a)$$

where x has a value of ~ 2.7. The rapid drop in magnetization near the Curie temperature was thought to have its origin in lattice distortions. This lead to a calculation done by Oretzki and Gaunt [26] in which they fitted the magnetization versus temperature curves using a molecular field approach with an exchange energy given by

$$E_{ex} = -\frac{3}{2}\frac{S}{S+1} kT_c \left[\left(\frac{M}{M_o}\right)^2 + 0.125\left(\frac{M}{M_o}\right)^4\right] \qquad (21)$$

and the fit is reasonable. In order to explain this quartic coefficient of 0.125, a few percent change in volume is needed.

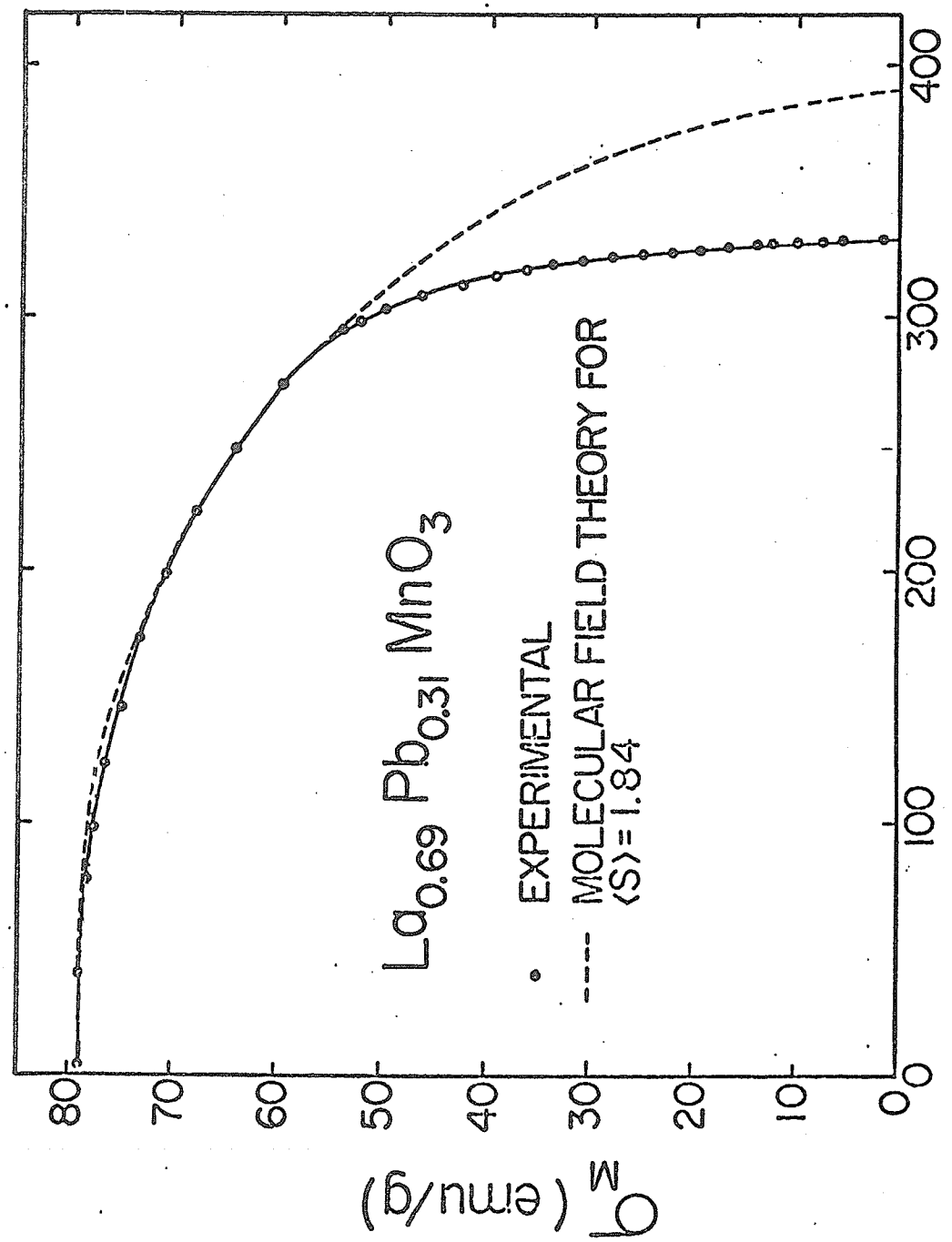

Fig. 27. Saturation magnetization as a function of temperature fitted with various theoretical models.

However, using a powdered sample of $La_{0.62}Pb_{0.38}MnO_3$, they did not find any volume or distortion anomaly of order 1% just below the Curie temperature and they concluded that the quartic term required to explain the magnetization can not have its origin in a volume-or distortion-dependent exchange energy constant.

The correlation between the spontaneous magnetization and the electrical resistivity was first noted by Van Santen and Jonker [9] and in turn led Zener [1] to propose the double-exchange interaction. In Fig.28, the spontaneous magnetization at a given temperature for $La_{0.69}Pb_{0.31}MnO_3$ is plotted against the corresponding resistivity for the entire range from 77° K to the Curie point. Near T_c, the magnetizations obtained by the thermodynamic method are used. Clearly, the relationship between σ_M and ρ is close to linear, although the deviations may be significant.

The high correlation between the magnetization and the electrical conductivity suggests that they have similar origins, viz. in electron double exchange between the Mn^{3+} and Mn^{4+} ions involving the intermediate O^{2-} ions. For the ensemble of Mn^{3+} - Mn^{4+} ions, there will be a large number of configurations that have the same or almost the same energy. The electrons involved in the double exchange will have Bloch-like wave functions that extend over the entire crystal and

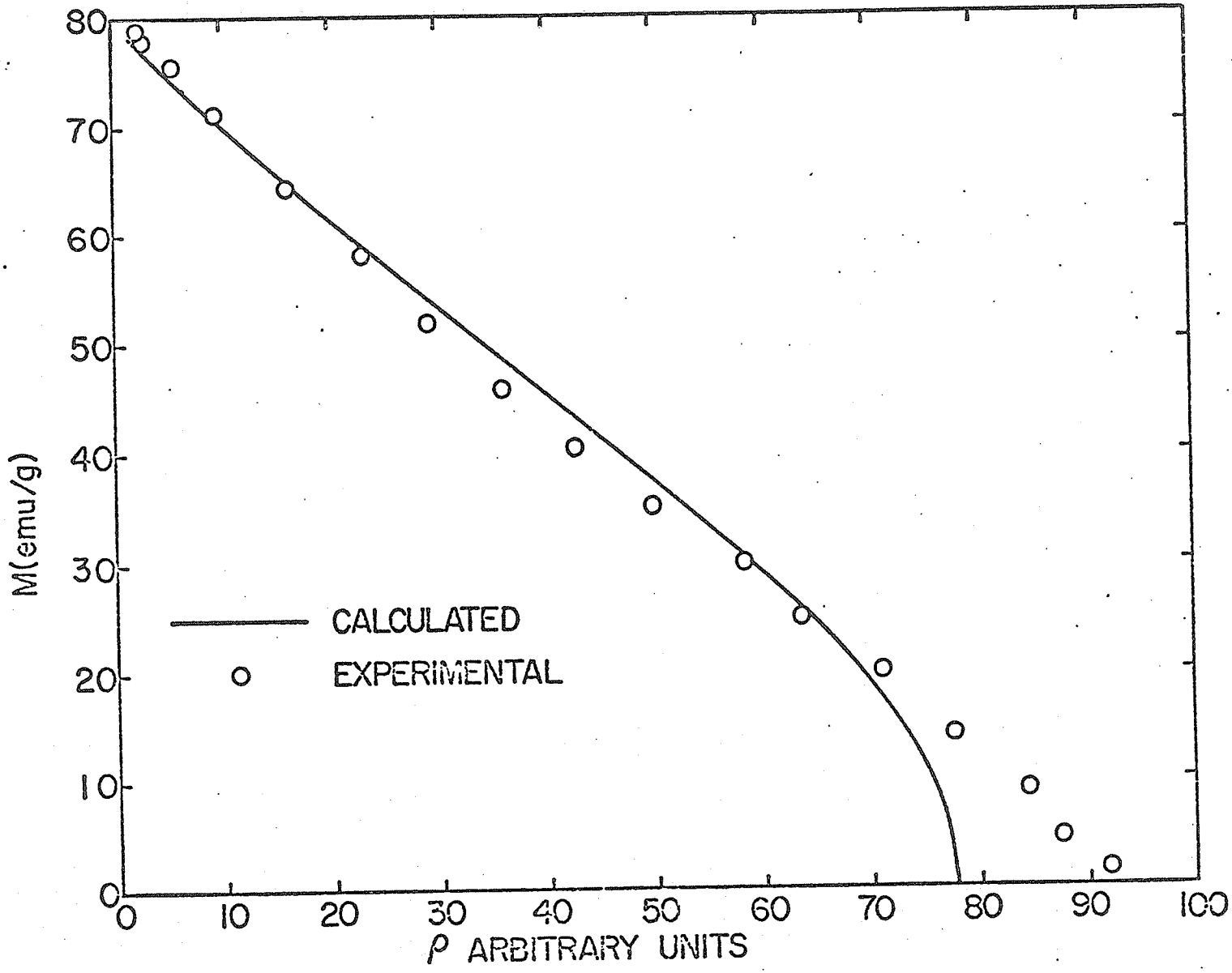

Fig. 28. Saturation magnetization versus electrical resistivity at all temperatures below T_c. The solid curve is calculated by Searle and Wang [40].

will lie in an unfilled, albeit narrow, band. The interaction between the localized 3d electrons of the Mn^{4+} ions via an itinerant electron, which is just Zener's double-exchange interaction, is ferromagnetic. The rapid decrease in the magnetization on the approach to the Curie point would, in this picture, be the result of a collapse of the double-exchange electron band, implied by the rapid corresponding increase in resistivity.

A model based on the resistivity and magneto-resistance data was developed by Searle and Wang [40] to explain the correlation between resistivity and magnetization. They argued that since the conduction band was strongly spin-polarized suggested by the data, the average effective exchange energy (between the band spin, S, and the ion-core spins $S_{d'}$) $-\Delta E = -K \langle S_Z \rangle \langle S_{d_Z} \rangle$ was required to be greater than the Fermi energy E_F, that is,

$$\Delta E/E_F > 1 \qquad (22)$$

However, most of the other rigorous calculations [41] assume just the opposite and thus cannot be used. Based on this, they arrived at an equation,

$$\rho = \frac{C}{N} \frac{1 - (M(T)/M(0))^2}{1 + (M(T)/M(0))^2} , \qquad (23)$$

which gave a good fit with the magnetization data shown in Fig.28 and Fig.29.

In the theory proposed by De Gennes [10], the competition between the ferromagnetic double-exchange interaction and the antiferromagnetic superexchange interaction will lead to a canted ferromagnetic arrangement for certain compositions. However, the agreement between the magnetization observed at $T = 0^{o}$ K and that expected from the chemical composition (Table IV) implies that any canting must be slight, provided of course that there is no appreciable orbital contribution to the magnetic moment. By the same token, the electrons in the double-exchange band must be fully polarized at absolute zero.

2.8.2. SUSCEPTIBILITY

The susceptibility above the knee of the magnetization curve (M versus H, Fig.3) is about 10^{-4} emu/gOe at low temperatures. This large value could possibly have its origin in a small canting of the manganese moments. Experiments at higher applied fields should be informative.

At the Curie temperature, the collapse of the double-exchange band would be complete, and hence at higher temperatures all the magnetic electrons would be localized at a given instant of time to form a random distribution of Mn^{3+} and Mn^{4+} ions. Under these circumstances, it is reasonable to expect a Curie-

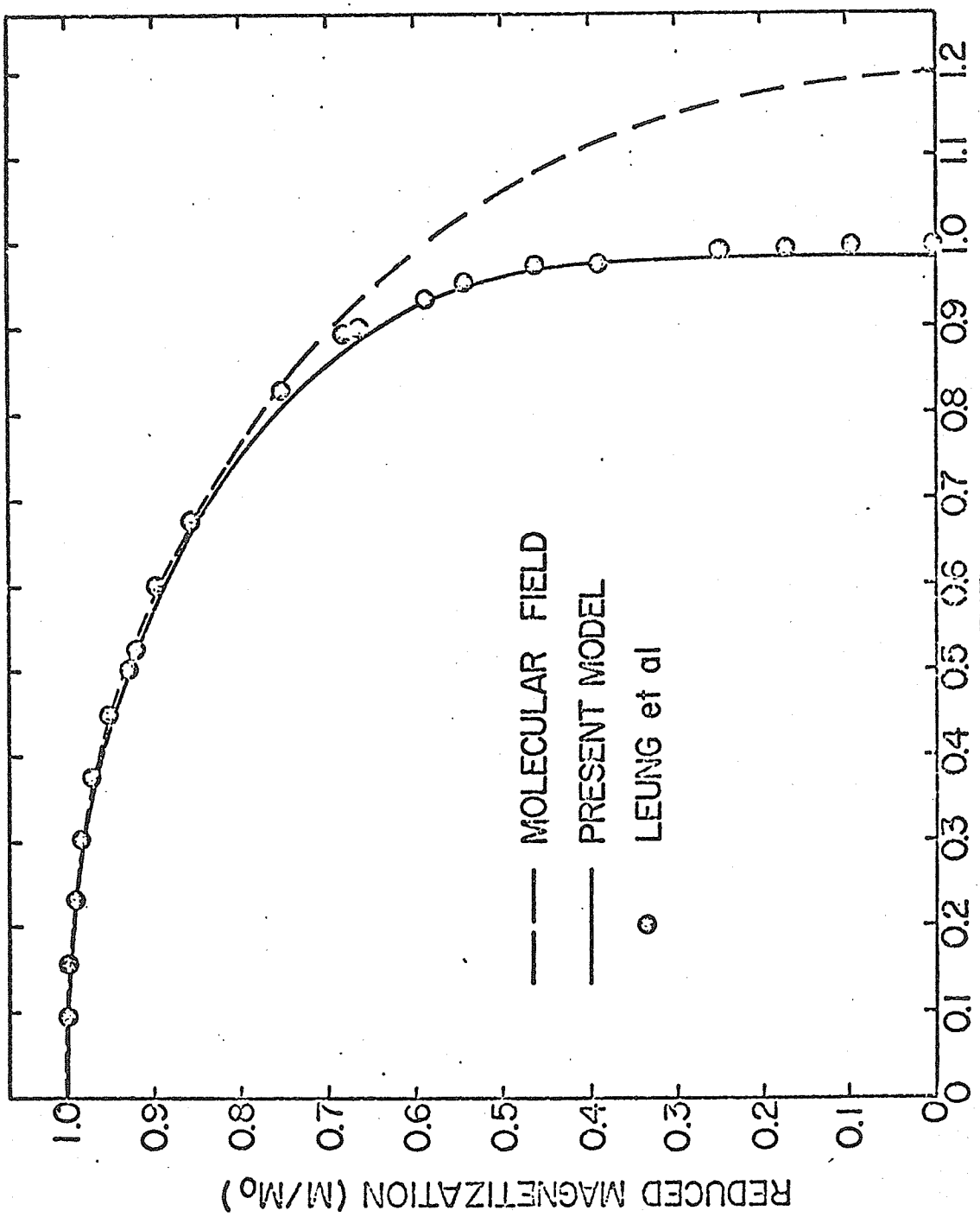

Fig. 29. Reduced magnetization as a function of reduced temperature with theoretical fit done by Searle and Wang [40].

Weiss behavior, as indeed has been predicted by Anderson [42], who has withdrawn an earlier incorrect prediction [3]. A small curvature in the reciprocal susceptibility versus temperature curve above T_c (Fig.5) is predicted by the series expansion and the Bethe-Peierls-Weiss theories of ferromagnetism, and is essentially the result of short-range order persisting.

2.8.3. CRITICAL EXPONENT

The values in Table V agree reasonably well with that found in $YFeO_3$ [20] ($\beta = 0.55 \pm 0.04$, D = 3.9) and Fe_3O_4 [21] ($\beta \simeq 0.53$, D $\simeq$ 3.5). In 1965, D. G. Howard et al. [22] reported that they found for Fe in Ni a $\beta \simeq 0.3$ for $T/T_c > 0.996$ and $\beta = 0.51 \pm 0.04$ for $0.996 < T/T_c < 0.9995$. As far as theoretical work is concerned, Landau's theory [16-17] of second-order phase transitions predicts that independent of model, $\beta = 0.5$, although the assumptions used in the derivation are not universally valid [23]. Calculations based on Ising three dimentional model all give $\beta \simeq 0.3$. However, Gallen and Callen [24] did predict such a change in β for Heisenberg ferromagnets as the temperature approaches T_c. Kadanoff [25] et al. suggested that this change could be due to the dipole force which is much weaker than the exchange forces at low temperature predominating at temperature near T_c. Since the dipole force is long-range, it might be expected to produce qualitatively different critical behavior from that

produced by the short-range exchange forces. This could be the explanation for our β value. The sudden drop in the magnetization curve could indicate the disappearing of the double-exchange force while the long-range dipole force persists since the rhombohedral distortion remains far beyond the Curie point [26].

2.8.4. NMR

2.8.4.1. MULTIPLE SPIN ECHOES

The number of echoes at temperatures 4.2 and 1.6° K is always less than or equal to 2I and does not change drastically with temperature. For the composition, X = 0.26, there are four at 4.2° K and only five at 1.6° K. However, in the manganese ferrite studies [35], Searle and Davis observed two or three at 4.2° K and about twenty-two at 1.6° K and Hirai and Fukuda in Japan observed eight at 1.6° K and about twenty-two at 0.4° K. The Suhl-Nakamura interaction is important only at very low temperature, therefore, we would expect it to be extremely sensitive in temperature change. Furthermore, we observed modulation on the spin echo amplitude when an external magnetic field was applied as shown in Fig.23. The ratio of the relaxation times between the first and second echo is ~ 3 while in [35] ~ 2. All these suggest that the mechanism of forming multiple spin echoes in this particular compound $(LaPb)MnO_3$ is quite different from that of the manganese ferrite and favor the mechanism that is due to the effect of quadrupole

interaction.

2.8.4.2. EXTERNAL STATIC MAGNETIC FIELD DEPENDENCE OF SPIN ECHO AMPLITUDE

The reduction of the spin echo amplitude in the presence of an external applied field is in fact due to the reduction of the enhancement factor, η , which can be worked out simply as follows. The effect of transverse of field, H_X, is to turn the electron magnetization M through an angle $H_X/(H_a - H_D + H)$, thus establishing a transverse magnetization

$$M_x = M \frac{H_x}{H_a - H_D + H} \qquad (24)$$

where H_a is the static anisotropy field acting on the electron, H_D is the demagnetizing field and H is the external applied field. Since the hyperfine field points to the opposite direction of the magnetization M, it also is rotated through this same small angle. The nuclei then see an effective transverse field

$$H_{eff} = H_x + \left(\frac{M_x}{M}\right) H_{hf} = \left(1 + \frac{H_{hf}}{H_a - H_D + H} \right) H_x \qquad (25)$$

The transition probability, and thus the absorption rate, will then be enhanced by the factor

$$\eta' = (1 + \frac{H_{hf}}{H_a - H_D + H})^2 = (1 + \eta)^2 \qquad (26)$$

as the external field becomes strong enough such that H_a and H_D may cancel each other and since H_{hf}/H is of order 100, then to a good approximation,

$$\eta' \simeq (\frac{H_{hf}}{H})^2 \qquad (27)$$

We have shown in Fig.21 that this is indeed the case.

2.8.4.3. RELAXATION TIME

Fig.22 shows that there is a minimum in the effective relaxation time near the resonance frequency at 4.2° K but this effect is not observed at 77° K. Similar effect was also observed in the ferrite studies [35] where a model based on the clustering of spin was used for the explanation. Of course, in a mixed oxides as this, clustering is known to exist quite frequently. However, we believe that this effect connects with the spin-spin relaxation mechanism in a more basic way because at 77° K where the spin-lattice relaxation can no longer be neglected this effect is completely washed out. The absorbed energy at such low temperature can be dissipated only by direct

or indirect nuclear spin-spin interaction, in other words, via nuclear spin wave or electronic spin wave respectively. The Suhl-Nakamura interaction is a typical example of indirect interaction. At resonance frequency, most nuclei will resonate, and it is reasonable to say that, at this particular frequency, the relaxation is most effective and thus the relaxation time is the shortest. At frequency off resonance, only a small number of nuclei--by statistical reasoning and/or nuclei which are near the domain wall or actually inside the domain--can absorb energy. Thus, it will be more difficult to find the right neighbors to dissipate the absorbed energy. As a consequence, we would expect a longer relaxation time when the frequency is off resonance. However, this does not happen when the energy can be dissipated through spin-lattice relaxation for the case of higher temperature.

The line width and the relaxation time may be expected to follow the relationship

$$\Gamma \tau = 1 \tag{28}$$

In solids, relaxation is not the sole contributor to the line width but many other factors such as distribution of fields, presence of conduction electrons [47], and so on. Therefore, the apparent width, Γ_a, is quite different from the true width, Γ. However, we may expect that the overall effect should still follow

a relationship

$$\Gamma_a \tau = C \qquad (29)$$

where C is a constant. Therefore, the change in relaxation time as observed in Table VI is simply a consequence of the narrowing of the absorption line width in the presence of an external field discussed in a later section, 2.8.4.5.

The sinosoidal behavior in the presence of an external field may be understood as follows. The principal magnetization process at radio frequencies in multidomain ferromagnetic metal is known [43] to be the displacement of domain walls, and this suggests that the nuclei in the domain walls will contribute the most to the absorption line shape. Within the domain walls, because of the spin arrangement, a spectrum of dipole fields results and in turn gives rise to a spectrum of resonance frequency across the wall. Therefore the signal due to nuclei within domain walls, does not show distinct quadrupole splitting but is extremely broad. However, this inhomogeneity in fields does not apply to nuclei within the domain, and a single quadrupole splitting may be expected. The effect of the external field is to sweep the domain walls out of the sample and expose those nuclei inside to the radio frequencies. The sinosoidal behavior can then be observed.

The total quadrupole splitting is only 0.7 Mc/sec and

this is extremely small compared with the half width of 34 Mc/sec. Thus, this quadrupole splitting can never be observed with the steady state method.

2.8.4.4. EXTERNAL STATIC MAGNETIC FIELD DEPENDENCE OF THE RESONANCE FREQUENCY

The gyromagnetic ratio γ_N determined experimentally agrees well with the known value 2π x 1055$(Oe\text{-}sec)^{-1}$. However, the demagnetizing field determined from the intercept of the solid line at H = 0 in Fig.24 is only about $\sim$2kOe which is smaller than both $(4\pi/3)M_S$ and $4\pi M_S$. Note also that we have used only the last four points to determine the solid line. The other data points at lower applied field are all below the solid line. The reason is that we believe the resonance frequency for the nuclei in the domain wall is not exactly the same for the nuclei in the bulk of domains--justification in the following section--but is slightly lower [44]. Therefore, the observed frequencies at low fields are lower than what they should be.

2.8.4.5. EXTERNAL STATIC MAGNETIC FIELD DEPENDENCE OF THE SPIN ECHO LINE SHAPE

The decrease of line width in the presence of an external applied field is believed to be the result of removal of domain walls from the sample. Note that in Fig.25, the spectrum at H = 0, is slightly asymmetric and has a small hump on the right hand side.

This may suggest the presence of another small absorption peak owing to those nuclei in the bulk of domains suggested in the previous section. Another possibility is that this hump is due to the presence of localized Mn^{3+} nuclei. However, this proposal is disregarded, because if this is true, then the hump should persist even in the presence of an external field but his is not observed.

The reduction of amplitude when single crystals are used is due to the presence of skin depth effect which can be estimated by using the equation [45]

$$\delta = (2 \epsilon_o C^2 / \sigma \omega)^{\frac{1}{2}} \qquad (30)$$

where δ is the skin depth, σ is the conductivity and ω is the frequency. Using $\sigma \sim 10^2$ mho/cm, $\omega \sim 2\pi$ x 400 MHz, then δ has a value $\sim 2.6 \times 10^{-2}$ cm which is indeed smaller than the dimensions of the single crystal used.

2.8.4.6. RESONANCE FREQUENCY AND SPECTRUM

The peak positions of the resonance spectra correspond to the resonance frequencies for $Mn^{+3.5}$ [46] while the hump is interpreted as the contribution from the nuclei in the bulk of domains. The hyperfine fields for different X values shown in Table VII can be easily calculated using $\omega = \gamma_N(H_{hf} - H_D)$ where γ_N is assumed to have the value 2π x 1055(Oe-sec)$^{-1}$. The hyperfine

fields decrease as the X values increase. This is consistent with the observed magnetization behavior for various X values.

The hyperfine constant A is constant within experimental error for different X values as expected.

2.8.4.7. RELAXATION TIME OF 1st AND 2nd ECHOES

The relaxation times of the 1st and 2nd spin echoes may be expected to be different because the 1st echo is produced by the two rf pulses while the 2nd spin echo is produced by some other mechanism--here it is proposed to be due to the effect of quadrupole interaction. However, no quantitative theory is known to us for comparison.

III. $La_{1-X}Pb_XMn_{1-Y}Fe_YO_3$

3.1 SAMPLE PREPARATION

Three series of polycrystalline samples, X=0.44, $0.03 \leq Y \leq 0.17$; $0.14 \leq X \leq 0.65$, Y=0.1; and X=0.30, $0.30 \leq Y \leq 0.15$, were prepared by the conventional ceramic technique. Appropriate amounts of oxides (PbO, MnO_2, Mn_2O_3, La_2O_3 and $Fe_2^{57}O_3$) according to the chemical formula were well mixed by wet grinding in acetone. The mixtures of powders were pressed into pellets and fired at 800°C in a top-loaded furnace. The pellets were quenched in air, ground into a fine powder, repelletized and refired at 1000-1200°C; this sequence of operations was repeated until a single phase material was obtained, as determined by X-ray powder diffractometry.

Samples were also made by slow cooling in the furnace. However, the Mössbauer spectra (discussed in a later section) at room temperature showed small magnetic absorption peaks besides the central paramagnetic peaks shown in Fig.30a. These peaks can be removed by reheating the samples to a much lower temperature (900°C) and then quenching in air as shown in Fig.30b. The central paramagnetic peak is made up of two quadrupole split pairs; the inner pair is due to Fe ion in the Mn site and the outer pair Fe ion in the La or Pb site. (Justification of these identifications is given in the

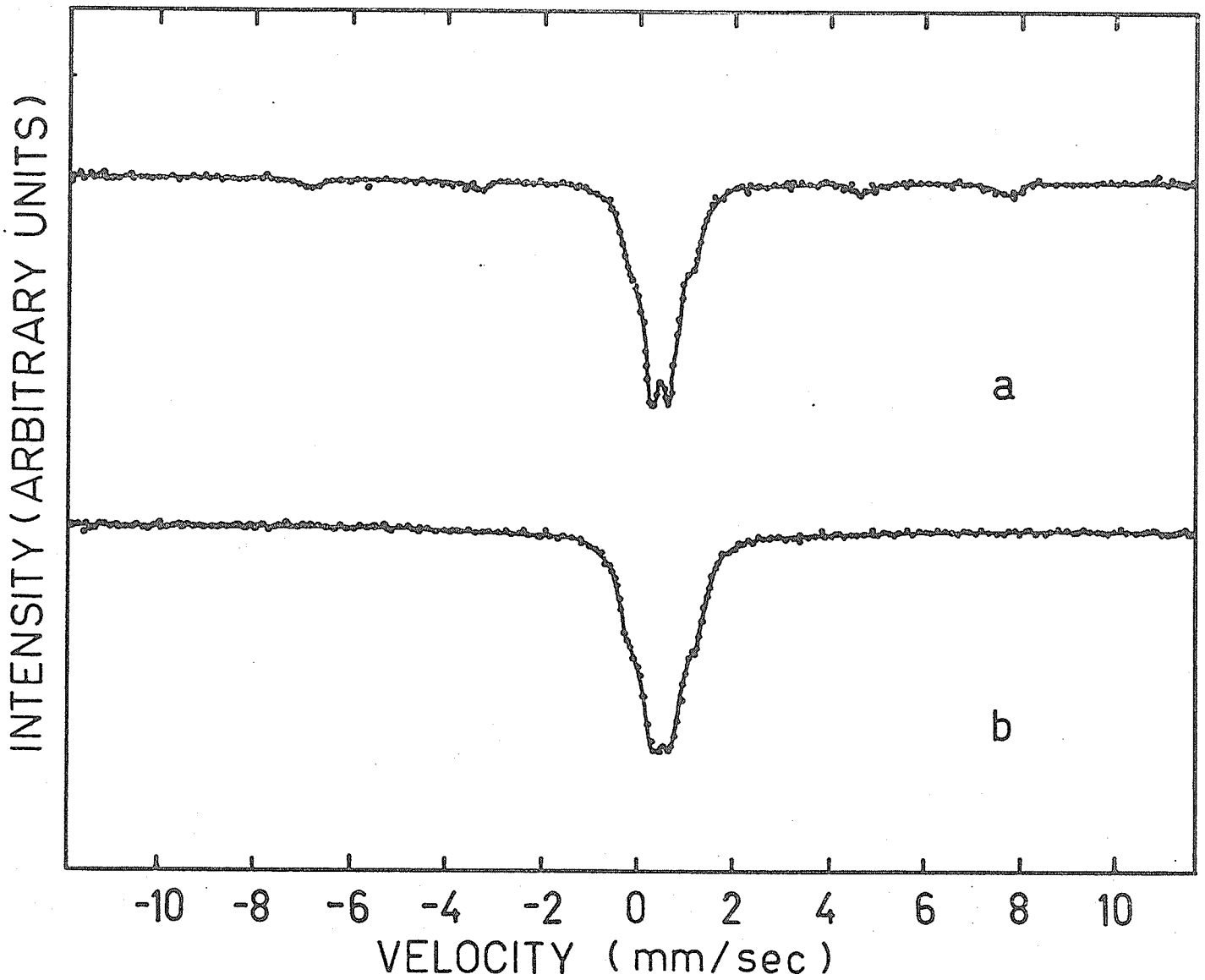

Fig. 30. Mössbauer spectra of $La_{0.7}Pb_{0.3}Mn_{0.9}Fe_{0.1}O_3$ of different thermal histories. (a) Furnace cooled at 1300°C. (b) Reheated to 900°C and quenched in water.

discussion section). A closer examination of the spectra in Fig.30 reveals that the outer pair of the paramagnetic peaks becomes more intense after the sample is quenched. This suggests that the Fe ions in the La or Pb sites, possibly due to their smaller ionic size (0.64Å for Fe^{3+}) compared to that of La or Pb (1.016Å for La^{3+} and 1.20Å for Pb^{2+}) and the unfavourable bonding angles with the other neighbouring ions, are quite loosely bound to their sites. As the sample is slowly cooled in the furnace, at a certain temperature, obviously even below 900°C, the Fe ions tend to bond together to form clusters which give rise to the observable magnetic splitting shown in Fig.30a. The samples analyzed in the following sections were quenched in air or water.

3.2 CRYSTAL STRUCTURE

The crystal structure was determined in the same way as that described in section 2.3. It is found that these polycrystals have the same structure as the single, undoped crystals. Table IX shows the complete powder diffraction data of $La_{0.74}Pb_{0.26}Mn_{0.9}Fe_{0.1}O_3$. However, besides the weak line [1,3,1], there are two more weaker lines [3,$\bar{3}$,1] and [3,3,$\bar{2}$]. These may be impurity lines but none of the d values from the starting materials matches them. We suspect that these correspond to superlattice lines due to a possibly non-random distribution of Fe ions in the lattice. The lattice constants for all three series are shown in Table X. They do not seem to follow any regular pattern as a function of X or Y and this is also observed in the undoped compounds.

Table IX. Powder Diffraction Data for $La_{0.74}Pb_{0.26}Mn_{0.9}Fe_{0.1}O_3$

Intensity	d_{obs}	d_{calc}	hkl
60	3.902	3.902	200
100	2.772	2.772	$2\bar{2}0$
100	2.745	2.747	220
10	2.354	2.362	$1\bar{3}1$
40	2.258	2.260	$22\bar{2}$
30	2.232	2.232	222
80	1.949	1.951	040
1	1.795	1.798	$3\bar{3}1$
30	1.750	1.751	$04\bar{2}$
30	1.736	1.739	240
5	1.663	1.666	$3\bar{3}\bar{2}$
70	1.595	1.600 1.595	$24\bar{2}$ 242
50	1.580	1.581	242
50	1.385	1.386	$04\bar{4}$
50	1.373	1.373	440
30	1.306	1.306	$24\bar{4}$
30	1.300	1.301	060
10	1.292	1.290	442
40	1.237	1.237	$06\bar{2}$
40	1.230	1.230	260
10	1.182	1.181	$\bar{6}22$
20	1.178	1.177	$62\bar{2}$
10	1.169	1.170	622
20	1.130	1.130	$44\bar{4}$
20	1.116	1.116	444
20	1.087	1.087	$\bar{6}40$
10	1.078	1.078	640

Table X. The Lattice Constant of $La_{1-x}Pb_xMn_{1-y}Fe_yO_3$

x	y	a_{Rh} (Å)	α_{Rh}
0.44	0.03	7.761±0.001	90°45'±3'
0.44	0.05	7.763±0.001	90°28'±3'
0.44	0.10	7.773±0.001	90°17'±3'
0.44	0.14	7.789±0.005	90°33'±5'
0.44	0.17	7.794±0.004	90°45'±5'
0.14	0.10	7.777±0.020	90°30'±5'
0.20	0.10	7.793±0.008	90°41'±3'
0.26	0.10	7.798±0.002	90°30'±3'
0.44	0.10	7.773±0.001	90°17'±3'
0.55	0.10	7.775±0.005	90°48'±4'
0.65	0.10	7.773±0.003	90°46'±3'
0.30	0.03	7.821±0.001	90°35'±3'
0.30	0.10	7.797±0.001	90°34'±3'
0.30	0.15	7.797±0.001	90°27'±3'

3.3 MÖSSBAUER STUDIES

3.3.1. INTRODUCTION

Mössbauer spectroscopy is a well-known technique for magnetic studies in recent years and its theory as well as its method of application has been discussed in great detail in many excellent texts and review papers[40], so here we will try to be extremely brief. Its basic principle is as follows. The particular radioactive nuclei[49] (Co^{57} and Sn^{119m} in this laboratory) are diffused into suitable matrices (Cr and $BaSnO_3$ respectively) so that when they decay by emitting a photon, the recoil momentum is shared by the entire lattice instead of the nucleus alone and the recoil energy is effectively zero. Thus the energy corresponding to the emitted photon is well defined and corresponds to the energy between the excited state and the ground state and can be reabsorbed by the nuclei in the ground state. The decay scheme for Co^{57} is shown in Fig.31. These Mössbauer nuclei are mostly used as probes to examine the electronic charge density, electric field gradient and the magnetic field in solid state physics. In general, a nucleus affected by its surroundings can be described by the following Hamiltonian

$$\mathcal{H} = -\vec{\mu}_N \cdot \vec{H} + \vec{Q} \cdot \nabla \vec{E} + \frac{2\pi}{5} Ze^2 |\psi(0)|^2 R^2 \qquad (1)$$

The first term is due to the nuclear magnetic dipole moment, $\vec{\mu}_N$, which interacts with the magnetic field, $\vec{H}$, due to its own electrons.

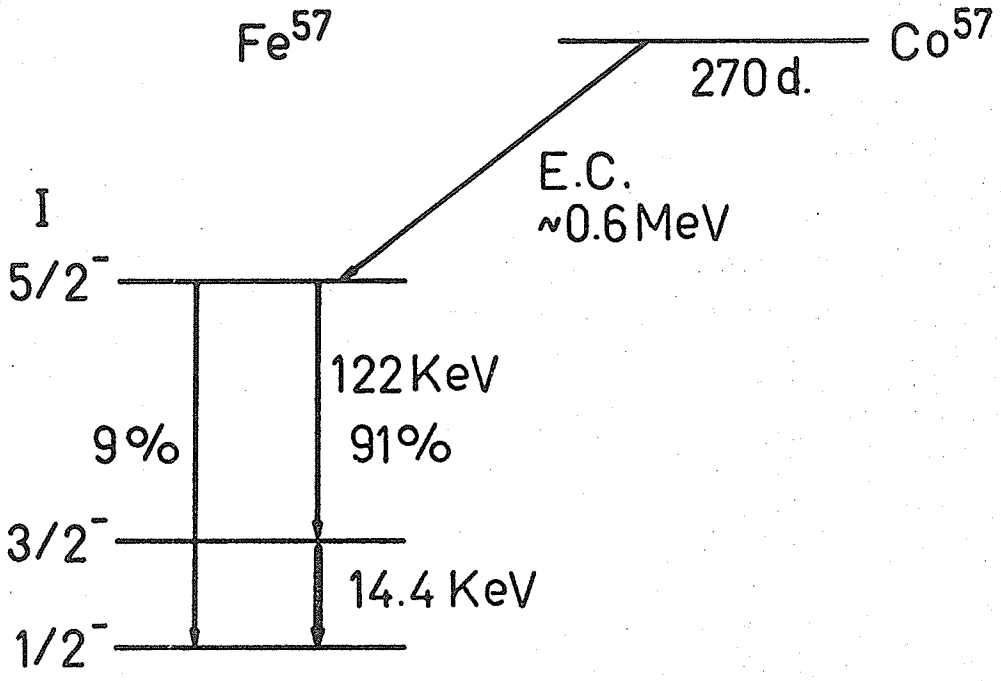

Fig. 31. Decay scheme of Co^{57}.

There are, in general, four contributions to $\vec{H}$. (i) Fermi contact interaction: this interaction arises whenever the atom has a partially filled magnetic shell, e.g. 3d-shell. This net spin moment has a different effect on the core up-spin and down-spin and in turn creates a net spin density at the nucleus. The strength of the magnetic field for unit spin is 210-250 kOe for ferric ions. Lower values are characteristic of oxides and higher values of fluorides. (ii) Dipolar field: this comes from the interaction of the electron spins of lthe surrounding atoms as well as the nucleus' own electrons with the nuclear magnetic moment. If the surroundings have perfect cubic symmetry and the spin-orbit coupling is absent, this contribution vanishes. Usually,

its contribution varies from 1 to 10 kOe. (iii) Orbital contribution: this arises whenever the orbital quantum number is different from zero. For metallic iron this term is estimated to be $\sim$ 70 kOe. (iv) Internal field: this results directly from the application of an external field $\vec{H}_o$, taking into account the Lorentz and demagnetizing fields. All these contributions can be represented by the following expression

$$\mathcal{H}_1 = 2\mu_B \vec{\mu}_N \cdot \left(\frac{8\pi}{3} \delta(r) \hat{S} + \frac{\hat{L}}{r^3} + \frac{3(\vec{r}\hat{S})\vec{r} - r^2\hat{S}}{r^5} \right) + \vec{\mu}_N \cdot \left(\vec{H}_o + \frac{4\pi}{3}\vec{M} - D\vec{M} \right) \qquad (2)$$

where $\hat{S}$ and $\hat{L}$ are operators for the spin and orbital momenta of the electron, and $\vec{H}_o$ and $\vec{M}$ the applied external field and the magnetization.

However, for some oxides and fluorides, there is also the contribution from the so called "Supertransferred hyperfine field" [50] which is a result of the transfer of spin and charge density from a cation to an adjacent anion by overlapping and covalency. As a consequence, the core polarization is modified and so is the spin density at the nucleus.

For the 14.4 keV transition in Fe^{57} which is the isotope used in subsequent experiments, due to the existence of magnetic hyperfine interaction below the ordering temperature, the excited level splits into four levels and the ground level into two. For L=1, in order to satisfy the conditions of conservation of momentum and parity, there are only six allowed transitions, $\Delta m = 0, \pm 1$, as shown in Fig. 32a.

The second term of the equation (1) comes from the interaction

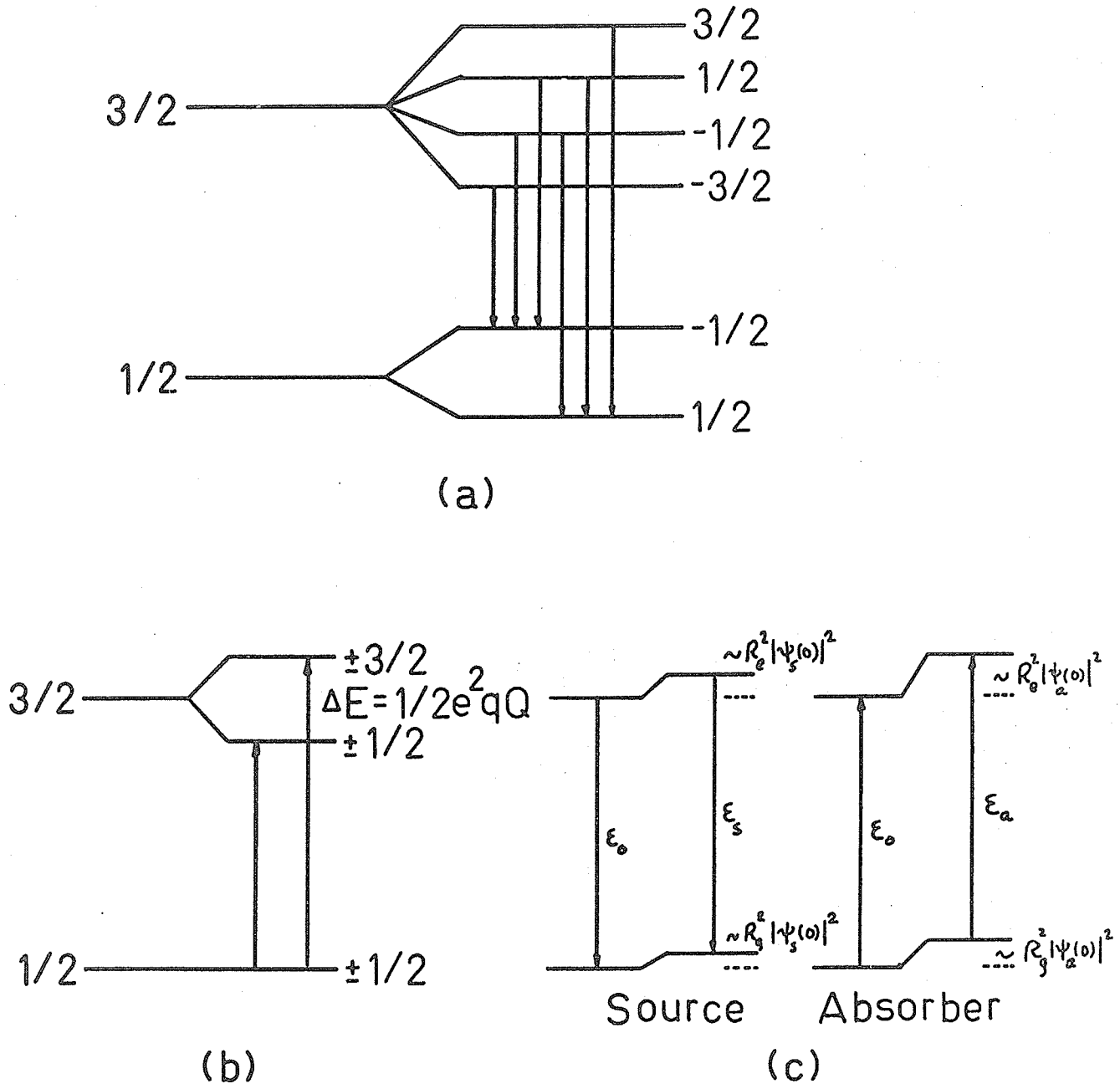

Fig. 32. Energy level diagram of Fe^{57}. (a) Magnetic Zeeman splitting of the two lowest states in a magnetic field. (b) Electric quadrupole splitting in an inhomogeneous electric field. (c) Isomer shift.

of the nuclear electric quadrupole moment, $\vec{Q}$, with the electric field gradient due to the surrounding charges. Its effect on the nuclear levels is to lift all or part of their (2I+1)-fold degeneracy where I is the nuclear spin quantum number as shown in Fig.32b.

The nucleus has a finite radius of electric charge which will in general be different for each nuclear state of excitation or energy level. This gives rise to the third term and in turn the observable so called "Isomer Shift" or "Chemical Shift" which can be represented by the expression

$$I.S. = \frac{2\pi}{5} Ze^2 \left[|\Psi_a(0)|^2 - |\Psi_s(0)|^2 \right] \left[R_{ex}^2 - R_{gd}^2 \right] \qquad (3)$$

where $e|\Psi_a(0)|^2$, $e|\Psi_s(0)|^2$ are the electronic charge densities of the absorber and source, and R_{ex}, R_{gd} the nuclear radii of the excited and ground state. It is shown graphically in Fig.32c. The electronic charge density at the nucleus is very sensitive to the valence state[51] of the atom because of the screening effect on e.g. the 3s-electron by the 3d-electrons of Fe ions. This effect enables us to tell with some certainty about the valence state of a certain Mössbauer ion in a compound.

Unfortunately, the quantities thus determined are all products of two unknowns: $\vec{\mu} \cdot \vec{H}$, $\vec{Q} \cdot \nabla \vec{E}$, and $e|\Psi|^2 \cdot Ze R^2$. Except the first one which can be resolved within the scope of Mössbauer spectroscopy by using an external magnetic field, the others have to rely on other experi-

mental techniques for their absolute determinations.

3.3.2 EXPERIMENTAL APPARATUS, DATA ANALYSIS AND CALIBRATION

The Mössbauer spectrometer basically consists of a drive on which the radioactive source is mounted, an absorber containing the appropriate nuclei to absorb the monochromatic radiation and a counter to register the radiation passing through the absorber. A full description of the electronics of the spectrometer as well as the temperature control setup has been given elsewhere[52] and will not be repeated here. However, one additional remark has to be made concerning the exact temperature of the low temperature spectra. All spectra at temperatures near helium were obtained using the superconducting magnet. The sample holder contacts the helium reservoir via a Be-Cu spring as shown in Fig.33 but there is no temperature sensor at the sample. However, by measuring the hyperfine field at the unknown temperature in a sample that has an ordering temperature near helium temperature, and comparing it with published values, we can easily estimate the unknown temperature to within $\pm 0.5^{\circ}$. In our case, one of the materials studied in later sections has this property; $ZnFe_2O_4$ with $T_N \approx 10^{\circ}K$ [53]. The temperature is estimated to be $7.0 \pm 0.5^{\circ}K$.

The spectra at various temperatures were least-squares fitted by a computer program developed by Powell [54] assuming all the line shapes to be Lorentzian. Basically, in order to find the best least-squares fit to a set of data (x_j, y_j), the quantity

$$D = \sum_{j=1}^{N} \left[y_i(\text{obs.}) - y_i(\text{theo.}) \right]^2 \qquad (4)$$

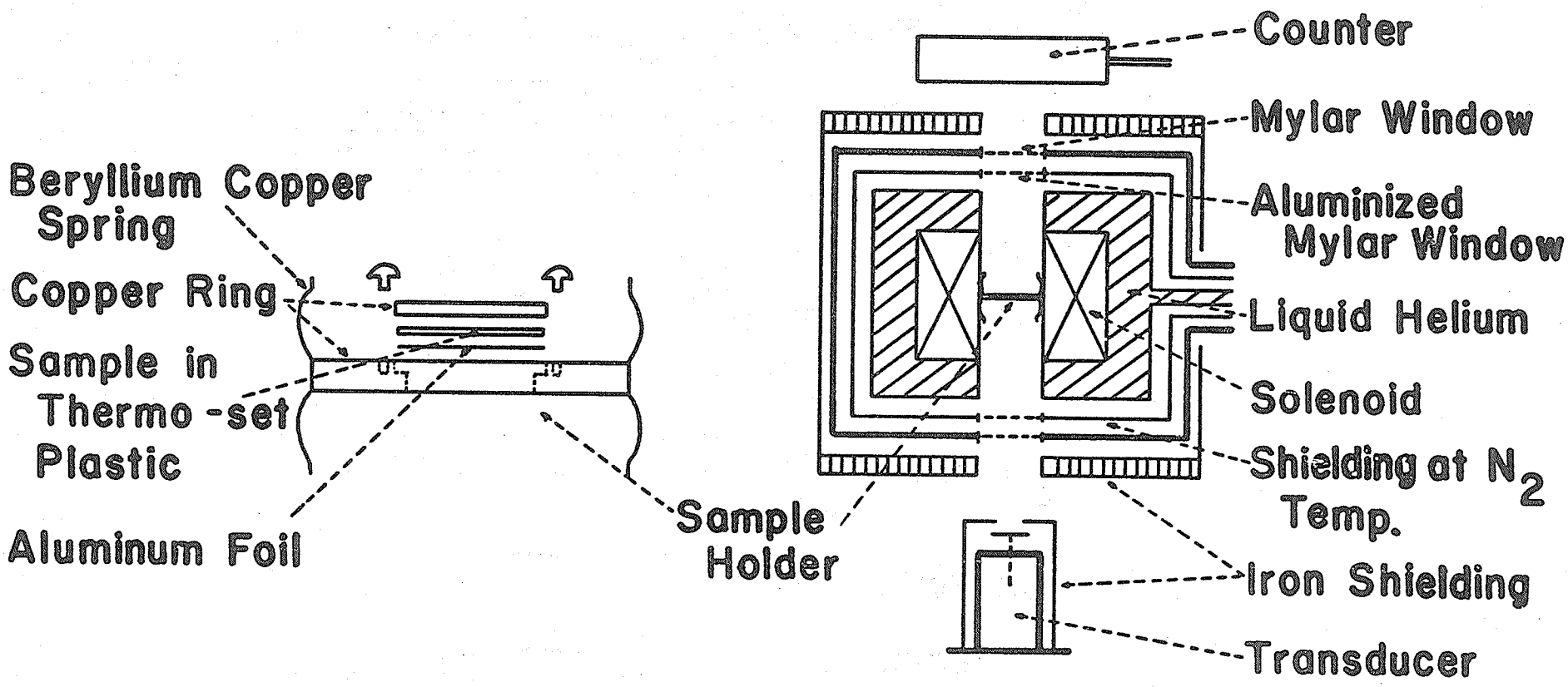

Fig. 33. Low temperature setup in the superconducting magnet.

must be minimized where $Y_j(\text{theo.}) = \sum_{i=1}^{n} \frac{A_i}{1+4[(X_j - P_i)/B_i]^2}$. Here A_i, P_i, B_i are the amplitude, position and half-width of the ith peak. The goodness-of-fit is defined by the parameter

$$F = \sum_{j=1}^{N_p} \frac{[Y_j(\text{obs.}) - Y_j(\text{theo})]^2}{Y_j(\text{obs.})} \qquad (5)$$

where N_p is the number of points in the spectrum. A spectrum is considered fitted satisfactory if $F \sim 1.5N_p$. In case the spectrum is magnetically split , the hyperfine field, isomer shift and quadrupole splitting are calculated from all six lines by redefining the position parameters P(i) in the computer program as

$$\begin{aligned}
P(6) &= GH(1+3R) + E.Q. + I.S. \\
P(5) &= GH(1+R) - E.Q. + I.S. \\
P(4) &= GH(1-R) - E.Q. + I.S. \\
P(3) &= GH(-1+R) - E.Q. + I.S. \\
P(2) &= GH(-1-R) - E.Q. + I.S. \\
P(1) &= GH(-1-3R) + E.Q. + I.S.
\end{aligned} \qquad (6)$$

where $G = g_o \mu_n / 2K$ and $R = g_e/g_o$. Here g_o, g_e, μ_n and K are the gyromagnetic ratio of the ground state and of the excited state, the nuclear magneton and the normalizing constant such that the separation of line No.1 and No.6 of an Fe spectrum equals 330 kOe.

An iron foil was used to calibrate the velocity scale of the

spectrometer. 10.656 mm/sec corresponding to 330 kOe was used as the separation between the outermost peaks and 0.16 mm/sec was used to correct the isomer shift value so that the reported value is with respect to metallic iron.

3.3.3. HYPERFINE FIELD DATA

Spectra at 297°K were obtained for all samples in all three series. At other temperatures, only a few selected samples from each series were used. 500 channels were used for all spectra and they were all collected in constant acceleration, the so called "Time Mode".

3.3.3.1 SPECTRA AT 297°K

All spectra at this temperature resemble the one shown in Fig.34. They were fitted with four lines with width constraints $\Gamma_1 = \Gamma_4$ and $\Gamma_2 = \Gamma_3$. The data are tabulated in Table XI and are plotted in Fig.35 and Fig.36.

3.3.3.2 SPECTRA AT 7°K

The spectra at this temperature are well resolved and the absorption lines show some structures depending on the values of X as shown in Fig.37 for the series with X=0.3 and $0.03 \leq Y \leq 0.15$ [96]. Because of the line structure, different kinds of constraints were used to fit the same set of spectra. In Fig.37, four six-line patterns were used with width constraints, $\Gamma_{i,j} = \Gamma_{i,7-j} = \Gamma_{k,j}$ where i and k stand for pattern numbers (1 to 4) and j denotes the line positions

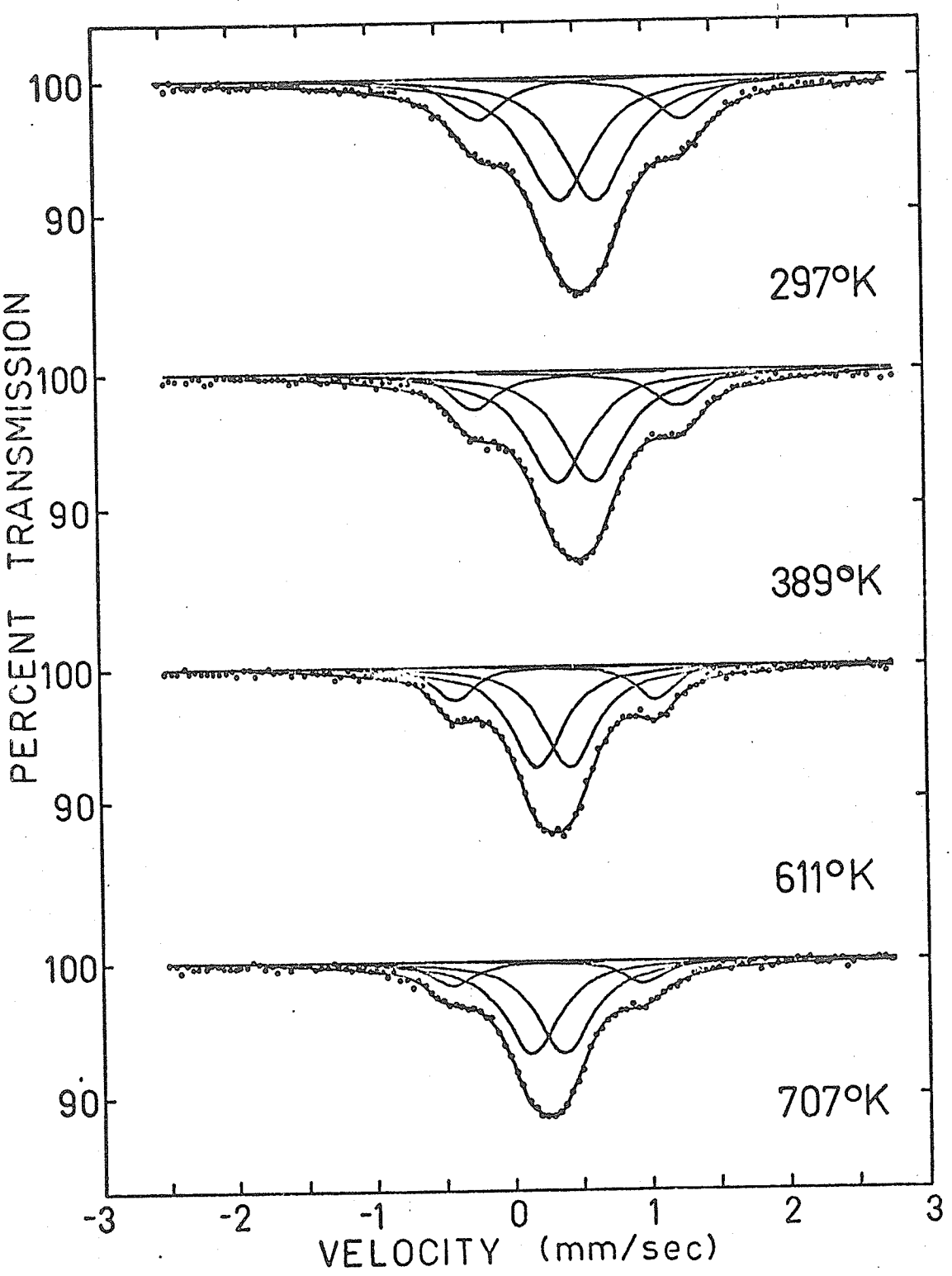

Fig. 34. Mössbauer spectra of $La_{0.70}Pb_{0.30}Mn_{0.97}Fe_{0.03}O_3$ at different temperatures.

Table XI. Mössbauer Data for $La_{1-x}Pb_xMn_{1-y}Fe_yO_3$ at T = 297°K

Pb	Fe	$\frac{1}{2}e^2qQ_{1,4}$ * (mm/sec)	$\frac{1}{2}e^2qQ_{2,3}$ ** (mm/sec)	I.S.$_{1,4}$ *** (mm/sec)	I.S.$_{2,3}$ *** (mm/sec)	$\Gamma_{1,4}$ (mm/sec)	$\Gamma_{2,3}$ (mm/sec)
0.44	0.03	1.47	0.240	0.55	0.54	0.40	0.47
0.44	0.05		0.338		0.52		0.54
0.44	0.10		0.344		0.52		0.54
0.44	0.14	1.22	0.348	0.54	0.52	0.43	0.61
0.44	0.17	1.21	0.336	0.54	0.53	0.44	0.59
0.14	0.10		0.284		0.54		0.49
0.20	0.10	1.37	0.292	0.53	0.53	0.24	0.56
0.26	0.10	1.32	0.299	0.52	0.53	0.35	0.55
0.44	0.10		0.344		0.52		0.54
0.55	0.10	1.34	0.366	0.54	0.54	0.37	0.60
0.65	0.10	1.35	0.378	0.55	0.54	0.40	0.60
0.30	0.03	1.55	0.236	0.54	0.54	0.31	0.40
0.30	0.10	1.33	0.379	0.53	0.53	0.33	0.45
0.30	0.15	1.21	0.337	0.52	0.52	0.37	0.45

*Error: ± 0.01 mm/sec

**Error: ± 0.005 mm/sec

*** Relative to iron metal; error: ± 0.01

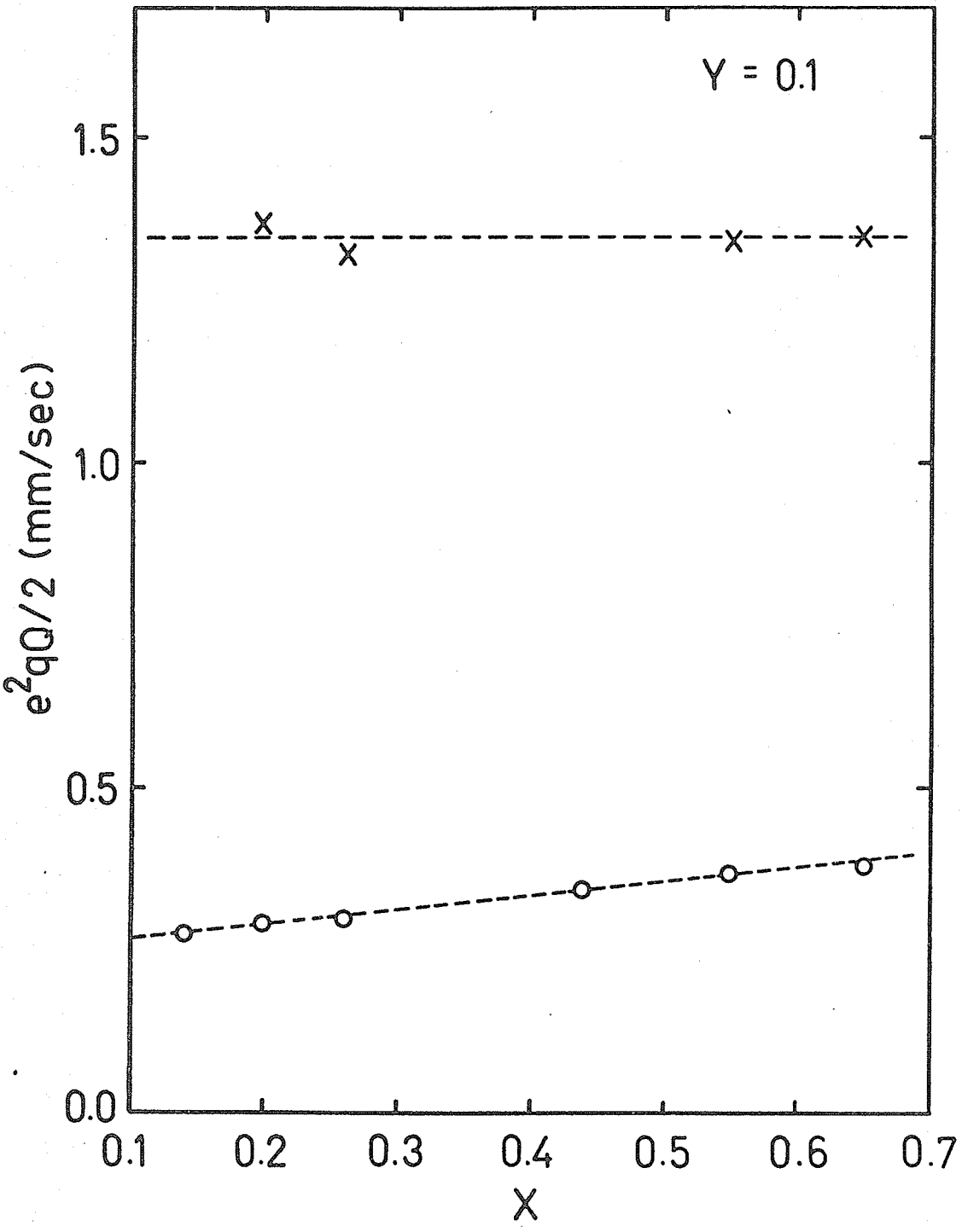

Fig. 35. Quadrupole splitting of $La_{1-X}Pb_XMn_{0.9}Fe_{0.1}O_3$. The symbol X corresponds to the value of the outer pair and o the inner pair.

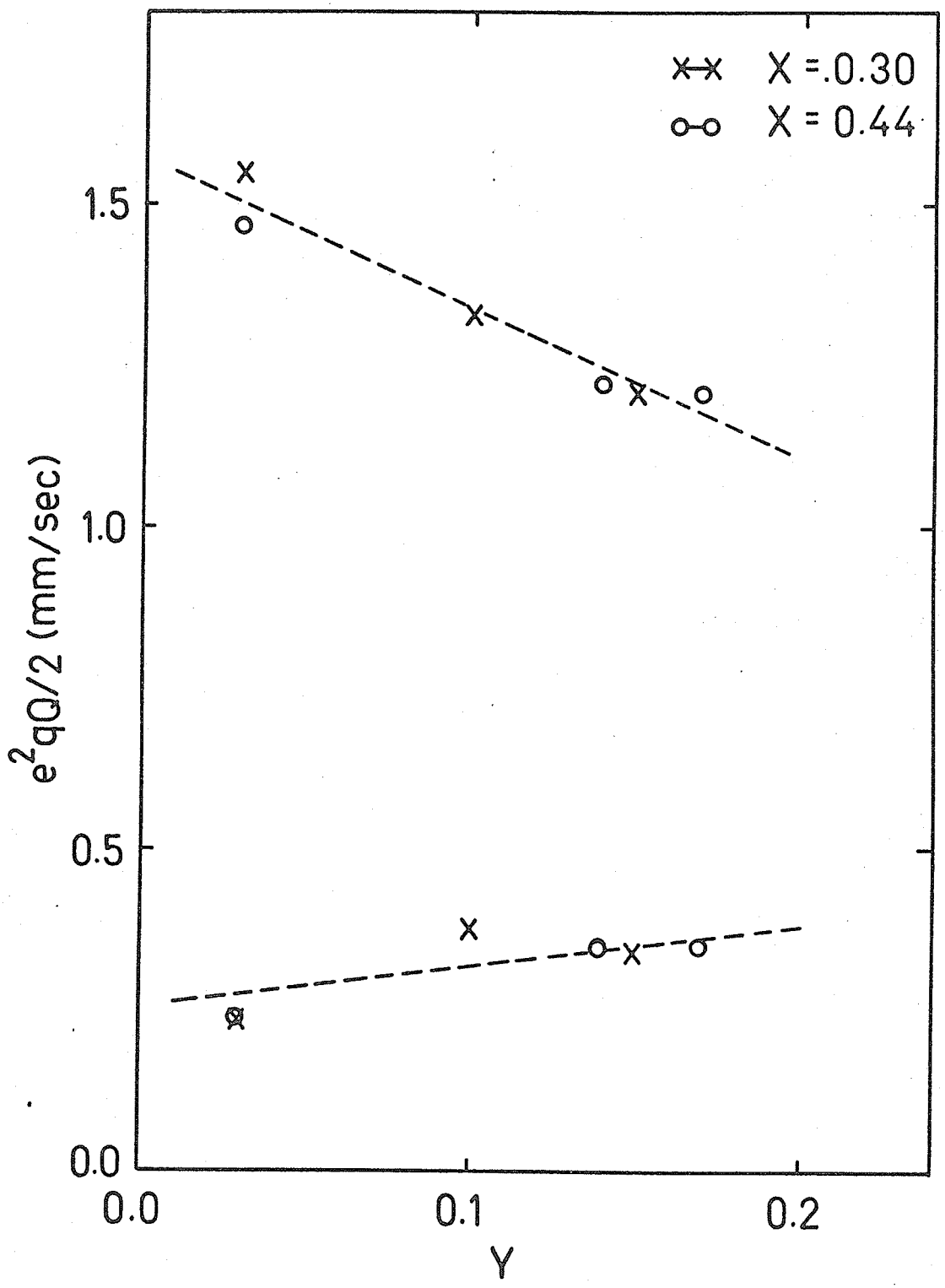

Fig. 36. Quadrupole splittings of $La_{1-X}Pb_XMn_{1-Y}Fe_YO_3$ as a function of iron substitution.

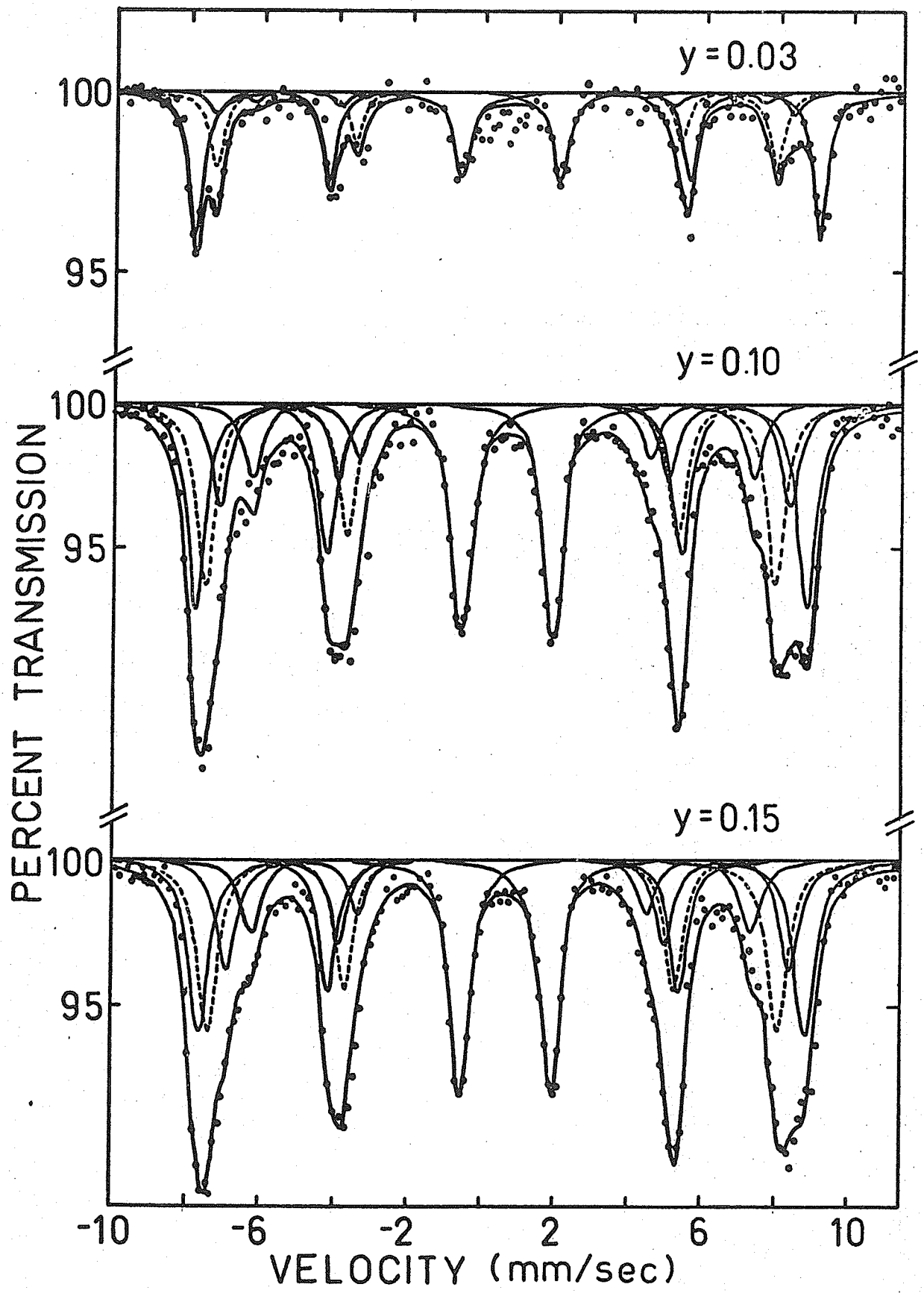

Fig. 37. Mössbauer spectra of $La_{0.7}Pb_{0.3}Mn_{1-y}Fe_yO_3$ at 7° K. The full curves correspond to computer fit with width constraints. The dashed curve corresponds to the contribution from Fe^{3+} ions at the La/Pb sites.

(1 to 6). The parameters for the final fitting is given in Table XII. Fig.38 shows the same set of spectra fitted with slightly different sets of constraints, that is, besides the constraints used before, the intensities among the patterns were restricted according to the probability formula

$$P(n,X) = \binom{6}{n} X^n (1-X)^{6-n} \qquad (7)$$

where n is the number of Mn sites occupied by Fe^{3+}, and X the amount of iron substitution. The final fitting parameters is given in Table XIII In order to obtain more informations about the substituted Fe spin, spectra with 50 kOe external field were also obtained as shown in Fig.39. The final fitting parameters are also listed in Table XII. Fig.40 shows a set of spectra for $La_{0.8}Pb_{0.2}Mn_{0.9}Fe_{0.1}O_3$ at different strengths of applied magnetic field.

3.3.3.3 SPECTRA AT VARIOUS TEMPERATURES

Fig.41 shows a representative set of spectra between nitrogen temperature and room temperature. Because of the line broadening and comparatively poorer resolution at these temperatures, only the average effective fields were determined and plotted in Fig.42.

3.4 MAGNETIZATION AND CURIE TEMPERATURE DETERMINATIONS

The magnetization of a few selected samples was determined in the same manner as that described in section 2.4.1 and the results are shown in Figs.43 and 44. The Curie temperatures of the samples

Table XII. Mössbauer Data for $La_{0.7}Pb_{0.3}Mn_{1-Y}Fe_YO_3$ at 7° K with no Intensity Constraints.

Y	H^*_{app}	H^*_0	H	H_1	H_2	I^{**}_0	I	I_1	I_2	$\Gamma^{**}_{1,6}$	$I.S.^{**}_0$	I.S.	$I.S._1$	$I.S._2$	$\frac{1}{4}e^2qQ^{**}_0$	$\frac{1}{4}e^2qQ$	$\frac{1}{4}e^2qQ_1$	$\frac{1}{4}e^2qQ$
0.03	0	528	474	488	430	0.039	0.023	0.002	0.003	0.49	0.66	0.64	0.58	0.75	-0.01	-0.29	-0.02	-0.00
0.10	0	517	482	481	423	0.074	0.072	0.028	0.024	0.61	0.61	0.59	0.64	0.64	-0.04	-0.29	0.03	-0.02
0.15	0	511	481	475	422	0.063	0.075	0.041	0.025	0.67	0.64	0.61	0.69	0.64	-0.02	-0.23	0.09	-0.02
0.03	50	567	511	480	427	0.055	0.021	0.004	0.005	0.46	0.67	0.60	0.62	0.69		-0.22		
0.10	50	555	513	454	401	0.087	0.059	0.024	0.023	0.79	0.54	0.56	0.53	0.61		-0.19		
0.15	50	553	510	452	398	0.073	0.046	0.042	0.023	0.83	0.58	0.59	0.64	0.59		-0.14		

* In units of kOe

**In units of mm/sec

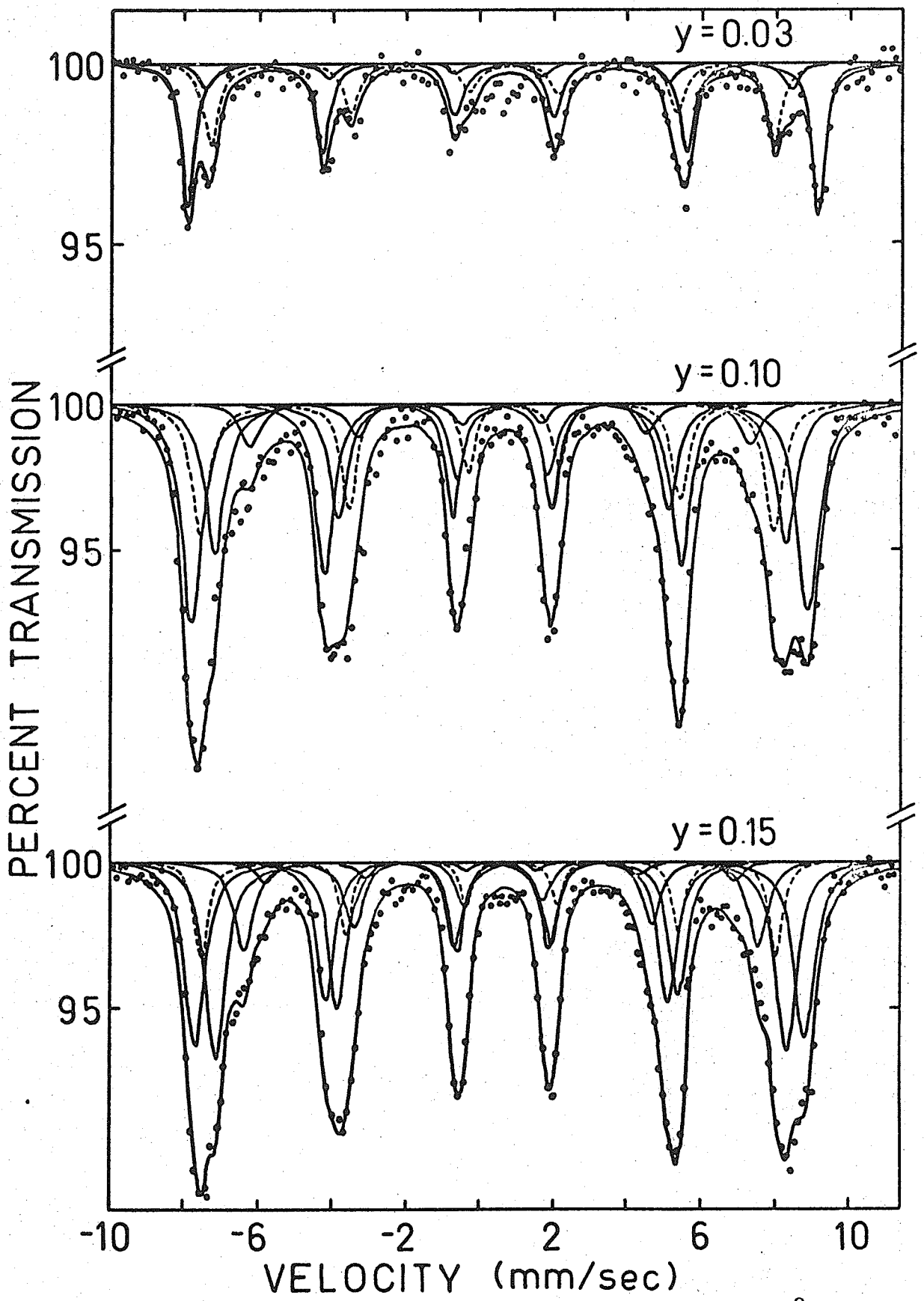

Fig. 38. Mössbauer spectra of $La_{0.7}Pb_{0.3}Mn_{1-Y}Fe_YO_3$ at 7° K. The full curves correspond to computer fit with width and intensity constraints. The dashed curve corresponds to the contribution from Fe^{3+} ions at the La/Pb sites.

Table XIII. Mössbauer Data for $La_{0.7}Pb_{0.3}Mn_{1-Y}Fe_YO_3$ at 7° K with Intensity Constraints.

y	H_0(kOe)	H_1(kOe)	H_2(kOe)	H_3(kOe)	H(kOe)
0.03	528	491	458		472
0.10	515	478	419	389	480
0.15	512	480	433	395	483

y	$I.S._0$ (mm/sec)	$I.S._1$ (mm/sec)	$I.S._2$ (mm/sec)	$I.S._3$ (mm/sec)	I.S. (mm/sec)
0.03	0.66	0.53	0.90		0.66
0.10	0.60	0.61	0.59	0.49	0.58
0.15	0.63	0.65	0.64	0.60	0.61

y	$\frac{1}{4}e^2qQ$(1to4) (mm/sec)	$\frac{1}{4}e^2qQ$ (mm/sec)	$\Gamma_{1,6}$(1to4) (mm/sec)	$\Gamma_{1,6}$ (mm/sec)
0.03	-0.018	-0.294	0.44	0.52
0.10	-0.033	-0.363	0.66	0.57
0.15	-0.024	-0.312	0.65	0.45

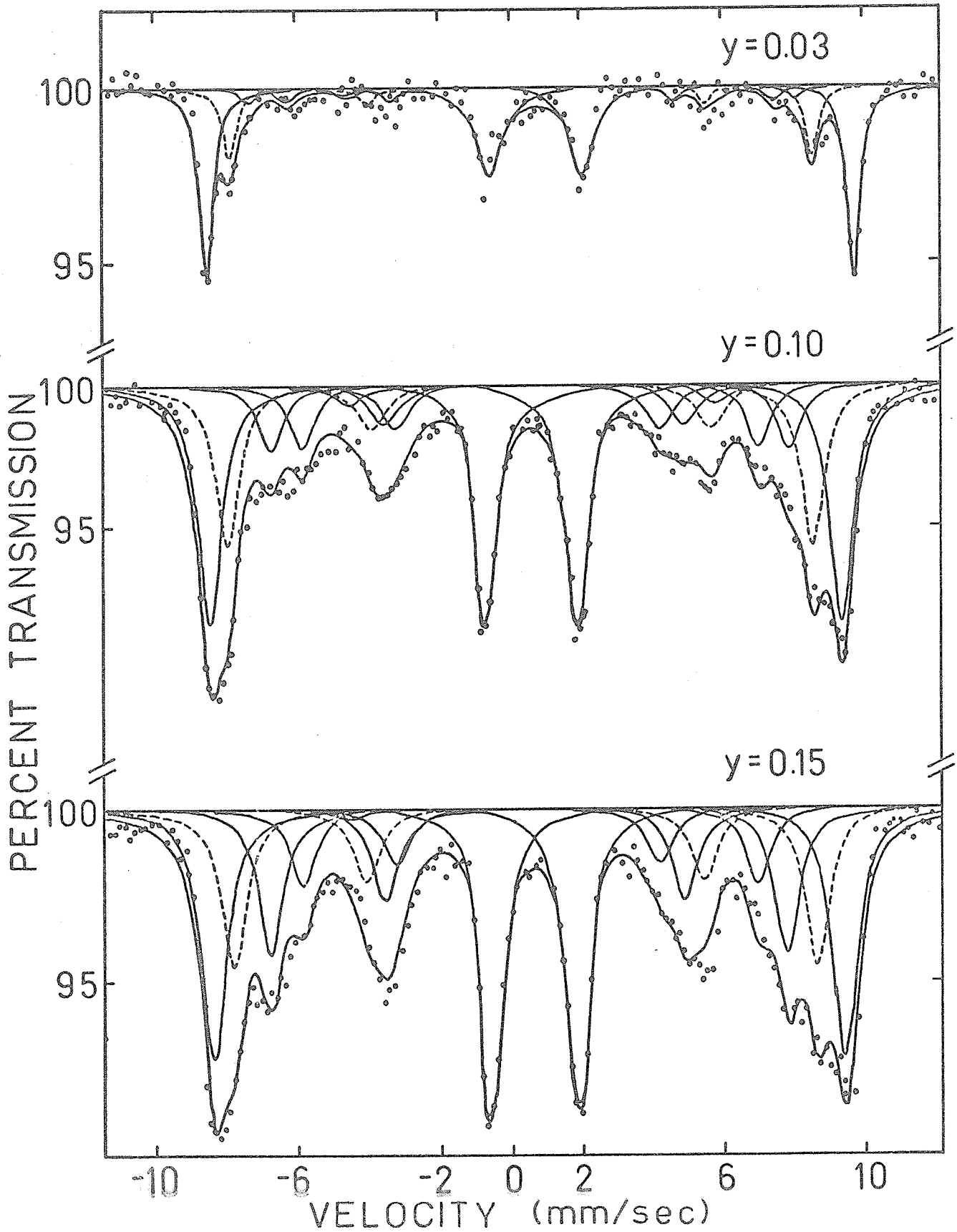

Fig. 39. Mössbauer spectra of $La_{0.7}Pb_{0.3}Mn_{1-y}Fe_yO_3$ in a 50 kOe field. The full curves correspond to computer fit with width constraints. The dashed curve corresponds to the contribution from Fe^{3+} ions at the La/Pb sites.

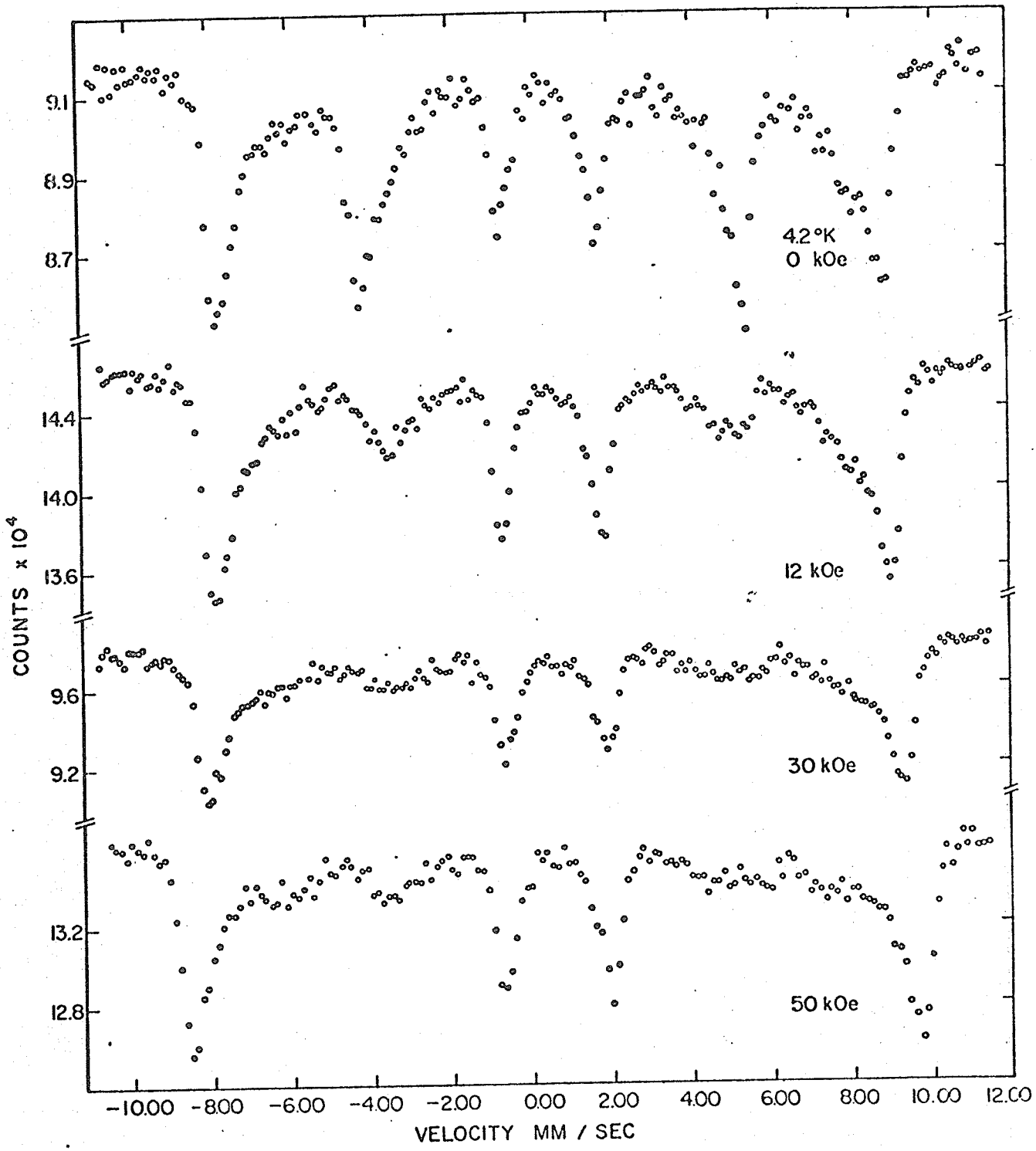

Fig. 40. Mössbauer spectra of $La_{0.8}Pb_{0.2}Mn_{0.9}Fe_{0.1}O_3$ at 7° K in various fields.

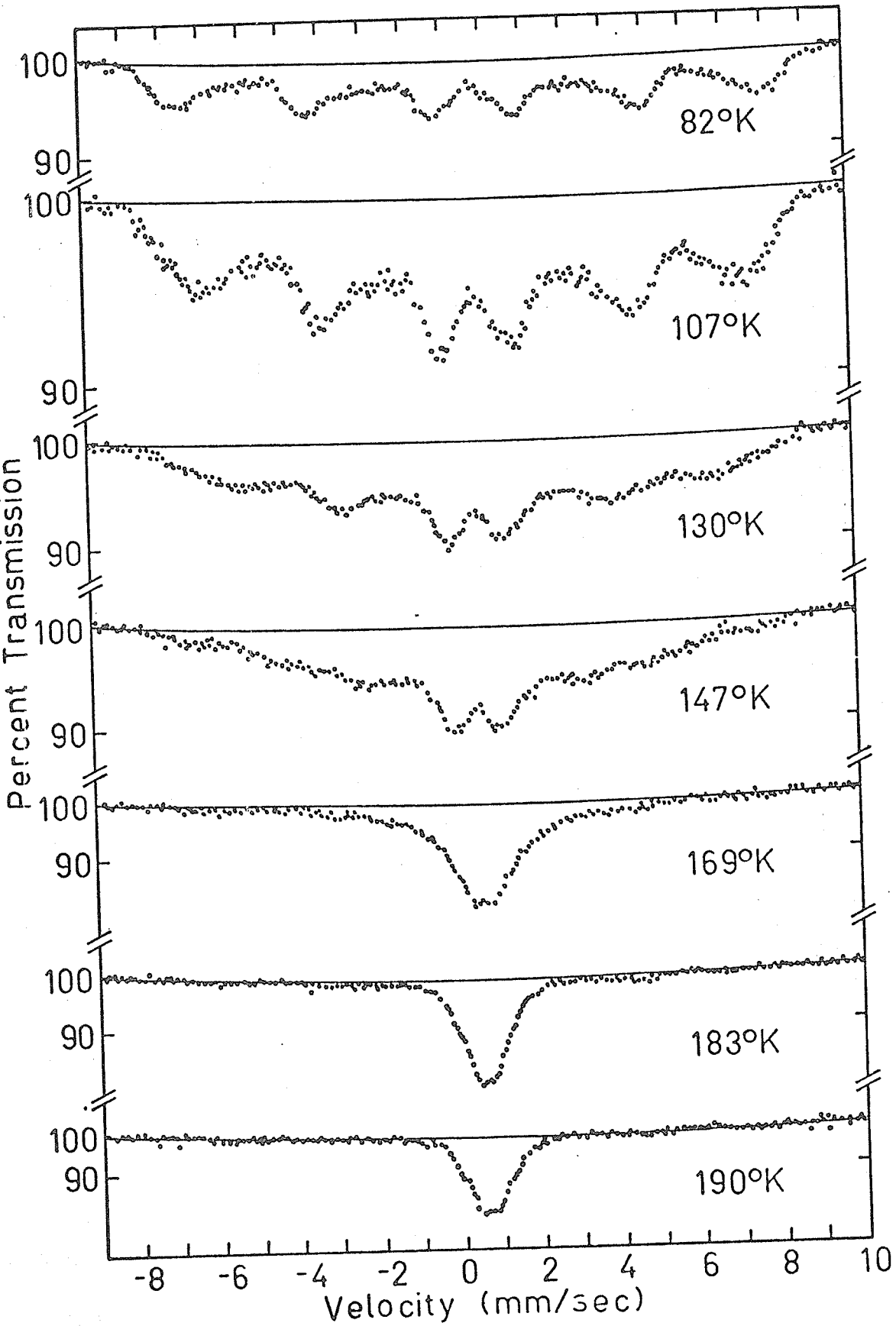

Fig. 41. Mössbauer spectra of $La_{0.70}Pb_{0.30}Mn_{0.85}Fe_{0.15}O_3$ at different temperatures.

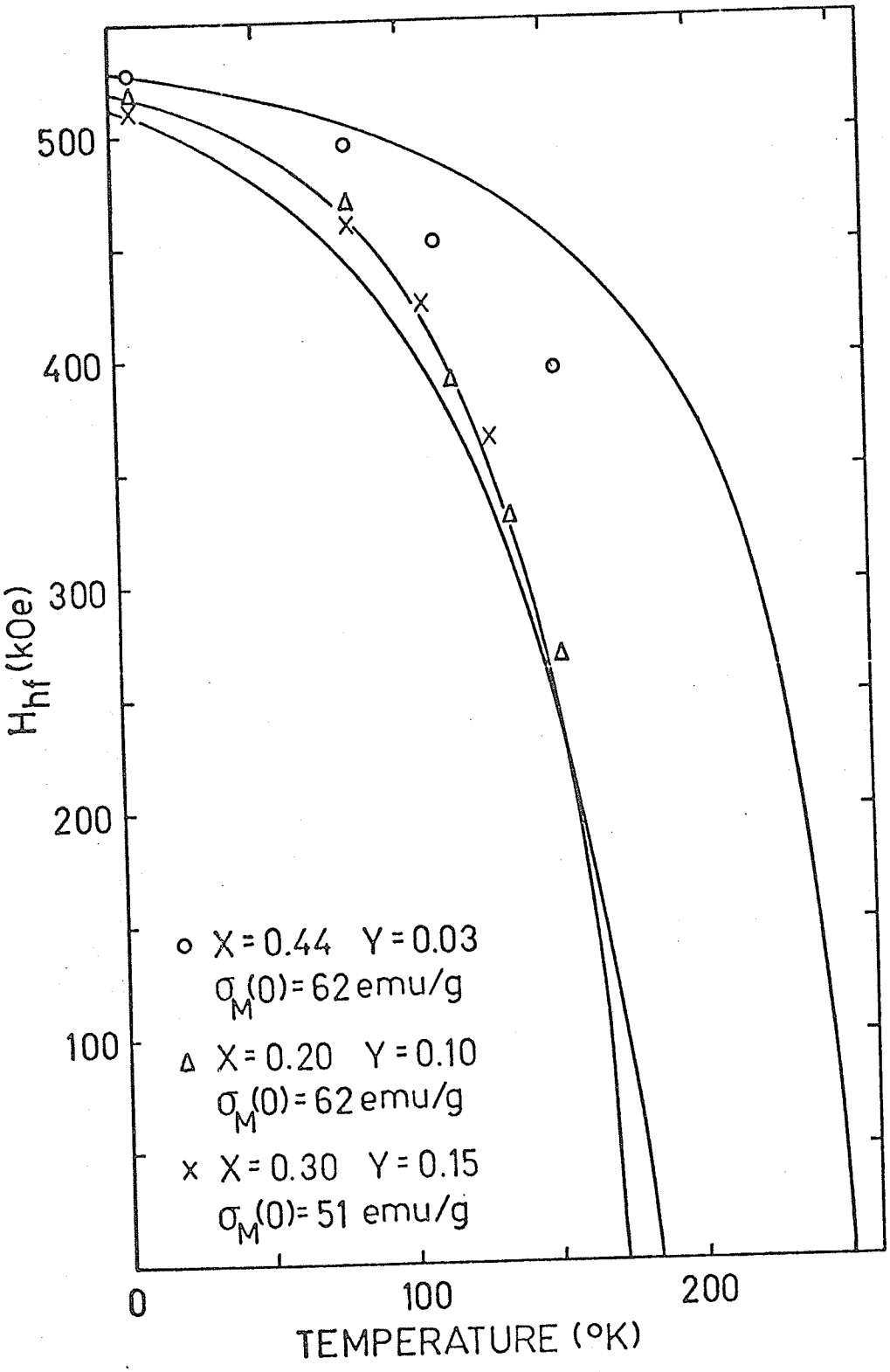

Fig. 42. The hyperfine field of $La_{1-X}Pb_XMn_{1-Y}Fe_YO_3$ as a function of temperature. The full curves are the corresponding magnetization curves normalized to the hyperfine fields.

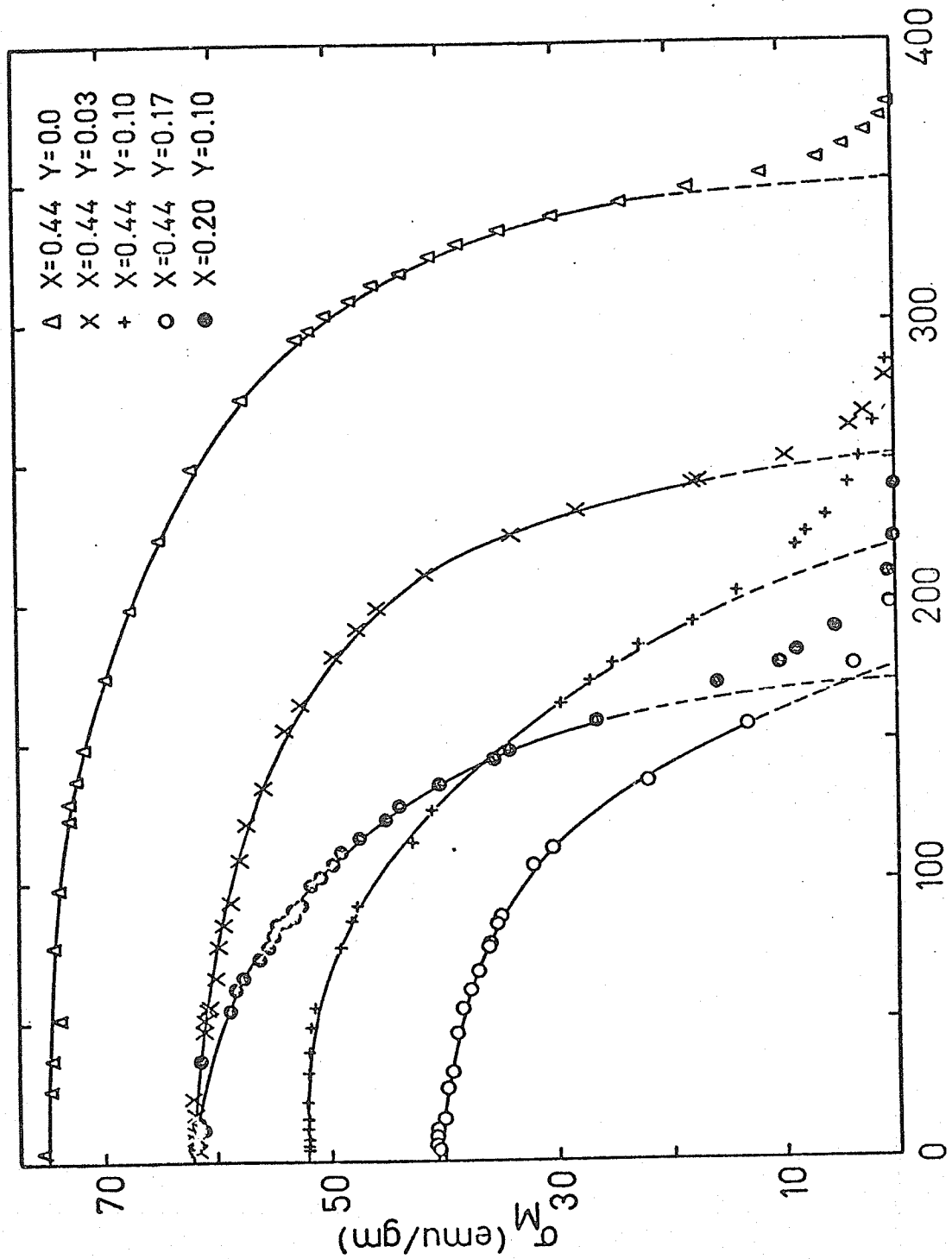

Fig. 43. Saturation magnetization of $La_{1-X}Pb_XMn_{1-Y}Fe_YO_3$ as a function of temperature. The full curves emphasize the trend of the data.

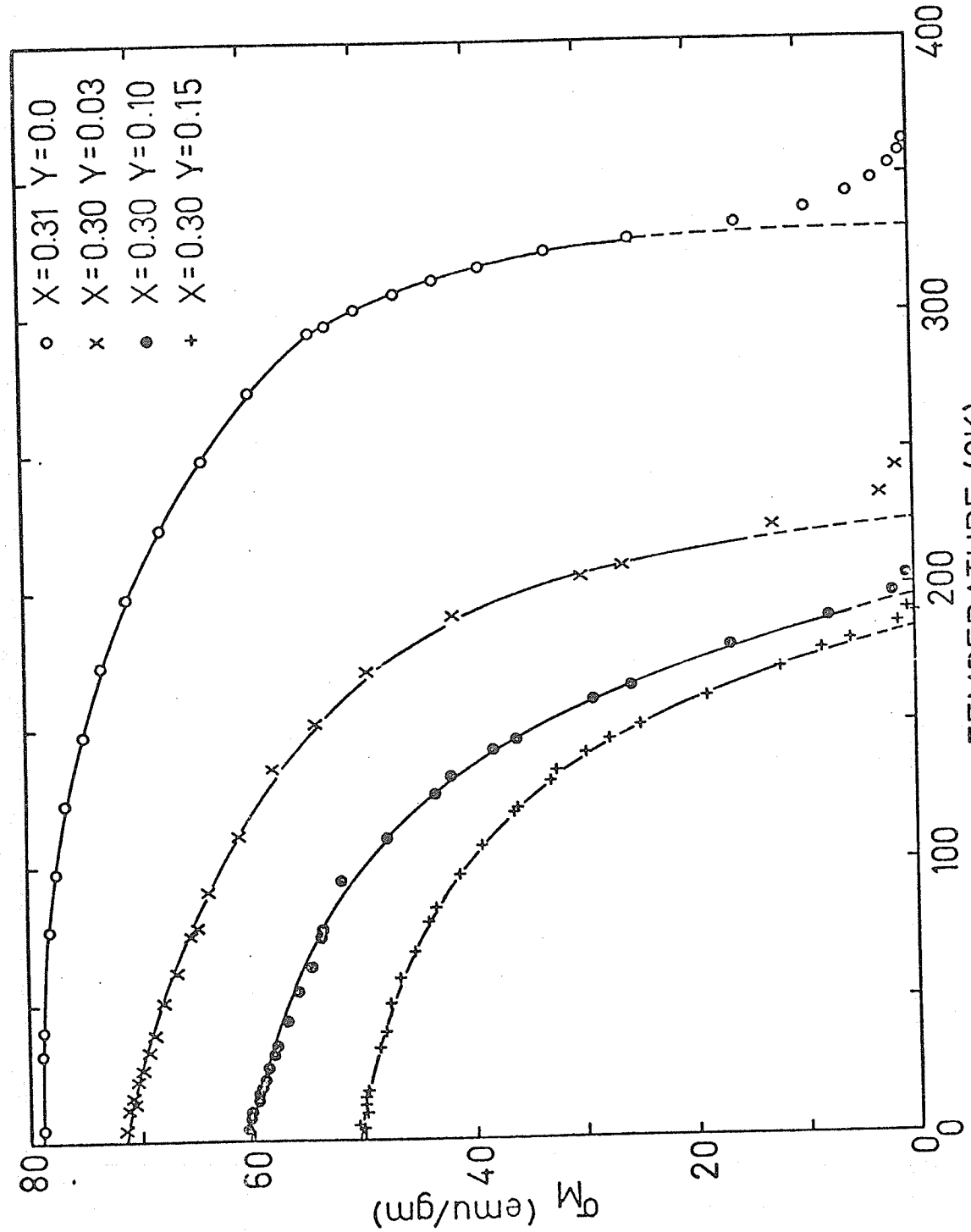

Fig. 44. Saturation magnetization of $La_{1-X}Pb_XMn_{1-Y}Fe_YO_3$ as a function of temperature. The full curves emphasize the trend of the data.

were obtained by extrapolation and tabulated with the extrapolated saturation moments at $0^{o}K$ in Table XIV.

Table XIV. Curie Temperatures and Saturation Magnetization of $La_{1-X}Pb_{X}Mn_{1-Y}Fe_{Y}O_{3}$

X	Y	T_c (^{o}K)	$\sigma_{exp}(0)$ emu/gm	$\sigma_{theor}(0)^{*}$ emu/gm
0.31	0	330	78.8	78.5
0.30	0.03	224	71.4	73.0
0.30	0.10	196	60.5	59.6
0.30	0.15	184	50.7	50.0
0.44	0	350	74.8	73.2
0.44	0.03	252	61.9	67.7
0.44	0.10	220	52.1	54.7
0.44	0.17	176	40.7	43.4
0.20	0.10	172	62.0	62.4

* Spin-only value assuming iron antiparallel to manganese spin

3.5 NMR DATA

The experimental setup is the same as that described in section 2.7. Because of the lowering of the Curie temperature due to iron substitution shown in Table XIV, the spin echo amplitude becomes weaker and even unobservable for the highest iron doped (15 at.%) sample at $4.2^{o}K$. Most of the data were collected instead at $1.6\pm0.1^{o}K$

by pumping the helium with a large capacity mechanical vacuum pump. Here instead of one single absorption line as observed in the undoped samples described in section 2.6 two extra side lines appear as shown in Fig.45. For powder sample it is reasonable to estimate the demagnetization field by $4\pi/3\ M_s$. From the line position, the hyperfine fields corresponding to Mn^{3+} and Mn^{4+} have been determined. Using $\langle s_z \rangle = 4\mu_B$ for Mn^{3+} and $3\mu_B$ for Mn^{4+}, the hyperfine constants are tabulated together with the hyperfine fields in Table XV. The identification of the absorption peaks with Mn^{3+} and Mn^{4+} was done by comparing with other published results on oxides [55-60]. The comparison is shown also in Table XV. The relaxation time T_{eff} ($\sim T_2$) is shown in Fig.46.

3.6 DISCUSSION

The spectra at 297°K show two pairs of absorption lines. In order to see if they correspond to two different sites, we did the following experiment. The recoilless fraction f in the Debye approximation can be written as [61]

$$f = \exp\left[- 6E_r T/k\Theta_D^2 \right] \qquad (8)$$

for $T > \Theta_D/2$. Here E_r is the recoil energy and k the Boltzmann constant. The f value is proportional to the total absorption, or to the area of a Mössbauer spectrum. Therefore, a comparison of the temperature

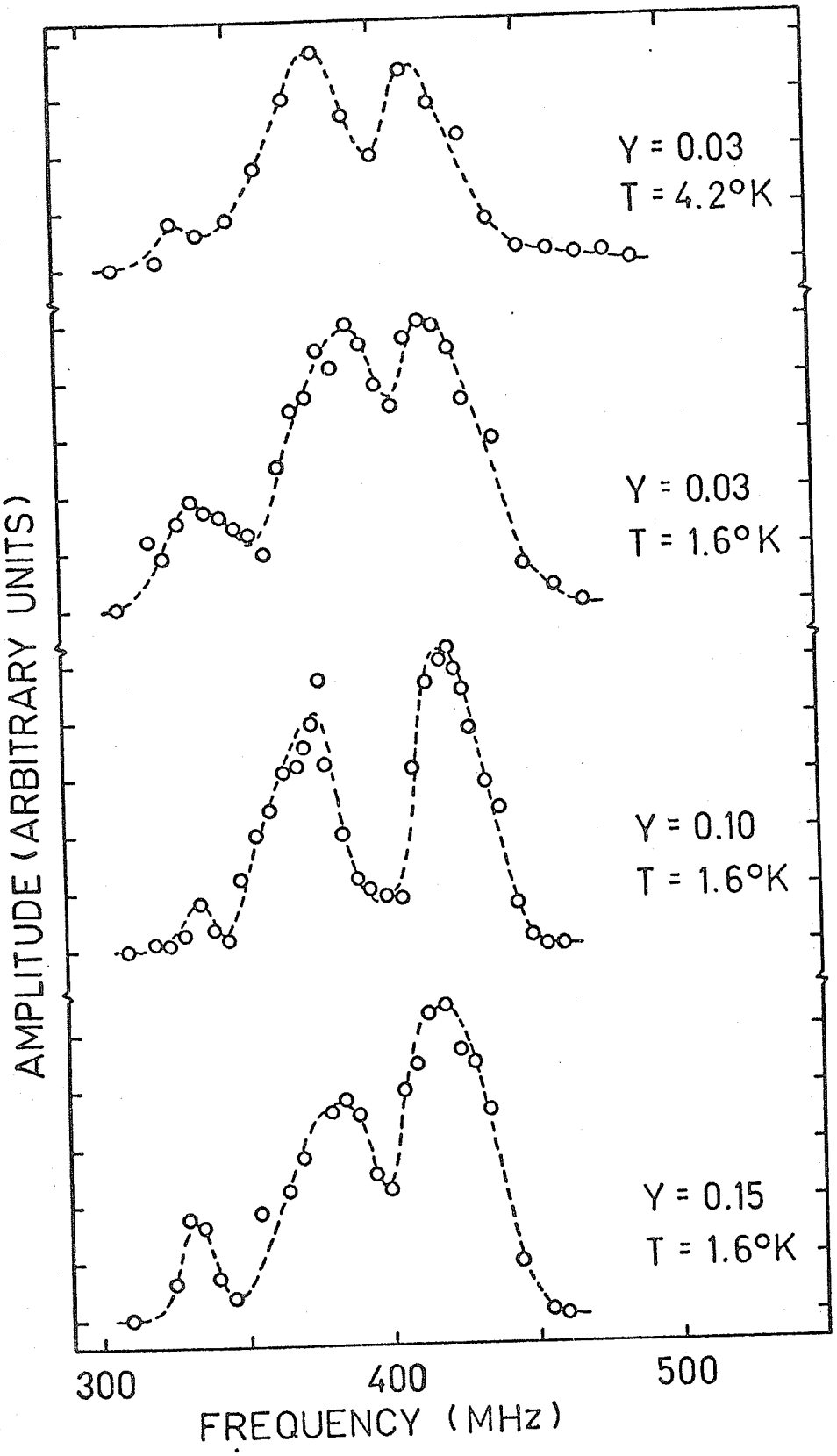

Fig. 45. NMR spectra of $La_{0.7}Pb_{0.3}Mn_{1-Y}Fe_YO_3$.

Table XV. Results of Data Analysis of NMR Spectra for $La_{0.7}Pb_{0.3}Mn_{1-Y}Fe_YO_3$ with other Published Values.

Ion	A (10^3xcm^{-1})	H_{hf} (kOe)	Freq.(MHz)
Mn^{3+}	7.1	402 ± 5	422 ± 5
Mn^{4+}	7.4	317	332

Ion	Method	|A| (10^3xcm^{-1})	Freq.(MHz)	Ref.
Mn^{3+}	NMR	53 and 83	250 430 (1.6°K)	55
Mn^{3+}	NMR		350 435 (4.2°K)	56
Mn^{3+}	NMR		300 470 (4.2°K)	60
Mn^{4+}	ESR	7.2		57
Mn^{4+}	ESR	7.0 ± 0.5		58
Mn^{4+}	NMR	-7.0	317 (0°K)	59
Mn^{4+}	NMR	7.2	320 (4.2°K)	56

dependences of the areas of the two pairs of lines will indicate whether or not they can be described by different Debye temperatures. If so, then it is reasonable to conclude that they correspond to two different iron sites. Of course, the existence of two sites is not disproved by a negative result. Spectra of $La_{0.70}Pb_{0.30}Mn_{0.85}Fe_{0.15}O_3$ were taken at four temperatures as shown in Fig.34 and the data are shown in Fig.47. From the slopes of the least-

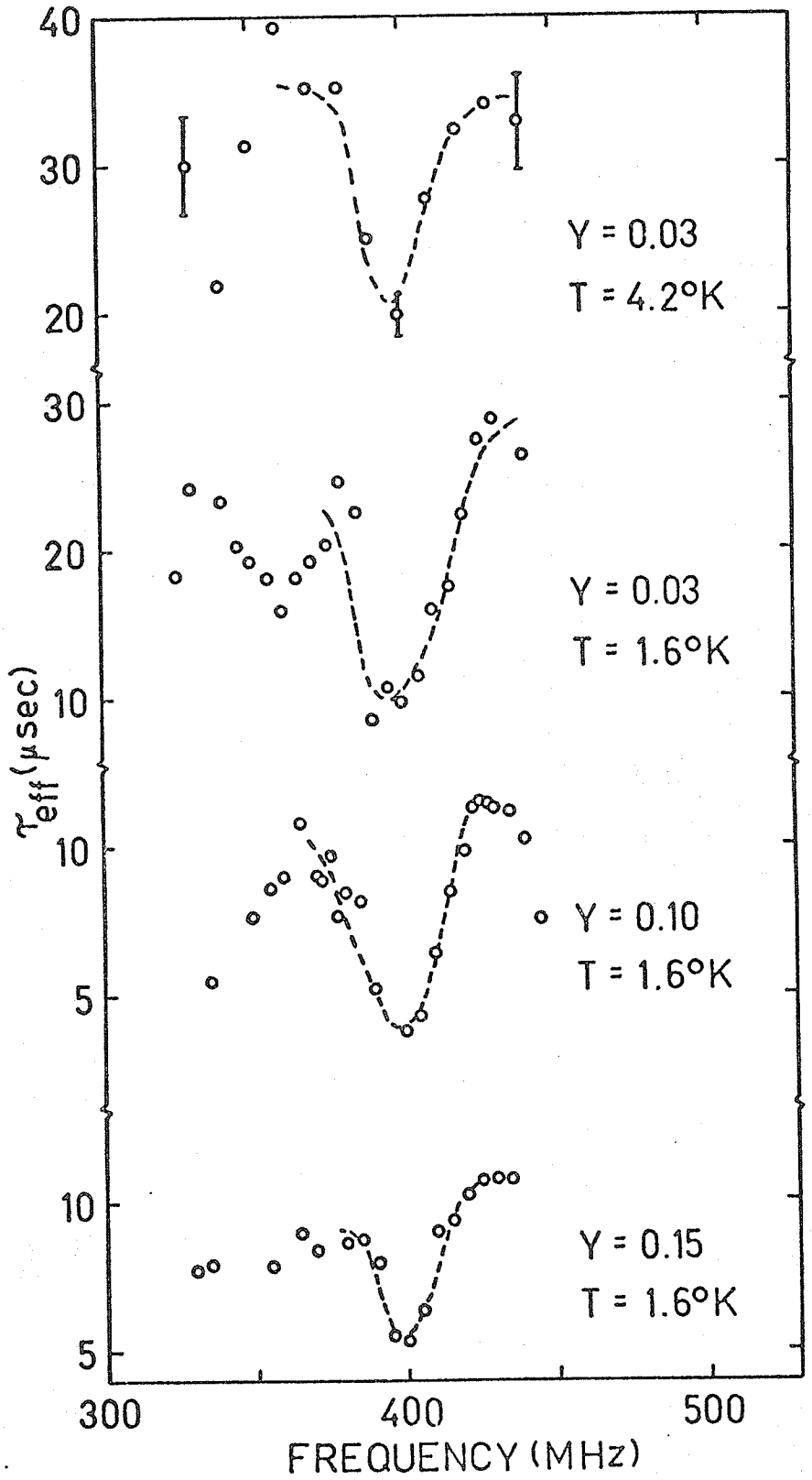

Fig. 46. Effective relaxation time of $La_{0.7}Pb_{0.3}Mn_{1-Y}Fe_YO_3$ as a function of frequency.

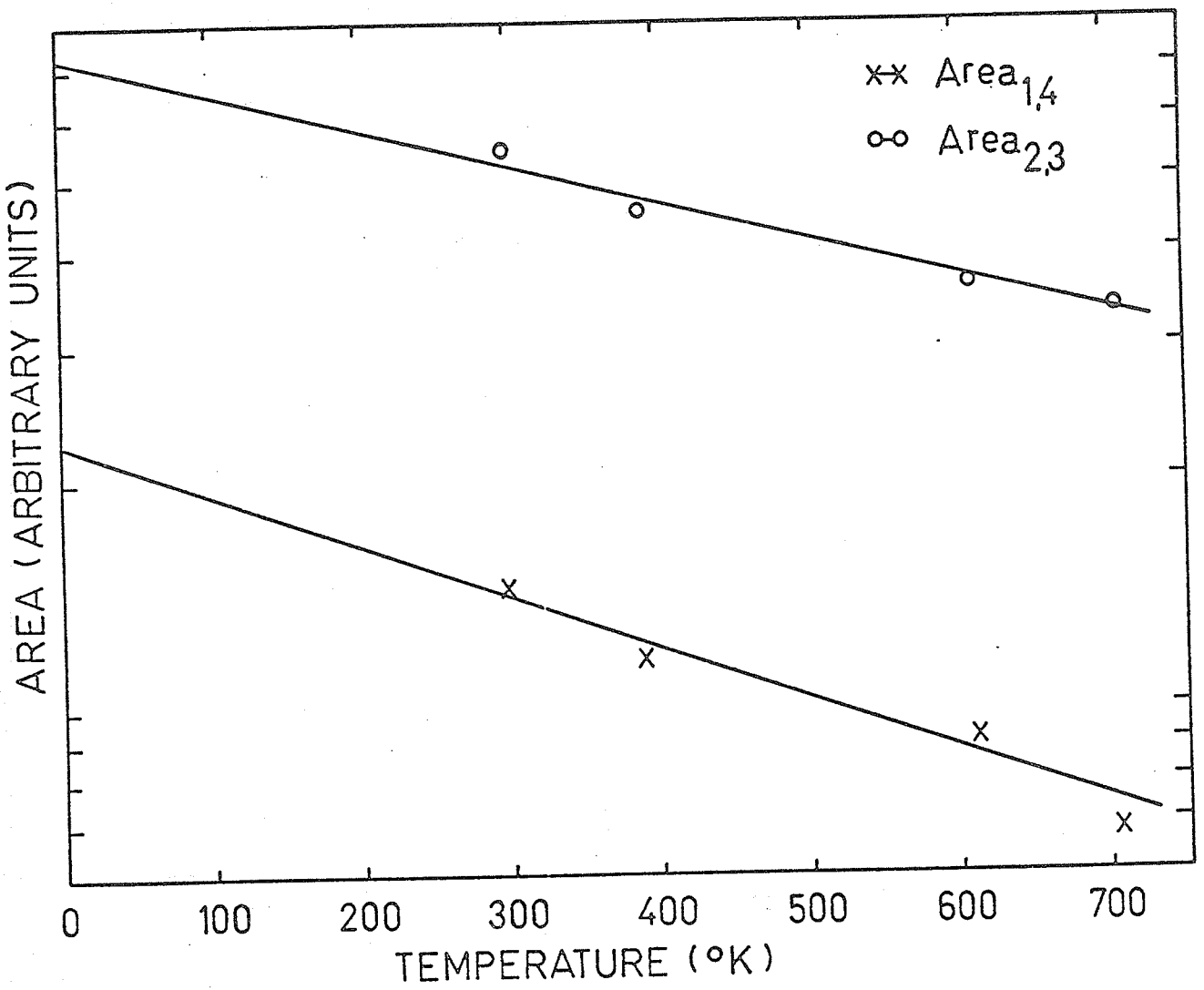

Fig. 47. A plot of areas of the Mössbauer spectra for $La_{0.70}Pb_{0.30}Mn_{0.97}Fe_{0.03}O_3$ in logarithmic scale versus temperature. The solid lines are the least-squares fits of thedata.

squares fitted lines, two Θ_D are found. They are $352 \pm 17^{\circ}K$ and $297 \pm 23^{\circ}K$ corresponding to the inner pair and the outer ones respectively. Further, a higher value for Θ_D suggests a tighter bonding to the lattice. Thus, the identification of sites in section 3.1 is justified. The constancy of isomer shifts shown in Table XI for different X and Y values suggests that the s-electron density at the nucleus stays quite constant within experimental error. This is further supported by the small change in hyperfine field as a function of X shown in Table XII. The value ~ 0.55 mm/sec suggests they are Fe^{3+} in both sites. The quadrupole splitting of Fe^{3+} ion, because of its spherical wave function, depends solely on its surroundings. From the data it does not seem to have any obvious correlation with the lattice constant which does not follow any regular pattern as a function of X and Y as pointed out in section 3.2. However, the quadrupole splitting as a function of X and Y does have some regularities as shown in Figs. 35 and 36. For constant Y value, the quadrupole splitting $(e^2qQ/2)_{1,4}$ associated with the outer pair of lines stays almost constant while the one corresponding to the inner pair $(e^2qQ/2)_{2,3}$ increases linearly as a function of X. For the series with constant X values, the splitting associated with the outer pair decreases sharply as a function of Y while the one with the inner pair increases moderately. The irregularities in the lattice constants and the complexity due to different substitutions suggest that a quantitative estimation of the quadrupole splitting is extremely difficult if not impossible. Here no such attempt is made.

As pointed out in Section 2.1, the Goldschmidt tolerance factor t concerning the relative ionic radii of the components is the condition for crystallization in the perovskite structure. In the following, we try to give a qualitative explanation based on the difference in ionic radii of the components. The ionic radii of La^{3+}, Pb^{2+}, Fe^{3+}, Mn^{3+} and Mn^{4+} are 1.016Å 1.20Å, 0.64Å, 0.66Å and 0.60Å respectively.

Let us compare the case when Fe^{3+} substitutes for Mn^{3+} or Mn^{4+} with the case when Fe^{3+} substitutes for La^{3+} or Pb^{2+}. Since the ionic radius of Fe^{3+} is so close to Mn^{3+} and so is the charge, we expect $(e^2qQ/2)_{2,3}$ to be small but this is not the case between Fe^{3+} and La^{3+} or Pb^{2+} and $(e^2qQ/2)_{1,4}$ is expected to be large. This is consistent with the observed result. When we change X, because of the difference in ionic radii of Pb^{2+} and La^{3+}, the tolerance factor t changes further from its value for a cubic structure (i.e. 1.0), $(e^2qQ/2)$ is expected to increase but the difference in radii is small and the change in $(e^2qQ/2)$ as a function of X is expected to be small. This agrees quite well with that shown in Fig.35. When Y is changed, and since the ionic radius of Fe^{3+} is only half of Pb^{2+} or La^{3+}, $\Delta(e^2qQ/2)$ is expected to be large and this is indeed observed as shown in Fig.36. The decrease of $(e^2qQ/2)_{1,4}$ as a function of Y seems to suggest that as more Pb^{2+} or La^{3+} sites are occupied by Fe^{3+}, some sort of averaging mechanism on the crystal structure appears and the Fe^{3+} in the La^{3+} or Pb^{2+} site sees a less distorted surround-

ing. The $(e^2qQ/2)$ shown in Fig.34 is almost temperature independent, which is expected of a Fe^{3+} ion and further supports the above suggestion that in both sites all iron ions are of 3+ charge. At temperatures below the ordering temperature, the average hyperfine field has a different temperature dependence compared with that of the magnetization. Fig.48 shows the reduced magnetization versus the temperature and Fig.49 the reduced hyperfine field versus the temperature. It is obvious that the magnetization varies very differently as a function of temperature depending on its Y value. However, it is not the case for the hyperfine field which seems to follow a Brillouin function of s = 5/2 which is simply the electronic moment of Fe^{3+} ion.

A comparison of the spectra in Fig.51, especially the regions shown by the arrow heads, suggests that the Fe^{3+} ions at the La or Pb sites have a much lower ordering temperature than those Fe^{3+} ions at the Mn sites. This is not surprising because the bond angle of the exchange interaction Fe-O-Mn is 90° which is known to be very weak [65] compared with the 180° superexchange and the direct overlap for the Fe^{3+} ion with the Mn ion is known [65] to be negligible. Further, the shape of the spectrum at $147^{\circ}K$ (see Fig.41) typifies a relaxation spectrum of $\tau \sim 10^{-9}$ sec.

The areas under different six-line patterns used to fit the spectra at $7^{\circ}K$ (see Figs.37 and 39) are tabulated in Table XVI along with a set of theoretical values based on equation (7). The agreement

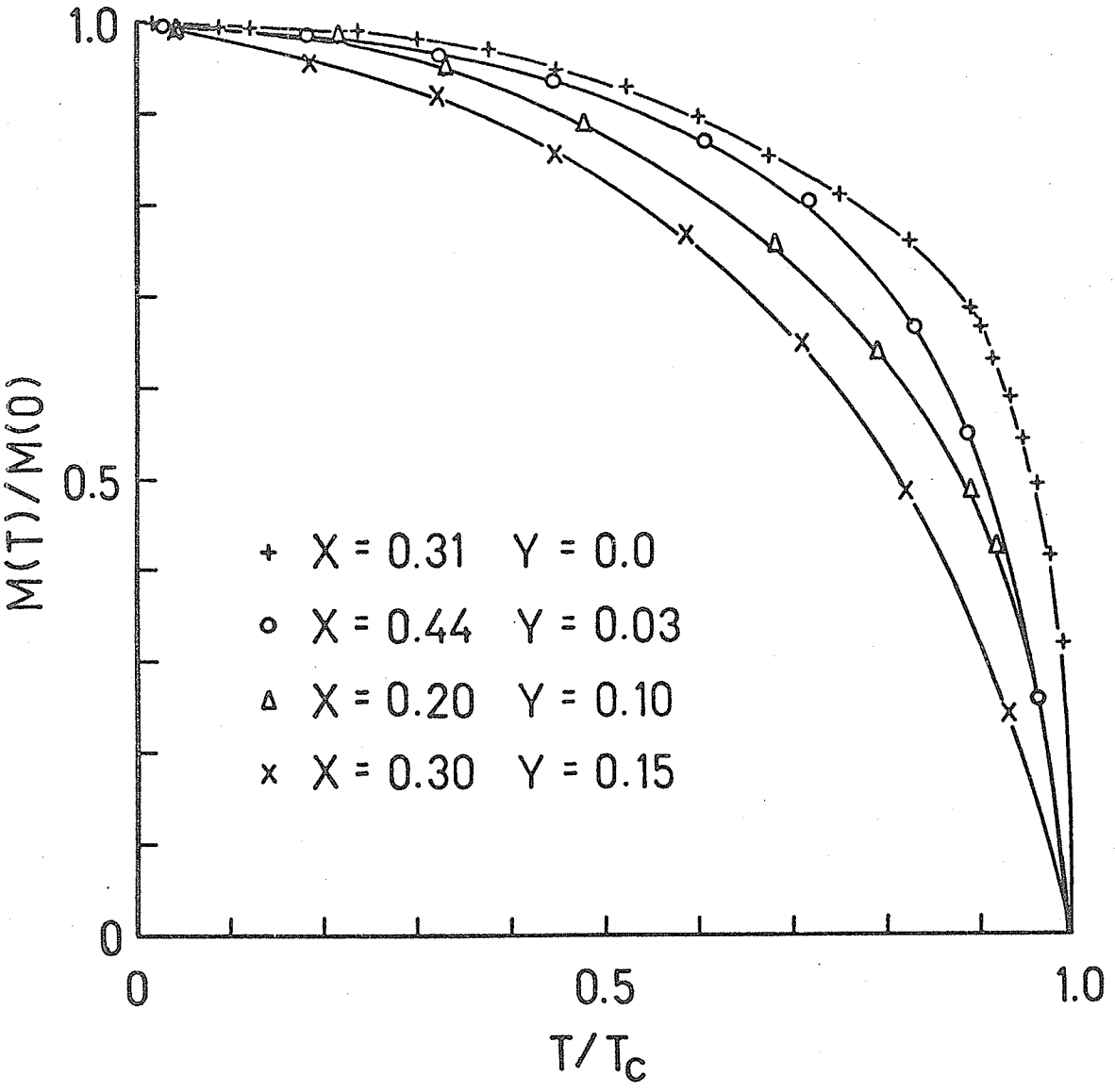

Fig. 48. Reduced saturation magnetization as a function of reduced temperature for $La_{1-X}Pb_XMn_{1-Y}Fe_YO_3$.

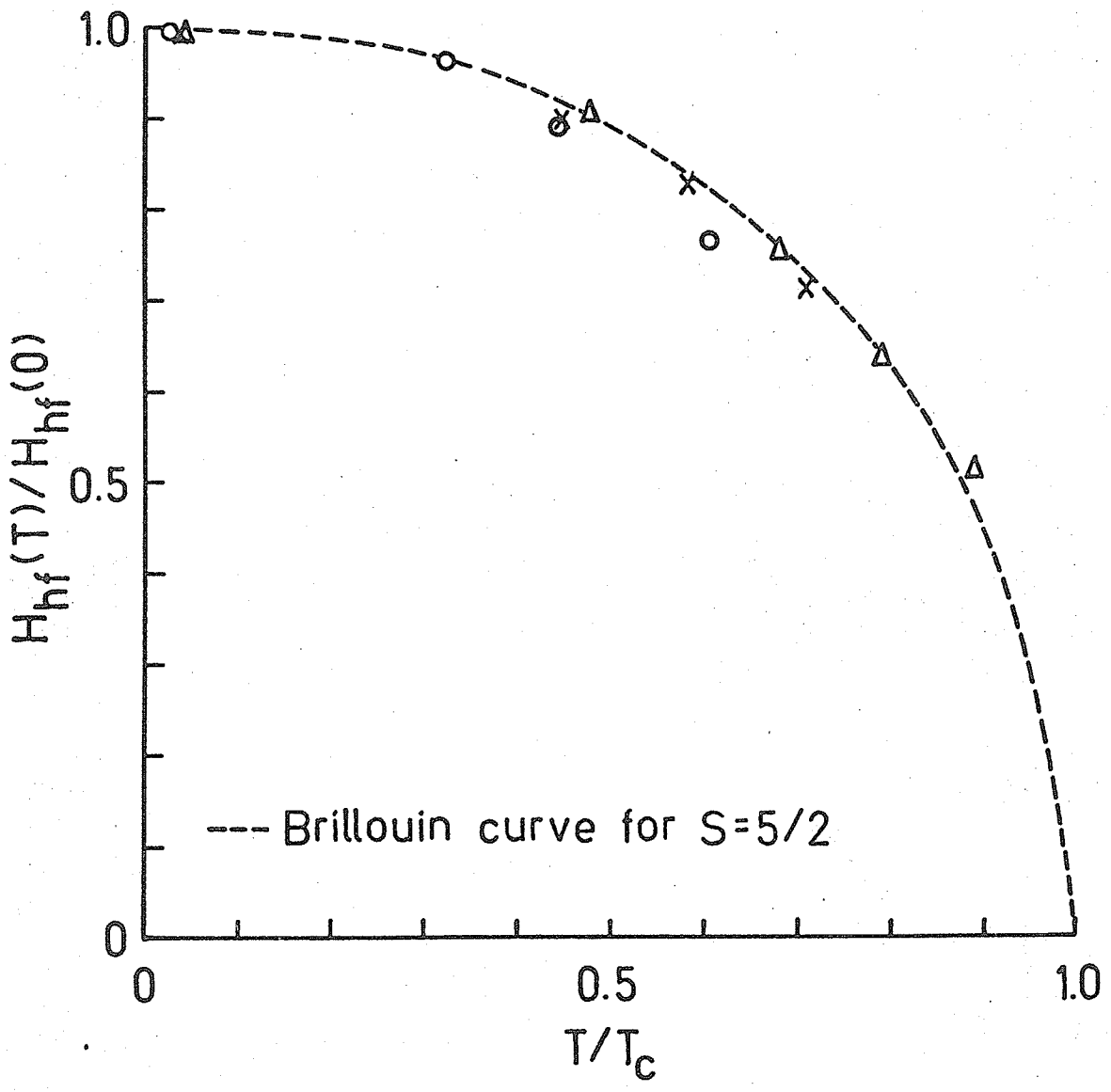

Fig. 49. Reduced hyperfine field as a function of reduced temperature for $La_{1-X}Pb_XMn_{1-Y}Fe_YO_3$. The meaning of symbols is the same as those given in the inset to Fig. 48.

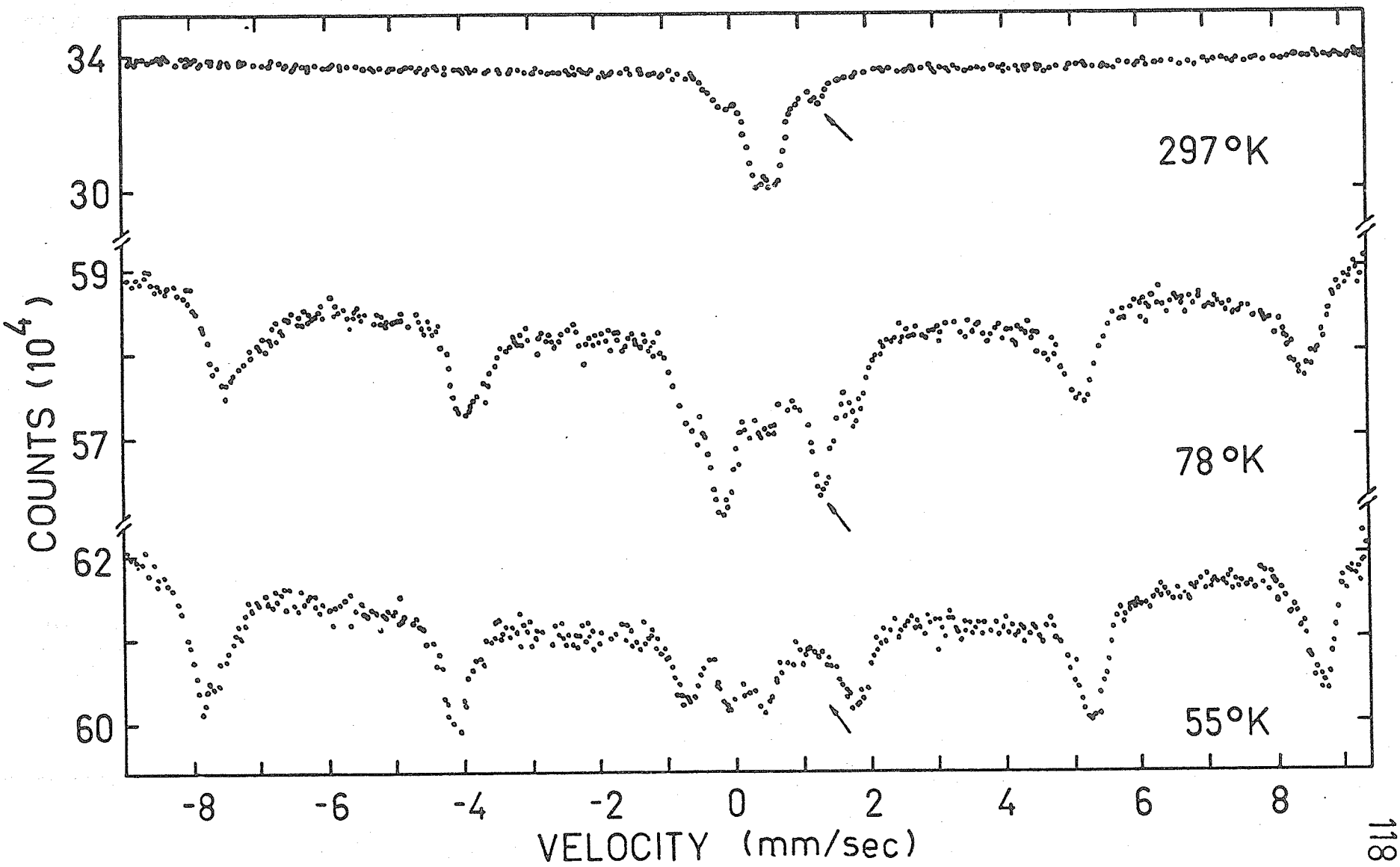

Fig. 51. Mössbauer spectra of $La_{0.56}Pb_{0.44}Mn_{0.97}Fe_{0.03}O_3$ at different temperatures. The arrowheads indicate the position of the paramagnetic peaks corresponding to the Fe^{3+} ions at the La/Pb sites.

Table XVI. Areas under Six-line Patterns of $La_{0.7}Pb_{0.3}Mn_{1-Y}Fe_YO_3$.

Fe at.%	Fe neighbour	P_{Theory}	$P_{(0\ kOe)}$	$P_{(50\ kOe)}$
3%	0	83.3	81.4	81.4
	1	15.5	12.9	7.4
	2	1.2	5.7	11.2
10%	0	53.1	53.5	55.7
	1	35.4	26.8	22.1
	2	9.8	19.7	22.2
	3	1.5		
15%	0	37.7	48.6	44.1
	1	39.9	30.9	35.9
	2	17.6	20.5	20.0
	3	4.1		
	4	0.3		

is very good. Further, the fitting with intensity constraint (see Fig.38) gave a chi-square value no worse than the unconstrained fitting as shown in Table XVII. This indicates that the statistical model is basically correct. The fitting suggests that the more the neighbouring ions are substituted by Fe ions the smaller will be the hyper-

Table XVII. Chi-square Values of Computer Fits of $La_{0.7}Pb_{0.3}Mn_{1-Y}Fe_YO_3$ Spectra with Different Constraints.

Fe Content	Intensity Constrained	Intensity Unconstrained
3%	568	600
10%	1285	1070
15%	1265	1305

fine field. A similar phenomenon has also been observed in many ferromagnetic alloys [62]. Using a formula,

$$H(m,n) = H_{Fe}(1 + an + bm)(1 + kc) \qquad (9)$$

where H(m,n) is the hyperfine field for an Fe atom with n impurity nearest neighbours,nn, and m impurity next nearest neighbours, nnn, in an alloy of atomic impurity concentration c and a, b the fractional change in hyperfine field per nn and nnn impurity atom respectively, Wertheim et al. [62] found that a has a range of values from −0.065 to −0.083, b from −0.01 to −0.07 and k from 0 to 0.4. For our case, we simply consider the nn effect. We believe this is justified. First of all, the resistivity of our undoped sample ($\sim 10^{-3}$ ohm cm) is still much higher than that of metals ($\sim 10^{-6}$ ohm cm) and in turn it implies that the d band is fairly narrow. Secondly, the excellent spectra fitting further supports this. Using the first

two patterns we obtained a = -0.073 ± 0.002 and k = -0.25 ± 0.04. However, a equals ~ 0.09 if the first and third patterns are used. We believe the additivity of neighbour effects observed in alloys should still be valid in our case. In our computer fitting, we considered the cases only up to two iron nn and thus the third pattern is not simply due to two iron nn but rather a weighted average of two to six iron nn and this results in a higher a value. This observed result is quite consistent with the simple band model proposed by Searle and Wang [40]. Here the substituted Fe^{3+} ion acts as a trap [63] or simply a scattering center for the mobile Zener electrons because of its spin direction being antiparallel to that of Mn spin. This fact is determined from the spectra with external field as shown in Fig.39. In this way, the d electron core-polarization which is believed to be the dominant contribution to the hyperfine field in this material is locally reduced and it results in a lower observed hyperfine field.

The line width increasing as a function of iron concentration suggests that the nnn effect does exist even though based on the computer fitting result it is going to be small compared with that of alloys. The data of the spectra with external field indicate that whenever an Fe ion sees one or more Fe ions as its nn, its spin becomes canted at an angle $\sim 60^{\circ}$ in the direction of the applied field. As presented in Table XIV, the measured moment agrees well with the calculated moment assuming all Fe spins are antiparallel to the Mn spin, which suggests that the Mn spins neighbouring the Fe site are

also canted. In addition, the spectrum shown as dotted curves in Figs. 37 and 39 corresponding to the No. 1 and 4 absorption lines in the spectrum at 297°K suggests that the large quadrupole splitting persists even in the presence of an external field of 50 kOe. This can simply be explained by recalling the Hamiltonian for the quadrupole interaction given in section 2.6.5.3. By standard second-order perturbation theory, the second-order term is given by

$$E_m^{(2)} = -h\left(\nu_Q^2/12\nu_L\right) m\left[3/2\,\mu^2(1-\mu^2)(8m^2-4a+1)+3/8(1-\mu^2)^2(-2m^2+2a-1)\right] \qquad (10)$$

where the same notations are used as that in section 2.6.5.3. It is obvious that this term will not be zero in the averaging process for a powder Mössbauer sample. This term can be neglected only if $e^2qQ \ll \mu H$.

In Figs. 43 and 44 the rapid decrease of the saturation magnetization curve near the Curie temperature, interpreted as the collapse of the double-exchange band in section 2.7.1, becomes less obvious, as the Fe concentration increases. This suggests that the Fe^{57} doped material can no longer be explained by pure double-exchange mechanism but rather a mixture with superexchange-mainly the Mn^{+}-O-Fe^{3+} interaction. This ties in nicely with the Mössbauer result that the Fe^{3+} spin is antiparallel to the Mn spin. The decrease of the Curie temperature as a function of Fe substitution is again expected because the competition between the double-exchange and

superexchange would lead to a weakening in the double-exchange mechanism. This is also consistent with the lowering of the hyperfine field as a function of Y. Fig.50 shows the saturation magnetization at T = 0 as a function of iron substitution. If the linearity suggested by the dotted line shown in Fig.50 holds for higher iron concentration, this suggests that at $Y \simeq 0.45$ the material becomes completely antiferromagnetic.

The NMR result at low temperature is very interesting indeed. Matsumoto [46,56] observed a similar phenomenon with the compound $(La_{1-X}Ca_X)MnO_3$ at very low X values, $X \lesssim 0.175$, where he explained the situation by proposing the formation of a ferromagnetic molecule at low temperature due to the d-hole being strongly bound to the sites neighbouring to a Ca^{2+} ion. Of course, this could also apply to our case. However, by examining the data (see Fig.45) closely, we notice that at the same temperature ($1.6^{o}K$) and the same X value (0.3) the intensities of the peaks associated with Mn^{3+} and Mn^{4+} ions increase as a function of iron substitution. This suggests that the Fe^{3+} ion plays an important role in the localization of the Mn^{3+} and Mn^{4+} ions, or in other words, the breaking down of the double-exchange in this case. Fe^{3+} has five d electrons. The iron substitution implies that extra electrons are introduced into the system and it has just the opposite effect compared with Pb substitution which creates d holes in the system. It is thus reasonable to suggest that the Fe^{3+} sites acting as traps for the d holes. Normally, for the interaction Mn^{3+}-O-Mn^{4+} the electron can move freely from the 3+ ion to the

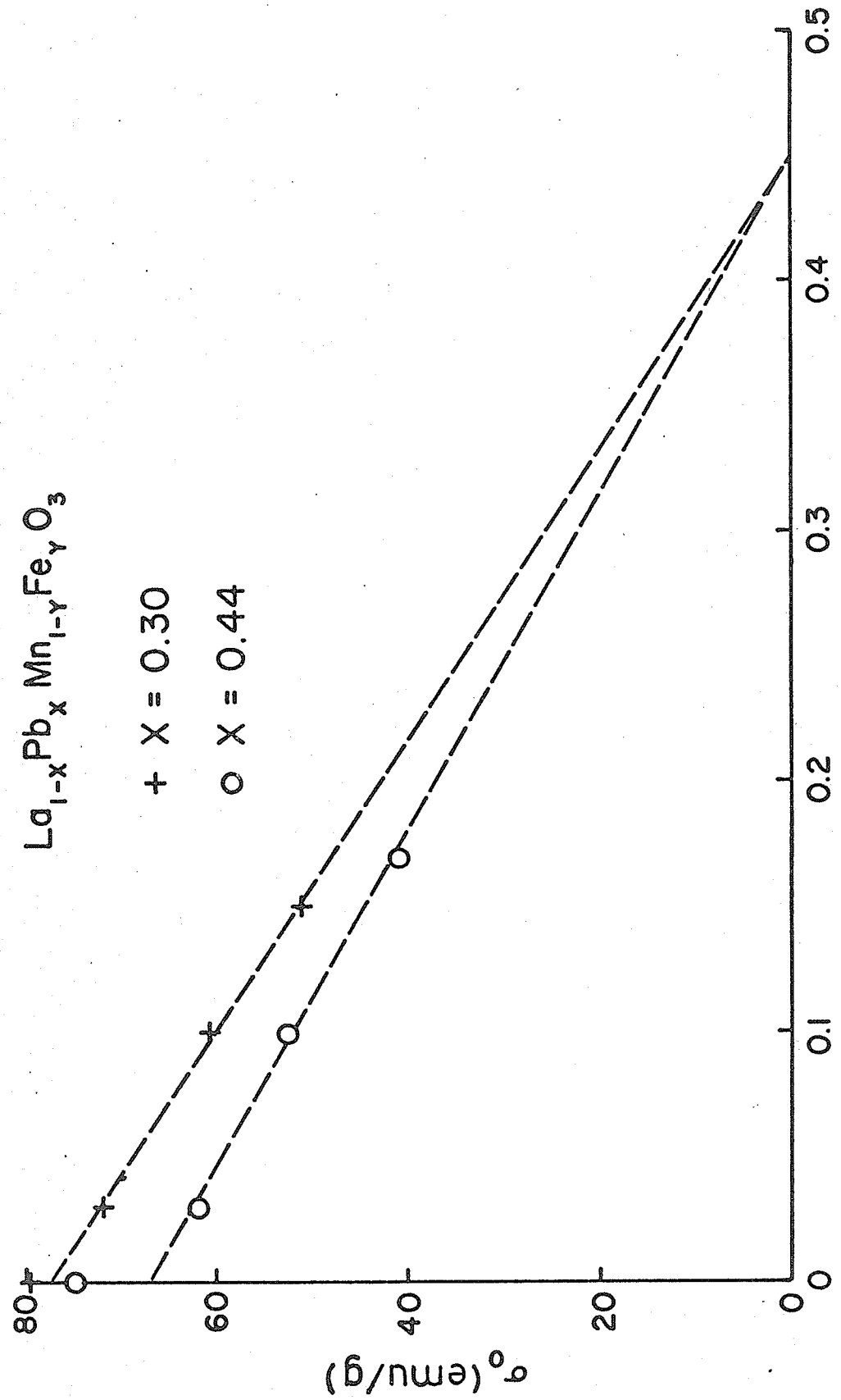

Fig. 50. Saturation magnetization of $La_{1-X}Pb_XMn_{1-Y}Fe_YO_3$ as a function of iron concentration.

4+ ion due to double-exchange. In other words, this implies that the d hole moves from the 4+ ion to the 3+ ion. When the Mn^{3+} ion is replaced by a Fe^{3+} ion we have the situation Fe^{3+}-O-Mn^{4+}. Because the Fe spin is antiparallel to the Mn spin (a direct result of the Mössbauer measurement) and because the d-electrons of the Fe ion are known to be more localized than those of the Mn ion [63], the double-exchange mechanism no longer applies. This results in a localized d hole and in turn the observable NMR peaks corresponding to the Mn^{3+} and Mn^{4+} ions. Furthermore, a comparison of the spectra for the 3% iron substitution at 4.2°K and 1.6°K indicates that the intensities of the peaks associated with the Mn^{3+} and Mn^{4+} ions increase slightly as the temperature becomes lower and this is consistent with the theory proposed by Matsumoto. We therefore conclude that, for our compound, both mechanisms contribute with the trapping mechanism seeming to play a more dominant and effective role.

IV $Zn_xNi_{1-x}Fe_2O_4$

4.1 INTRODUCTION

In recent years there has been a revival of considerable interest in the local properties of disordered systems [66-74]. In particular, there have been several neutron diffraction and Mössbauer studies of the nickel-zinc ferrite, $Ni_{1-x}Zn_xFe_2O_4$ system [75-78]. As a consequence of these studies, it has been proven that, first of all, there is a canting of the B site spins and secondly, that the concentration of paramagnetic Fe^{3+} ions, either as single ions or clusters, is nowhere near as great as previously expected. In addition, a local-molecular-field model has been used to explain the saturation magnetization of the Ni-Zn-ferrite system with considerable improvements over previous attempts. This particular treatment of the saturation moments did not, however, allow for spin canting and there are small, but significant, deviations between the calculated and experimental moments at high Zn contents.

The considerable advancement in our understanding of the magnetic properties of the Ni-Zn-ferrites as a result of the above mentioned studies notwithstanding, there are still some cogent questions that remain to be answered. The correct interpretation

of some of the recently generated results also need to be clarified and confirmed by additional independent measurements. In addition, it is felt that it would be desirable to establish the corroborative aspects of the more recent results by performing a series of magnetic and Mössbauer measurements on identical specimens from chemically and strcturally well-characterized parent materials; this has not been done in any of the studies so far.

Most important among some of the unanswered questions, is the precise meaning of the canting angles deduced from the neutron diffraction studies. It is obvious that the neutron diffraction data permits one to deduce only the average B site canting angle. No information is obtained regarding the local canting angles of the spins of the Ni^{2+} and Fe^{3+} B site ions. In principle, the canting angles of the Ni^{2+} and Fe^{3+} ions are expected to be different on a local basis since the B-B and A-B exchange interactions, J_{BB} and J_{AB}, are known to be different [79] for Ni^{2+} and Fe^{3+}. In this regard, it is significant that the extrapolated canting angle of 90^{o} based on the neutron diffraction results, for the B site Fe^{3+} spins in pure $ZnFe_2O_4$ is apparently not in agreement with the observed, rather complicated, spin structure of $ZnFe_2O_4$ [80-81]. We have, therefore, determined the canting angle of the Fe^{3+} spins by means of Fe^{57} Mössbauer spectroscopy in external magnetic fields. We find that there are indeed differences between the (average) canting angles of the B site Fe^{3+} spins, determined

using Mössbauer spectroscopy, and the average canting angles of all the B site spins, determined using neutron diffraction. The relative magnitudes of the (average) Ni^{2+} and Fe^{3+} canting angles are qualitatively consistent with the predictions based on the relative strengths of the exchange interactions within the local-molecular-field approximation.

Secondly, there is the question for the cation distribution. While it is widely accepted that the site preference of Ni^{2+} and Zn^{2+} for the octahedral and tetrahedral sites, respectively, is great enough to assure one of the cation distribution $(Zn_XFe_{1-X})[Fe_{1+X}Ni_{1-X}]O_4$ for all values of X, the cation distributions have not been proven to correspond to the above formulation for all values of X. Through the improved resolution of the A and B site Fe^{57} Mössbauer spectra in external magnetic fields, we have determined at 7^{o} K the cation distribution. The accuracy of the resulting cation distributions is not limited by differences in the recoilless fractions at the A and B sites, f_A and f_B, since f_A/f_B is expected to be very close to 1.00 at 7^{o} K and inaccuracies in the cation distibutions deduced from the area ratios of the Mössbauer spectra will not be greater than 10%.

The possibility of local fluctuations in the magnetic properties of the Fe^{3+} ions is also discussed on the basis of a local-molecular-field model and local variations in the supertransferred hyperfine interactions. Line width considerations indicate that

variations in the hyperfine fields at Fe^{3+} ions due to local variations in molecular field parameters are negligible. From the isotropic decrease in the magnitude of the hyperfine fields, however, it is concluded that there are substantial variations in the supertransferred hyperfine interactions as the Zn content is varied.

Finally, to assure that the present data have some relevance to other studies, we have characterized each specimen in terms of its lattice parameter, chemical composition, saturation magnetization and Neel temperatures. The results, of these characterizations indicate that the materials used in this investigation are very similar to those used in previous studies. We can therefore be confident that points of differences and similarities between the results of the present study and previous ones are substantive and not due solely to differences in the materials under investigation.

4.2 EXPERIMENTAL

The ferrite specimens were prepared by wet grinding into intimate mixtures (specpure grade - Johnson-Matthey) powders of $ZnCO_3$, $NiCO_3$ and Fe_2O_3. The mixtures of powders were pressed into pellets and fired at 1000°C in a muffle furnace. The pellets were quenched in air, ground into a fine powder, repelletized and refired at 1200 - 1300°C; this sequence of operations was repeated until a single phase material was obtained, as determined by X-ray

powder diffractometry.

The chemical compositions of the samples were determined using wet chemical techniques [82]. Since there was a possibility of loss of Zn through volatilization, only the Zn content was determined. The closeness of the experimental weight percentages of the more volatile zinc to the nominal weight percentages makes it unlikely that the Ni and Fe contents are very different from their nominal values.

The lattice constants, the saturation magnetization and the Curie temperatures were arrived at in the same manner as that described in previous chapters. Also the same Mössbauer setup referred to in Chapter III was used.

4.3 RESULTS

The results of the chemical and X-rays analyses are shown in Table XVIII and Figure 52 and Table XIX, respectively. The

Table XVIII. Data of Chemical Analysis for Ni-Zn Ferrites.

Nominal Formulas	Zinc weight percent Found	Expected
$(Zn_{0.6}Fe_{0.4})[Ni_{0.4}Fe_{1.6}]O_4$	16.9 ± 0.2	16.5
$(Zn_{0.7}Fe_{0.3})[Ni_{0.3}Fe_{1.7}]O_4$	18.9 ± 0.1	19.2
$(Zn_{0.8}Fe_{0.2})[Ni_{0.2}Fe_{1.8}]O_4$	21.6 ± 0.2	21.8
$(Zn_{0.9}Fe_{0.1})[Ni_{0.1}Fe_{1.9}]O_4$	23.5 ± 0.1	24.4

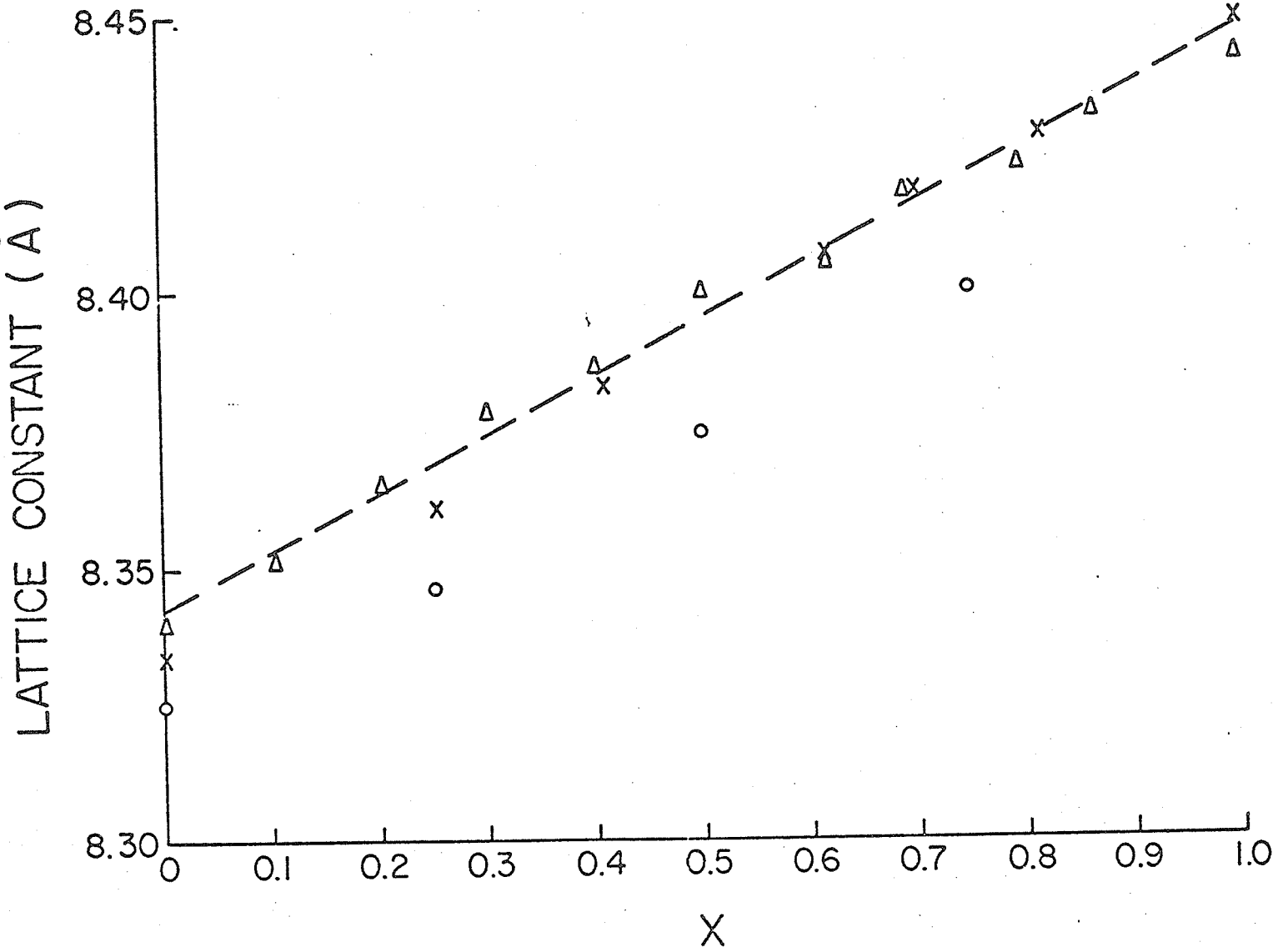

Fig. 52. Lattice constants vs. X values. (X) represents data from Daniels and Rosencwaig [78], (o) from Satya Murthy et al. [76] and (Δ) from this work. The dashed line emphasizes the linearity of the data.

Table XIX. Lattice Constants of Ni-Zn Ferrites.

Sample formula	a* (Å)
$(Fe)[NiFe]O_4$	8.340 ± 0.005
$(Zn_{0.1}Fe_{0.9})[Ni_{0.9}Fe_{1.1}]O_4$	8.351
$(Zn_{0.2}Fe_{0.8})[Ni_{0.8}Fe_{1.2}]O_4$	8.365
$(Zn_{0.3}Fe_{0.7})[Ni_{0.7}Fe_{1.3}]O_4$	8.378
$(Zn_{0.4}Fe_{0.6})[Ni_{0.6}Fe_{1.4}]O_4$	8.386
$(Zn_{0.5}Fe_{0.5})[Ni_{0.5}Fe_{1.5}]O_4$	8.399
$(Zn_{0.6}Fe_{0.4})[Ni_{0.4}Fe_{1.6}]O_4$	8.405
$(Zn_{0.7}Fe_{0.3})[Ni_{0.3}Fe_{1.7}]O_4$	8.417
$(Zn_{0.7}Fe_{0.2})[Ni_{0.2}Fe_{1.8}]O_4$	8.425
$(Zn_{0.9}Fe_{0.1})[Ni_{0.1}Fe_{1.9}]O_4$	8.432
$(Zn)[Fe_{2.0}]O_4$	8.442

* Determined from [5, 3, 3] with internal Si standard.

zinc weight percentages of the various specimens are quite close to their nominal values, even though there does appear to be some slight loss of zinc, as expected. The lattice constants for the specimens used in this study are given in Table XIX; they are compared with other previously reported values in

Fig.52.

The saturation moments, magnetizations and Curie temperatures are shown in Figs.53, 54 and 55, along with some previously reported determinations [83-85]. The agreement is again seen to be rather good. Where there are slight differences between the values found in this study and those of previous ones, we believe them to be due to differences in the actual chemical compositions.

Mössbauer spectra are shown in Figs.56 through 57. The solid lines through the data points are the results of least squares fit of the data to two mixed, magnetic and electric quadrupole hyperfine patterns. In the computer fitting, the shapes of the lines were assumed to be Lorentzian and their intensities and widths were allowed to vary freely subject only to the constraints that $I_j = I_{7-j}$ and $\Gamma_j = \Gamma_{7-j}$. For the zero-field spectra the relative integrated intensities of the lines between the two patterns were further constrained to have the values according to the chemical formula $(Zn_xFe_{1-x})[Ni_{1-x}Fe_{1+x}]O_4$. The linewidths, however, were allowed to be variable in every case subject only to the $\Gamma_j = \Gamma_{7-j}$ constraint.

The parameters derived from the least squares fits are listed in Tables XX and XXI. They are also plotted in Figs.58 through 63. The area ratios and angles, Θ, between the external field and B-site Fe^{3+} hyperfine field directions were derived

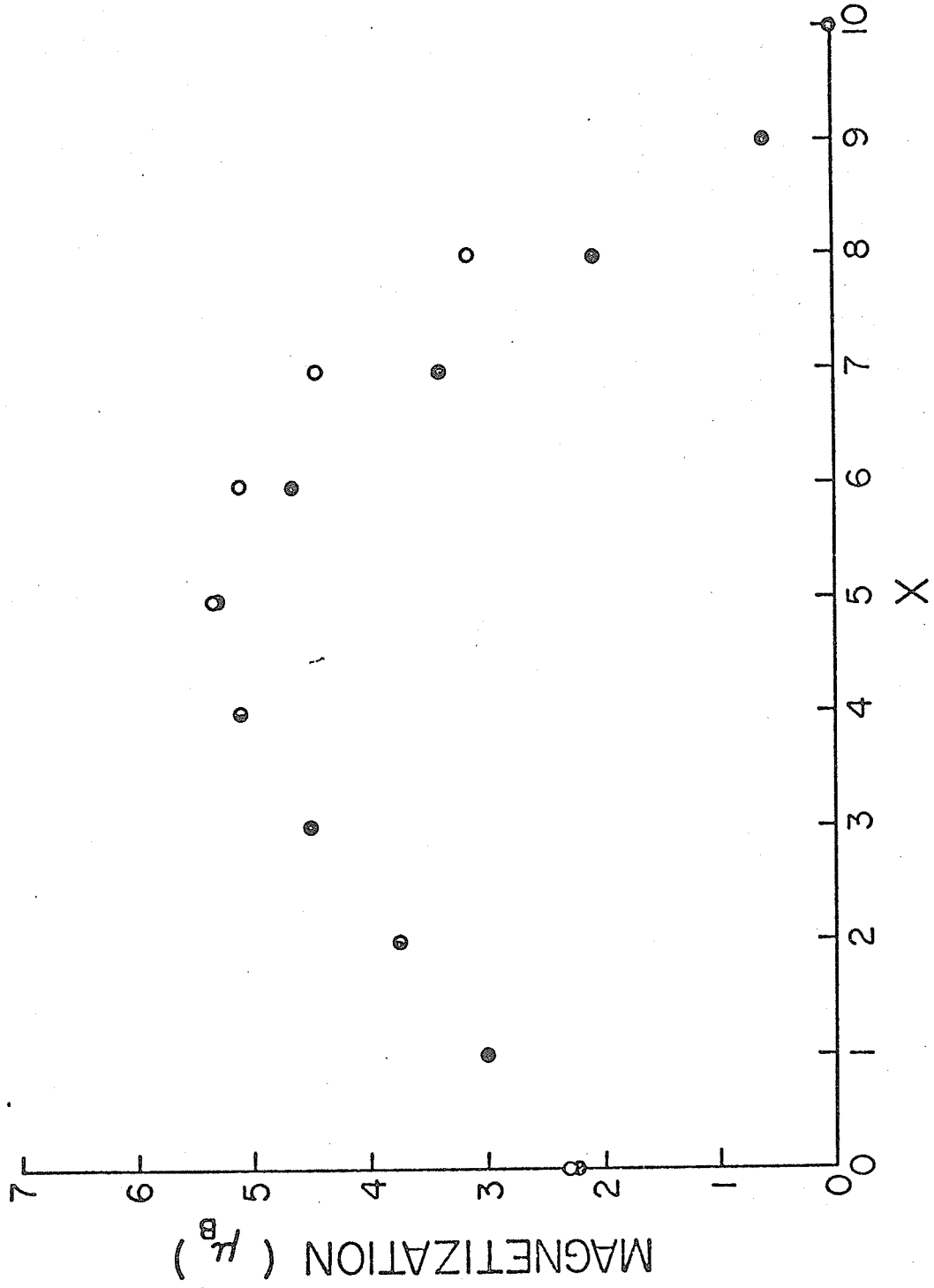

Fig. 53. Saturation magnetization at 4.2° K vs. X values. (o) represents data from Guilland et al. [83] for H → ∞ and (●) from this work for H = 0.

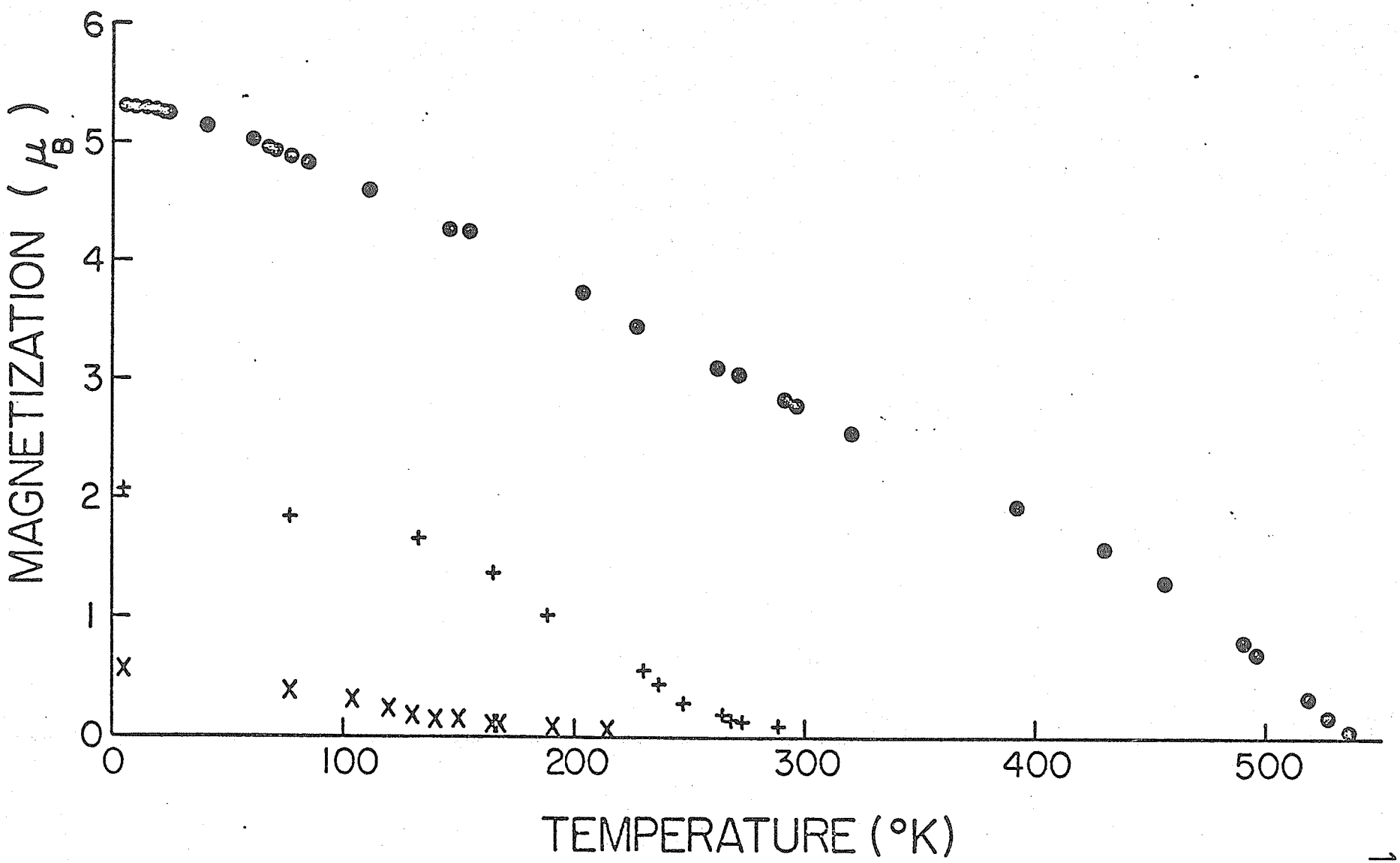

Fig. 54. Saturation moments as a function of temperature for three compositions: (●) for X = 0.5; (+) X = 0.8 and (X) X = 0.9.

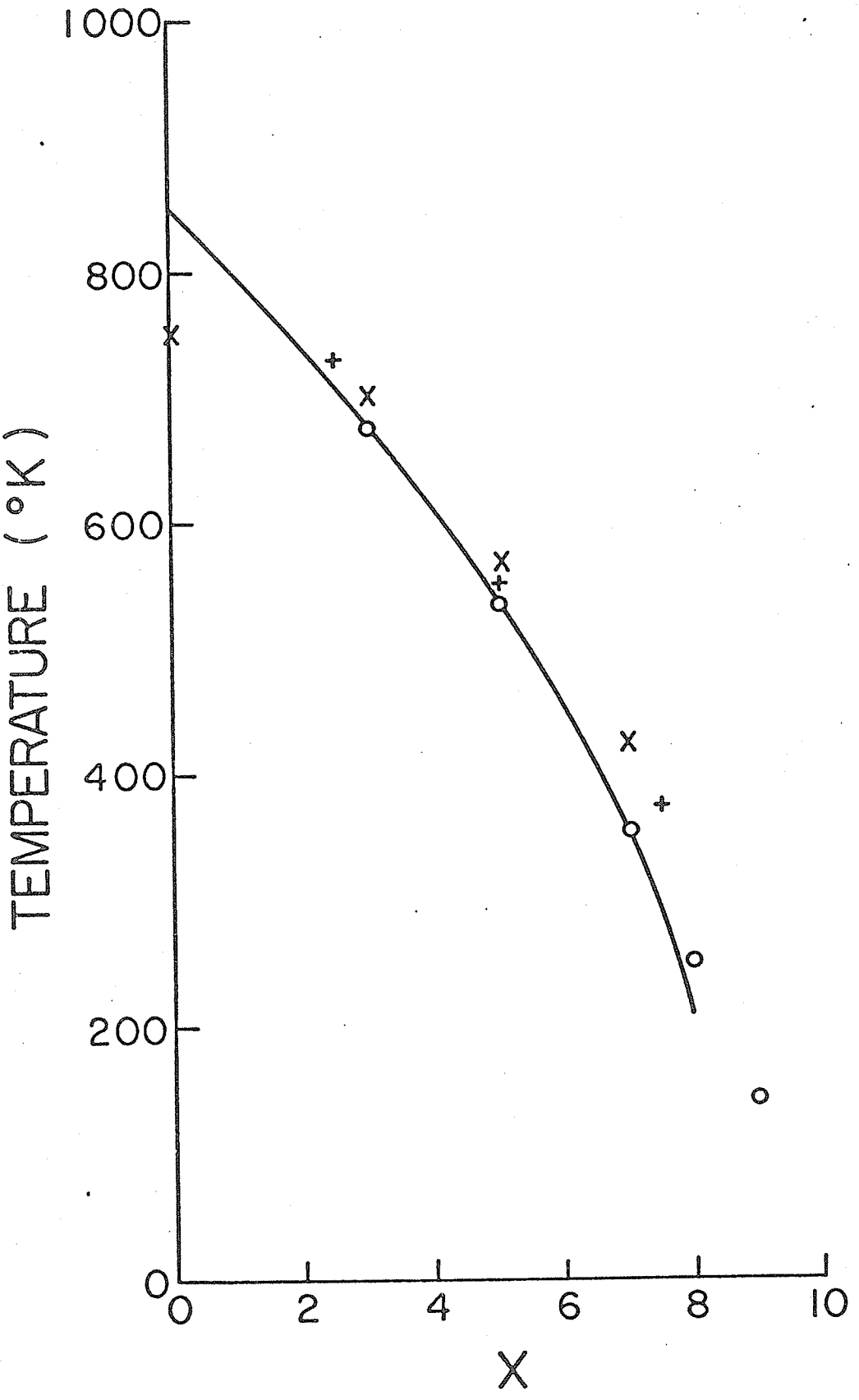

Fig. 55. Curie temperature vs. X values. The solid curve represents data from K. A. Piskarev [84], (X) from J. G. Booth and J Grangle [85], (+) from Satya Murthy et al. [76] and (o) from this work.

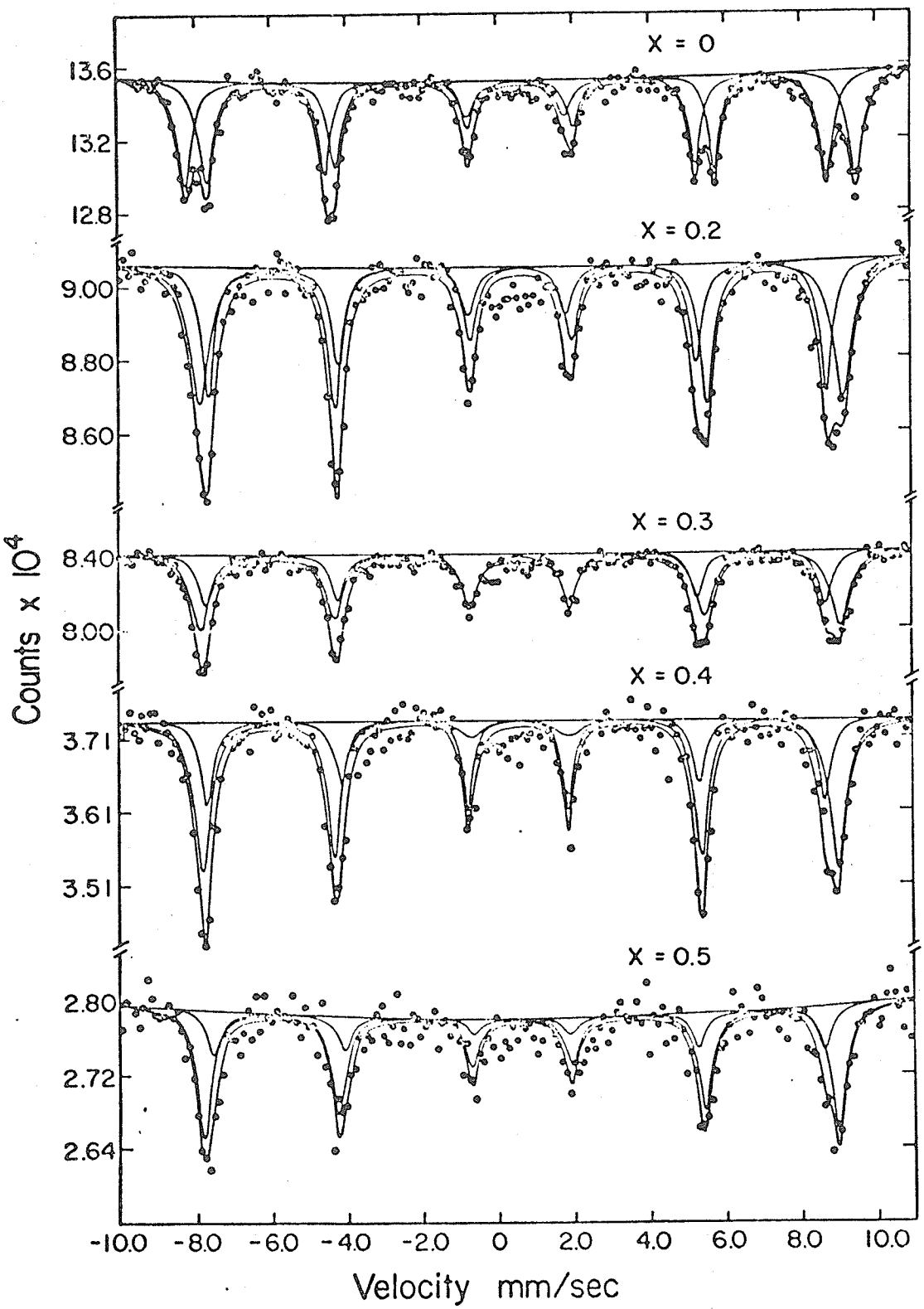

Fig. 56a. Mössbauer spectra of $Zn_XNi_{1-X}Fe_2O_4$ at 7° K. The solid curves are the computer fits.

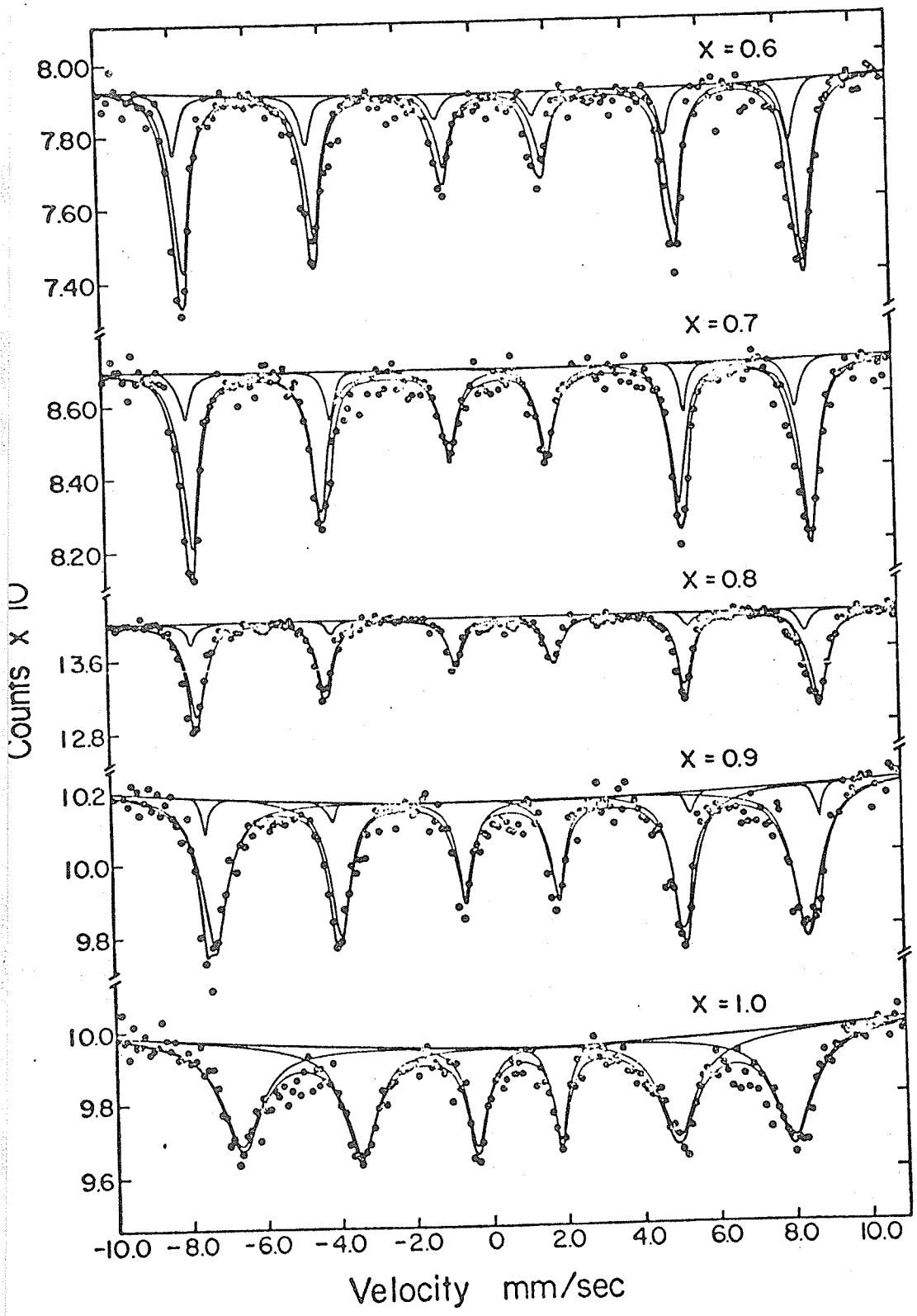

Fig. 56b. Mössbauer spectra of $Zn_xNi_{1-x}Fe_2O_4$ at 7° K. The solid curves are the computer fits.

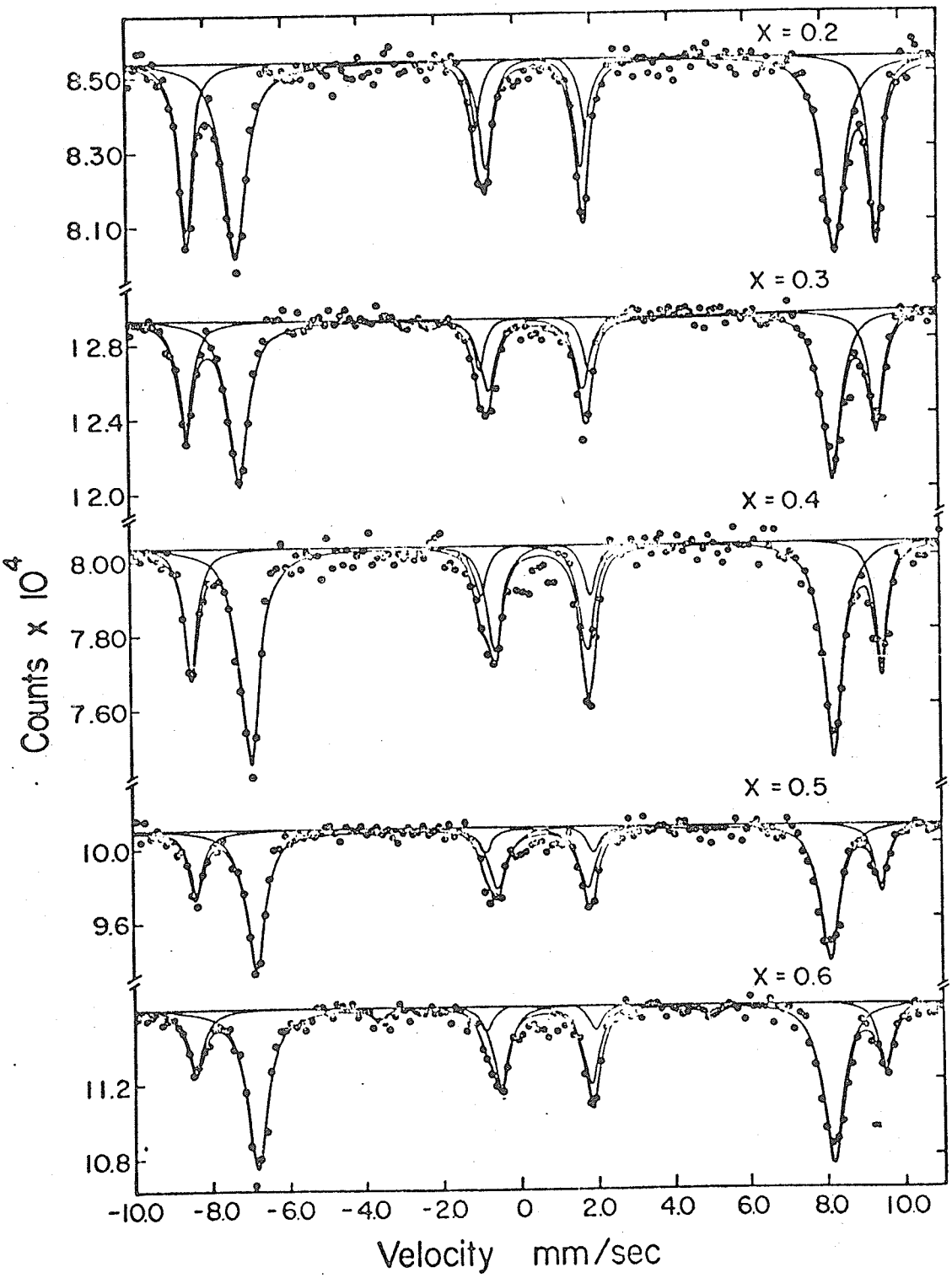

Fig. 57a. Mössbauer spectra of $Zn_xNi_{1-x}Fe_2O_4$ at 7° K with an external field of 50 kOe parallel to the direction of propagation of the ray. The solid curves are the computer fits.

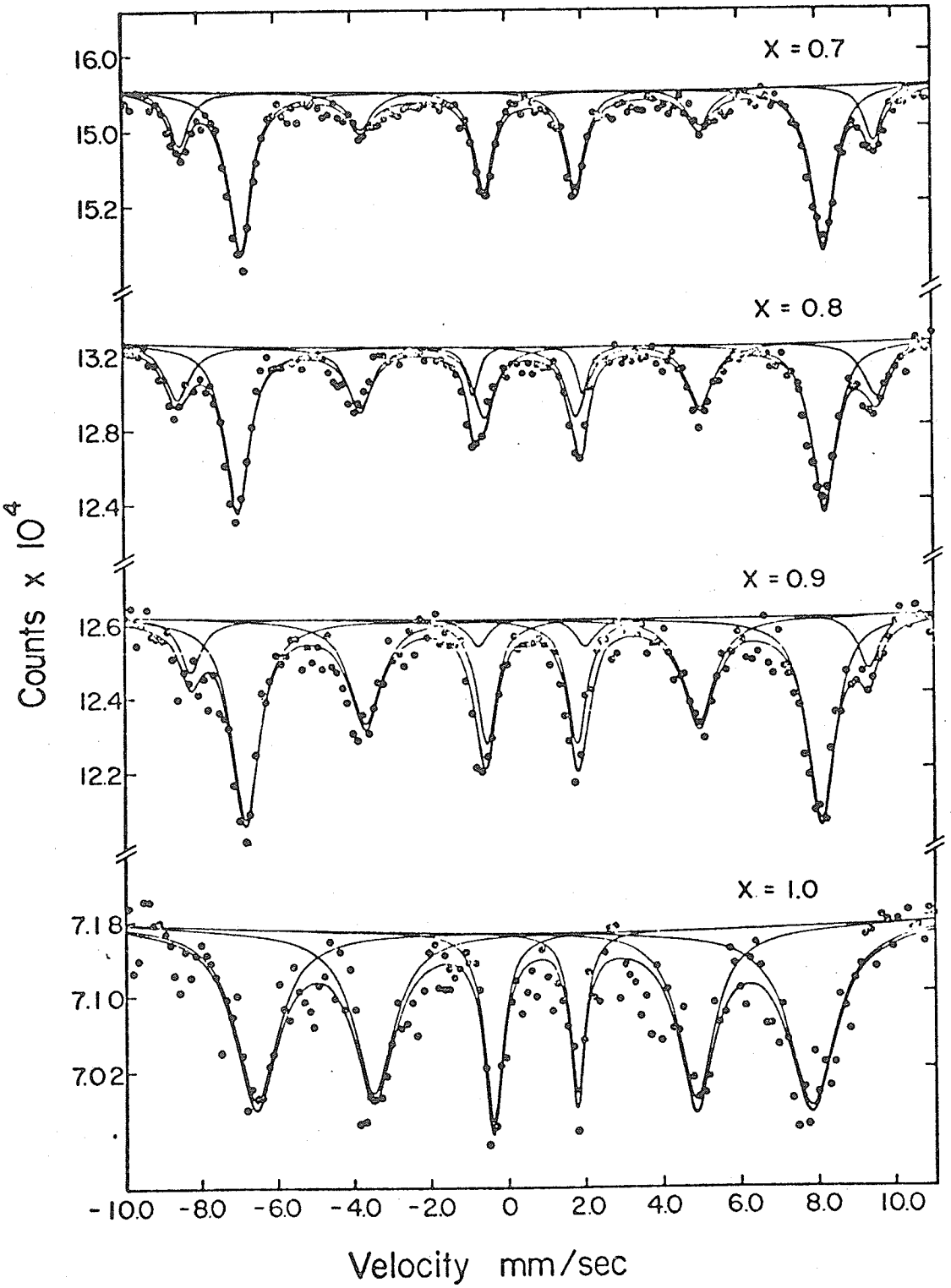

Fig. 57b. Mössbauer spectra of $Zn_xNi_{1-x}Fe_2O_4$ at 7° K with an external field of 50 kOe parallel to the direction of propagation of the ray. The solid curves are the computer fits.

Table XX. Results of Data Analysis based on Spectra of Ni-Zn Ferrites as shown in Figs. 56a and 56b.

X	H_{eff}(A)	H_{eff}(B)	I.S.(A)	I.S.(B)	½eqQ(A)	½eqQ(B)	Γ (A)	Γ (B)
0	511 ± 5	553 ± 5	0.60 ± 0.01	0.72 ± 0.01	-0.009 ±0.004	-0.007 ±0.004	0.50 ± 0.01	0.48 ± 0.01
0.1								
0.2	510	531	0.59 ± 0.01	0.69 ± 0.01	-0.004 ±0.006	-0.006 ±0.006	0.44 ± 0.02	0.63 ± 0.03
0.3	511	530	0.54 ± 0.01	0.64 ± 0.01	-0.027 ±0.007	0.008 ±0.005	0.48 ± 0.04	0.61 ± 0.02
0.4	509	523	0.55 ± 0.03	0.58 ± 0.03	-0.07 ±0.02	0.02 ±0.01	0.43 ± 0.04	0.55 ± 0.03
0.5	504	521	0.57 ± 0.05	0.62 ± 0.05	-0.07 ±0.03	-0.01 ±0.01	0.55 ± 0.10	0.58 ± 0.05
0.6	505	517	0.55 ± 0.05	0.52 ± 0.05	-0.14 ±0.02	0.01 ±0.01	0.49 ± 0.03	0.52 ± 0.04
0.7	505	512	0.54 ± 0.05	0.54 ± 0.05	-0.24 ±0.01	0.002 ±0.004	0.35 ± 0.06	0.56 ± 0.02
0.8	507	514	0.54 ± 0.05	0.59 ± 0.05	-0.17 ±0.04	0.016 ±0.003	0.27 ± 0.02	0.59 ± 0.01
0.9	508	489	0.62 ± 0.05	0.60 ± 0.05	-0.01 ±0.05	0.033 ±0.006	0.17 ± 0.02	0.86 ± 0.03
1.0	-	454	-	0.67 ± 0.02	-	0.03±0.02	-	1.30 ± 0.07
1.0†	-	486	-	0.65 ± 0.01	-	0.005±0.003	-	0.81 ± 0.01

† done at 4.2°K

Table XXI. Results of Data Analysis based on Spectra of Ni-Zn Ferrites as shown in Fig. 57a and 57b.

X	$H_{eff}(A)$	$H_{eff}(B)$	I. S. (A)	I. S. (B)	$\frac{1}{2}eqQ(A)$	$\frac{1}{2}eqQ(B)$	$\Gamma_{1,6}(A)$	$\Gamma_{1,6}(B)$	$\Gamma_{2,5}$	Area(A) / Area(B) Th.	Area(A) / Area(B) Expt'l	θ_{YK} ††
0.2	558 ± 5	485 ± 5	0.56 ± 0.01	0.65 ± 0.01	-0.004 ±0.006	0.01 ±0.01	0.42 ± 0.02	0.61 ± 0.03	0	0.67	0.61 ± 0.10	0
0.3	559	481	0.57	0.68	-0.01 ±0.01	0.01 ±0.01	0.44 ± 0.02	0.59 ± 0.01	0	0.54	0.51 ± 0.03	0
0.4	559	472	0.56	0.69	0.01 ±0.01	0.008 ±0.004	0.41 ± 0.02	0.61 ± 0.01	0	0.43	0.39 ± 0.03	0
0.5	555	466	0.57	0.68	0.01 ±0.01	-0.002 ±0.005	0.42 ± 0.04	0.60 ± 0.01	0	0.33	0.33 ± 0.03	0
0.6	559	466	0.55	0.67	0.00 ±0.02	-0.006 ±0.004	0.45 ± 0.05	0.63 ± 0.03	0.32 ± 0.13	0.25	0.24 ± 0.05	18°±5°
0.7	560	470	0.54	0.67	0.01 ±0.04	0.003 ±0.004	0.55 ± 0.05	0.71 ± 0.02	1.01 ± 0.12	0.18	0.22 ± 0.05	32°±5°
0.8	564	472	0.54	0.62	-0.03 ±0.03	0.002 ±0.007	0.76 ± 0.08	0.84 ± 0.03	0.80 ± 0.05	0.11	0.23 ± 0.05	59°±5°
0.9	547	465	0.60	0.66	0.04 ±0.03	-0.005 ±0.009	0.63 ± 0.11	0.84 ± 0.03	1.15 ± 0.06	0.05	0.12 ± 0.05	52°±10°
1.0	-	446	-	0.67	-	0.02 ±0.02	-	1.33 0.11	1.16 ± 0.11	0	0	59°±15°

†† Calculated from lines 1,2 or 5,6.

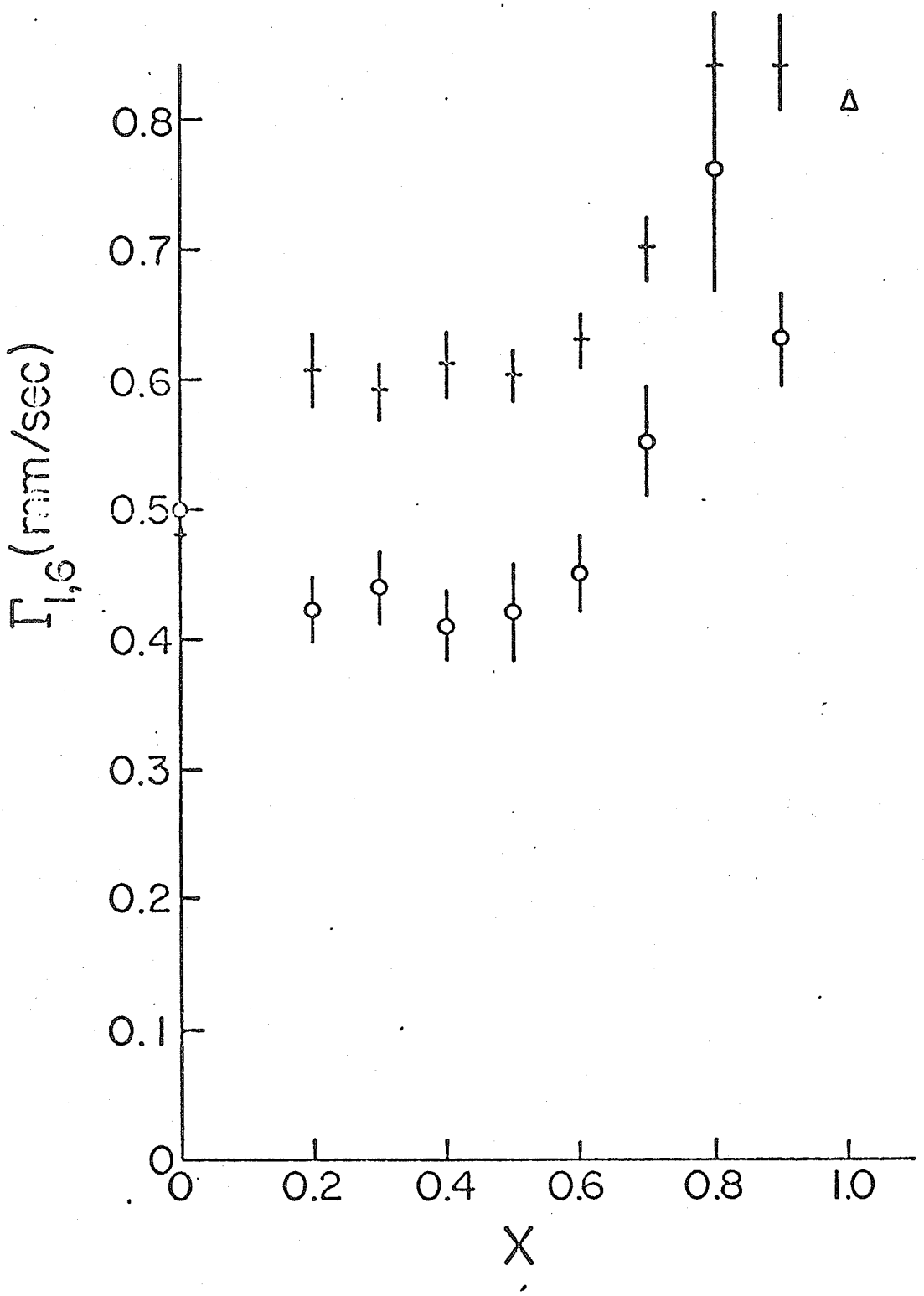

Fig. 58. Outermost line width vs. X values. (o) represents data corresponding to the A-site at 7° K, (+) B-site at 7° K and (Δ) B-site at 4.2° K.

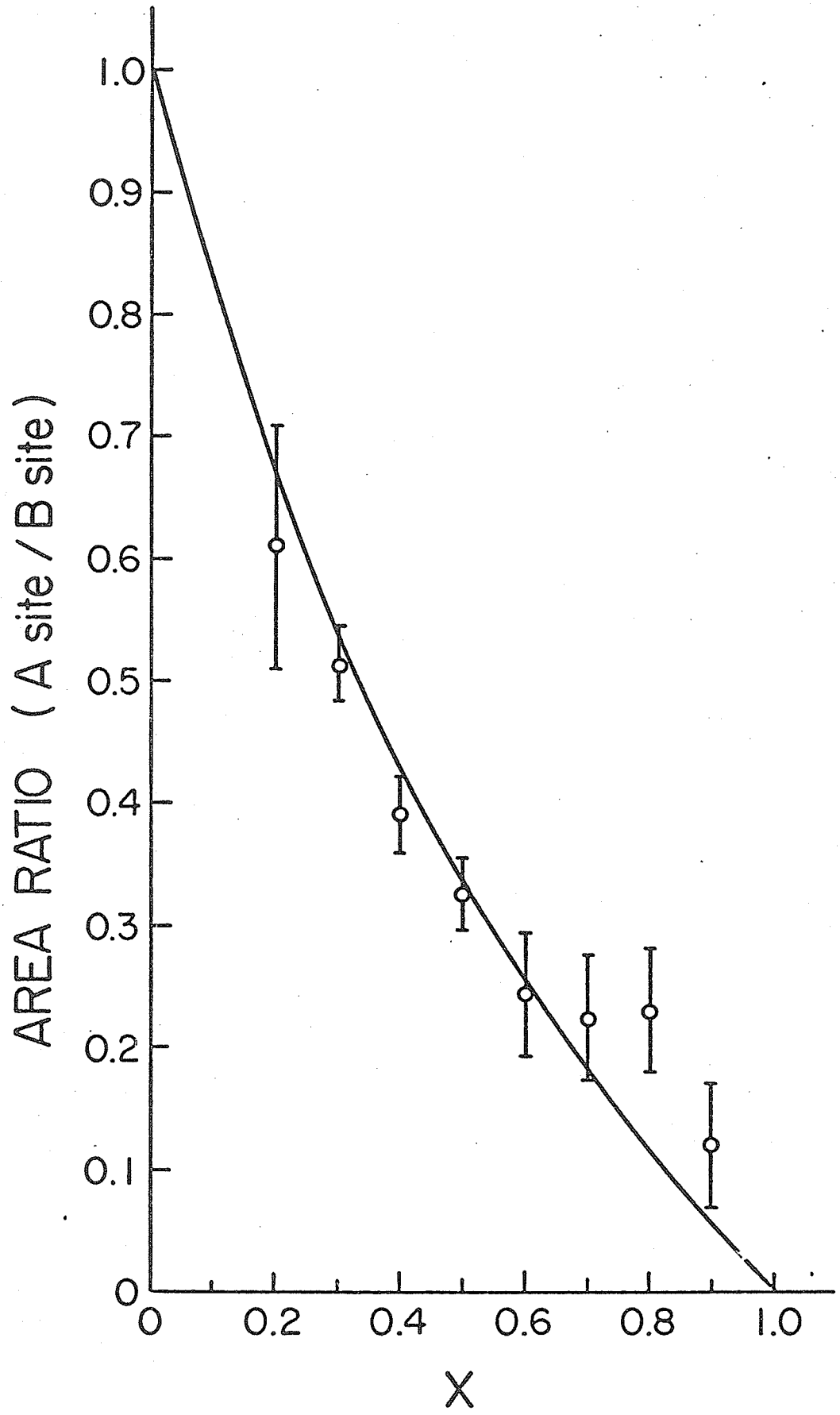

Fig. 59. Area ratio between A-site and B-site vs. X values. (o) represents experimental data and the solid curve is calculated based on the chemical formula $(Zn_XFe_{1-X})[Ni_{1-X}Fe_{1+X}]O_4$.

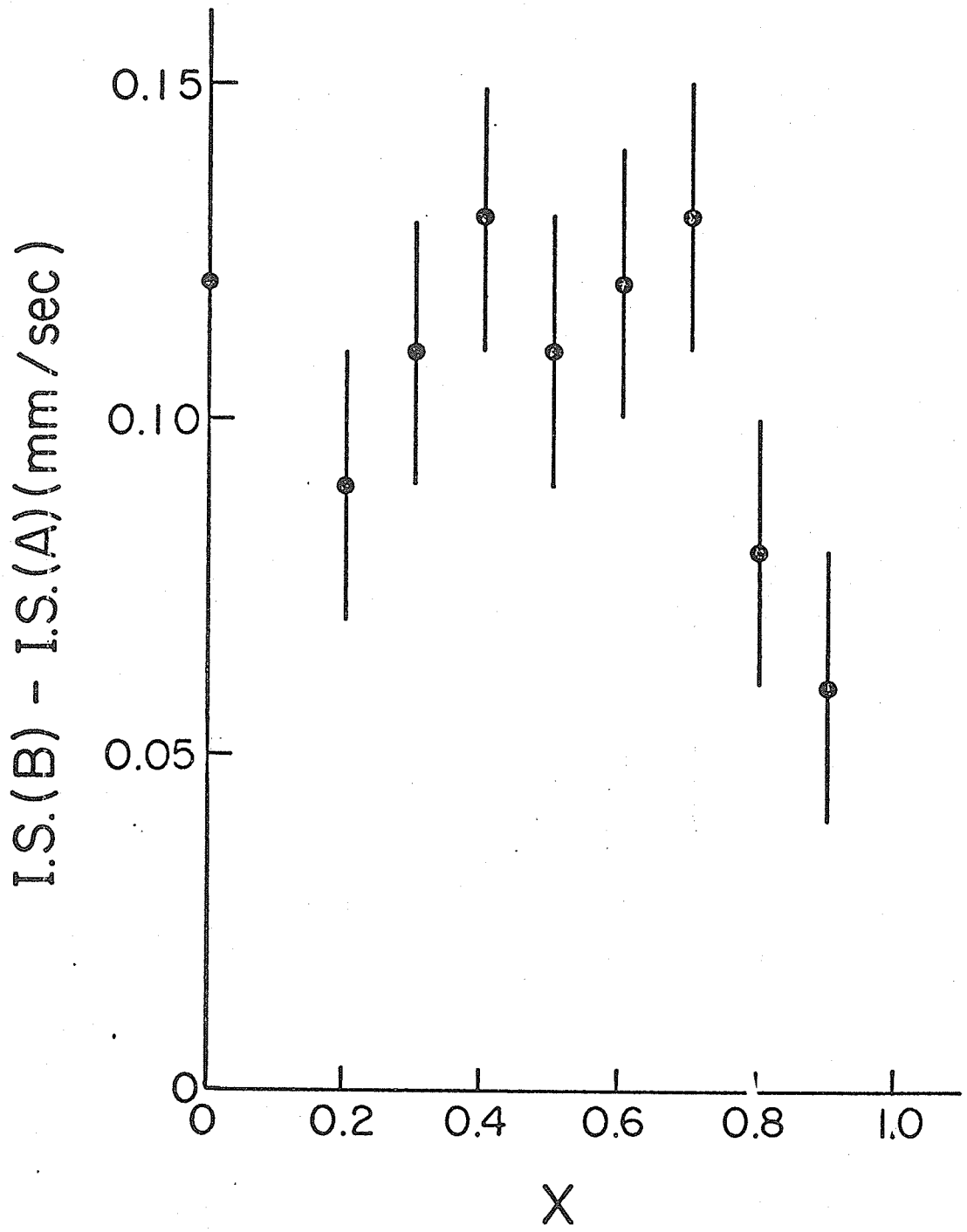

Fig. 60. Differential isomer shift vs. X values.

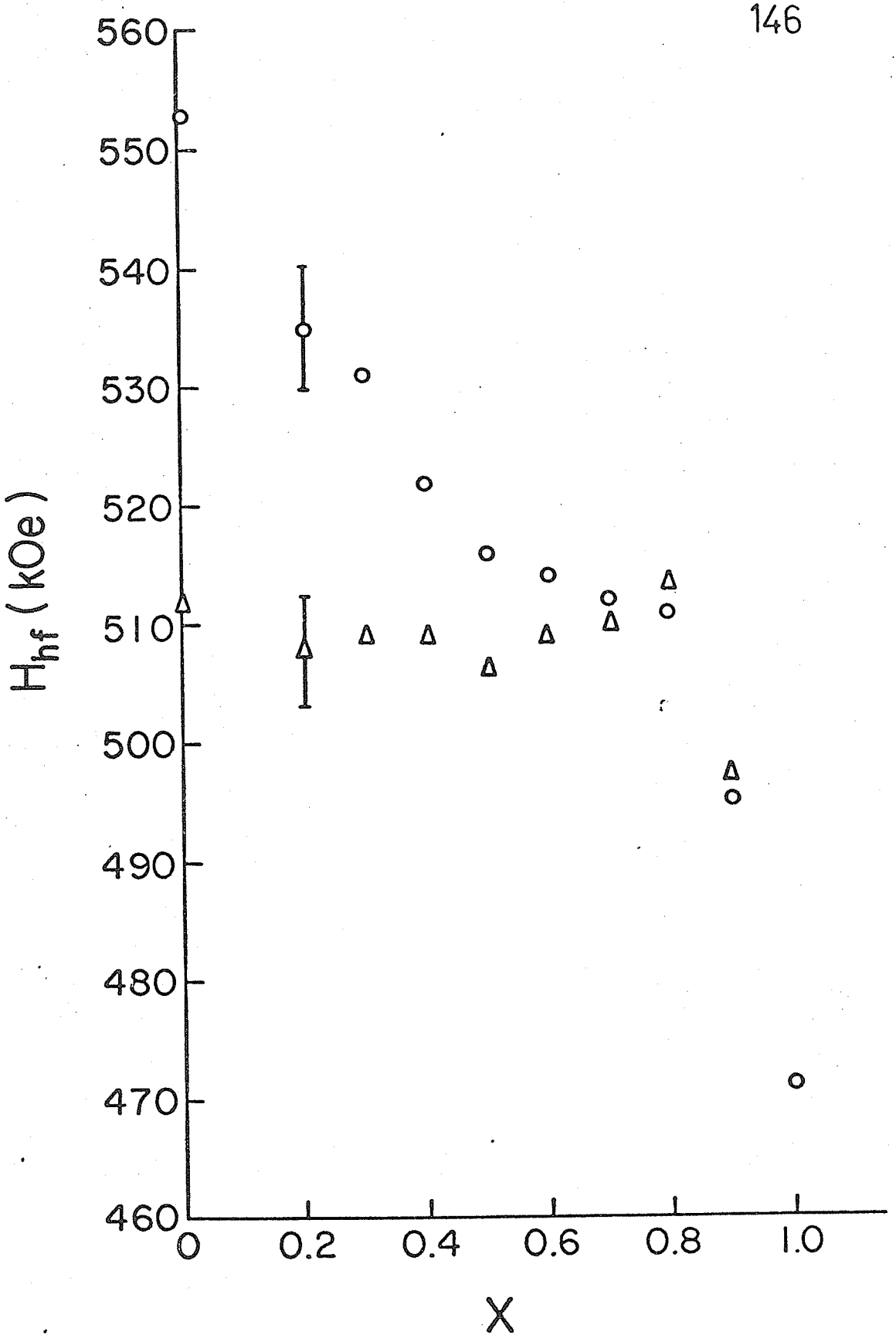

Fig. 61. Hyperfine fields derived from Fig. 57a and b. (o) represents data corresponding to B-site and (Δ) A-site.

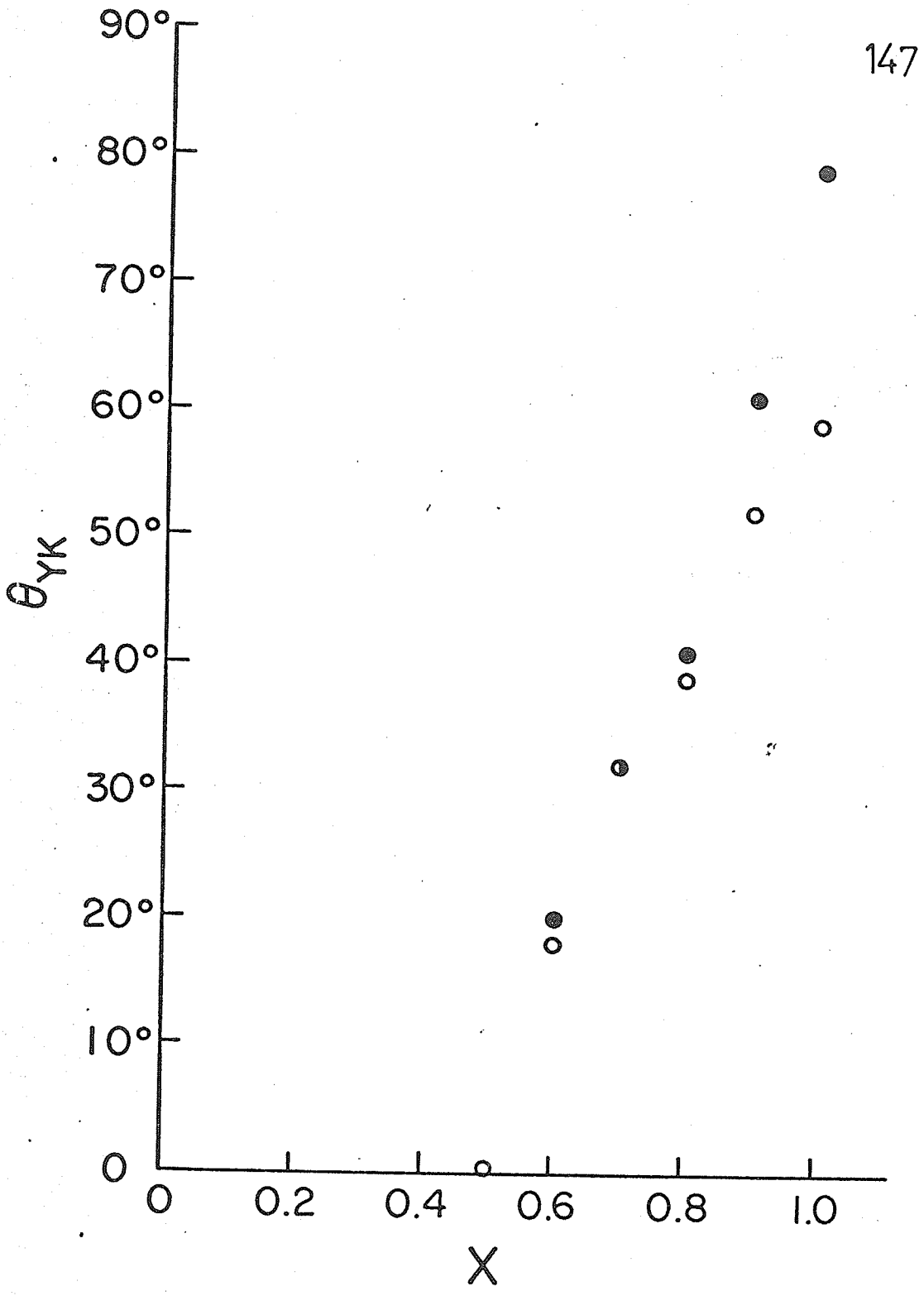

Fig. 62. Yafet-Kittel angle vs. X values. (o) represents results obtained through equation (2) and (●) through equation (3).

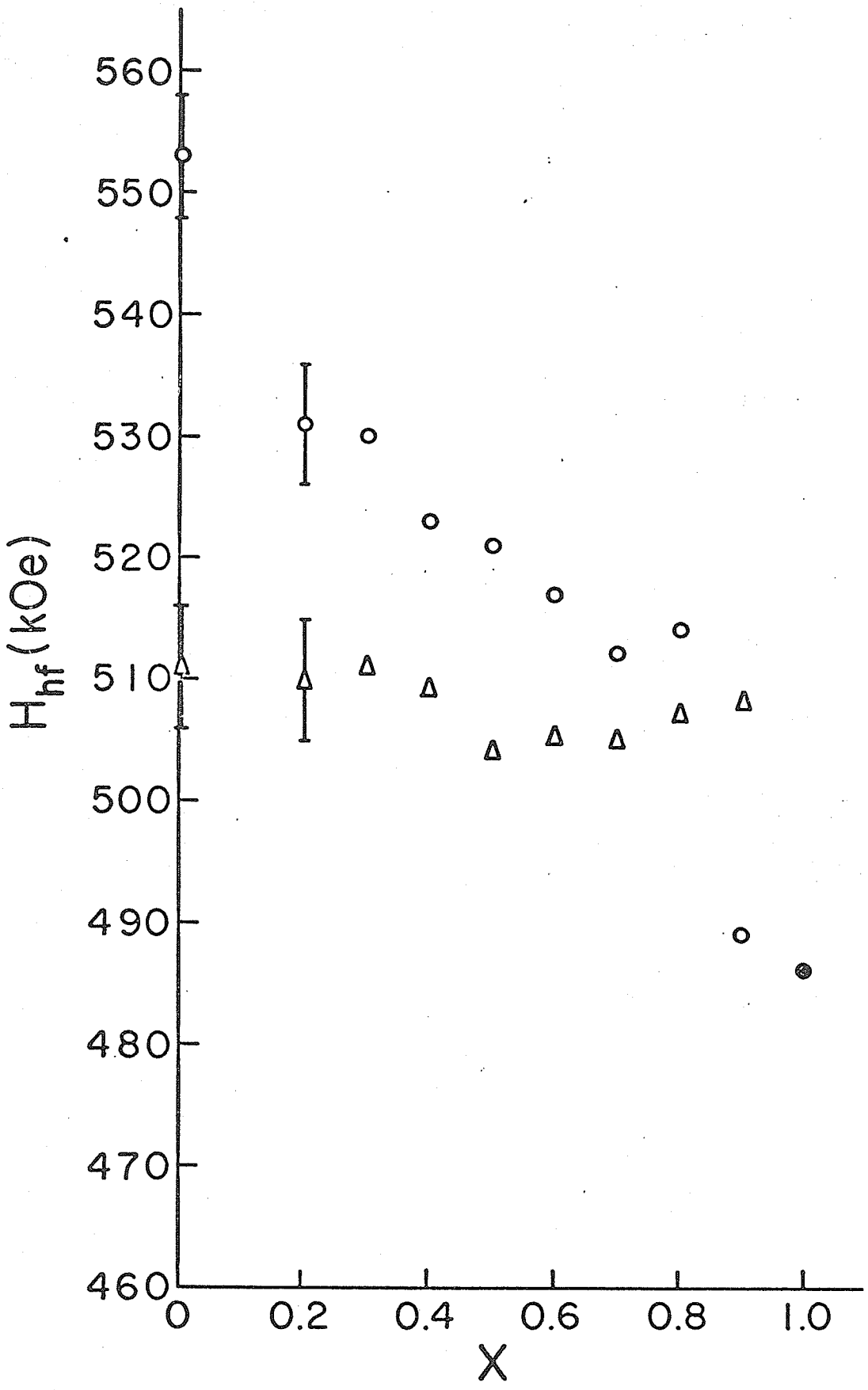

Fig. 63. Hyperfine fields derived from Fig. 56a and b. (o) represents data corresponding to B-site at 7° K, (●) B-site at 4.2° K and (Δ) A-site at 7° K.

from the applied field spectra shown in Fig.57. The angles have been derived from the data by two independent methods. In the first method, the angle is deduced from the relative integrated intensities of the lines. The intensities of the lines are related to θ by the following equations:

$$\begin{aligned} A_{1,6} &= \frac{9}{4}(1 + \cos^2\theta) \\ A_{2,5} &= 3\sin^2\theta \\ A_{3,4} &= \frac{3}{4}(1 + \cos^2\theta) \end{aligned} \qquad (1)$$

We have evaluated the angle θ from the following relationship:

$$\theta = \arcsin\left[1.5\,(I_{2,5}/I_{1,6})/\,(1 + 3I_{2,5}/4I_{1,6})\right] \qquad (2)$$

In the second method, we have used the relationship in the following equation, which was also used by Chappert and Frankel [66] in a Mössbauer study of spin canting in $NiFe_2O_4$ and $NiFe_{2-X}Cr_XO_4$:

$$\theta = \arccos\left(H_n^2(B) - H_{ext}^2 - H_{hf}^2(B)/\,2\,H_{ext}H_{hf}(B)\right) \qquad (3)$$

where $H_n(B)$ is the hyperfine field of the B site Fe^{3+} ions in the presence of an external field and is given by

$$\vec{H}_n(B) = \vec{H}_{hf}(B) - \vec{H}_{ext} \qquad (4)$$

$H_{hf}(B)$ is the hyperfine field at the B site Fe^{3+} ions in zero external field and H_{ext} is the external field. As seen in Table XXII,

Table XXII. Average Yafet-Kittel Angles for Ni-Zn Ferrites.

x	$\bar{\theta}_{yK}(B)$ (Equation 2)	$\bar{\theta}_{yK}(B)$ (Equation 3)
0→0.5	0	0
0.6	18° ± 5°	20° ± 5°
0.7	32° ± 5°	32°
0.8	39° ± 5°	41°
0.9	52° ± 10°	61°
1.0	59° ± 15°	79°

there is excellent agreement between the angles deduced from equations 2 and 3.

4.4 DISCUSSION

The chemical compositions lattice constants and magnetic properties data serve mainly to establish the relevance of the present study to previous ones. In the main, the Ni-Zn ferrites of this study are comparable with the ferrites used in previous studies. The complete delineations of the physical properties serve the further purpose of permitting other investigations to easily test the important conclusions of this study.

Our main concern in this discussion, however, is with

the cation distributions, magnetic structures, and their implications for local-molecular-field models and exchange interactions in disordered spinel ferrites. The remainder of our discussion will be devoted to these topics. First of all, as seen in Fig.59 and Table XXI where corrections due to slight Zn evaporation have not been made, excellent agreement is obtained between the experimental integrated intensity ratios of the A and B site Fe^{57} spectra and those calculated on the basis of the cation distribution $(Fe_{1-X}Zn_X)[Ni_{1-X}Fe_{1+X}]O_4$. Since these measurements were made on thin absorbers at 7^{o} K, corrections for finite thicknesses and differences in recoilless fractions are negligible. Previous Mössbauer studies on the spinel ferrites $NiFe_2O_4$ [79], Fe_3O_4 [86], γ-Fe_2O_3 [87-88] and $LiFe_5O_8$ [87] have all shown $f_A/f_B \cong 1.0$ at 4.2 K. This is the first time that the cation distribution has been proven to be $(Fe_{1-X}Zn_X)[Fe_{1+X}Ni_{1-X}]O_4$ in Nickel-Zinc Ferrites for all values of X between 0 and 1. This result permits a consideration of the local magnetic properties in terms of the statistics of the cation distribution to be undertaken with confidence.

None of the previous Mössbauer measurements have succeeded in fully resolving the A and B site pattern at several values of X, as has been done in the present study. Most of the data in this study are therefore not directly comparable with that of previous ones. The two most extensive Mössbauer studies on Ni-Zn Ferrites have been those of Goldanskii et al.[77] and Daniels and Rosencwaig [78].

Although the workers in reference [78] took exception to the dependence of H_{hf} on X as determined by Goldanskii, they did not prove the results of Goldanskii *et al.* to be erroneous since certain unproven constraints were imposed upon the data analysis to obtain the contrary results. We have proven in the present study that indeed Goldanskii *et al.* were incorrect and that the B-site hyperfine field decreases faster than the A-site hyperfine field at 7^{o} K. In general, there is good agreement between the present study and that of [78]. There are some important differences, however, in the conclusions regarding the linewidth, isomer shift and hyperfine field variations as a function of X.

From Fig.9, it is clear that the relative variation in the isomer shifts for $0 \leq X \leq .6$ is not as great as that found in [78]. The differential isomer shift [I.S.(A) − I.S.(B)] is essentially constant within experimental error up to $X \cong 0.7$. There are apparently greater variations for $X > 0.7$, though still not as great as those seen by the workers in [78]. We believe the variations for $X > 0.7$ to be of less significance than those for $X \leq 0.7$ since the lines have become seriously broadened. While there is agreement between the two studies that the B-site hyperfine field decreases faster than the A-site field, the rates of decrease and the cross-over points are quite different. From the applied field spectra, which is the most reliable for studying the variation in hyperfine fields, it is concluded (cf. Fig.61) that the B-site

field is larger than the A-site field up to $X \cong .7$ and is only slightly smaller than the A-site field for $X > 0.7$, the difference being within the experimental error and therefore of little significance. The cross-over point found in [78] at 77° K was at $X = 0.4$ and the B-site field was smaller than the A-site field by almost 20 kOe at $X = 0.6$. We believe the variations in the two sets of data to be due primarily to the difference in the temperatures at which the measurements were made. While the effect of variations in the reduced temperature, $T/T_N = T_R$, at 77° K was claimed in [78] to be negligible, this is not precisely correct since T_R varies between .13 and .18 for $0.4 \leq X \leq 0.6$ at 77° K compared to a variation of $.007 \leq T_R \leq .01$ at 7° K. The poorer resolution of the spectra in [78] is also expected to account for some of the differences.

Of somewhat greater importance since it relates to the interpretation of the Mössbauer data in terms of a local-molecular-field model is the variations in linewidths. Our results do not agree with those found in [78] that the A-site pattern has a significantly larger linewidth at $X = 0$ than the B-site pattern; at no value of X is the A-site linewidth, Γ_A, greater than Γ_B. However, there is a difference in the use of the term linewidth; the workers in [78] use the "average" linewidth of a single pattern whereas we are using the linewidths of the outermost lines. It has been shown [89] that the widths at outermost lines (1 and 6) are 6 times more

sensitive than those of the innermost lines (3 and 4) to fluctuation effects in the magnitudes of the hyperfine field, whereas the widths of all of the lines are equally sensitive to variations in the quadrupole coupling constant. The previous study has therefore over-estimated the relative importance of cation disorder on fluctuations in the A and B site hyperfine fields. The broadening of the B-site lines at 7° K in $NiFe_2O_4$ due to the different values of $e^2qQ(3\cos^2\theta - 1)$ is apparently greater than any broadening of the A-site lines as a result of local variations in the $Fe^{3+}(A)$-O^{2-}-Me(B) exchange interactions. The results of the present study are supported by recent Mössbauer measurements on $LiFe_5O_8$ [90] in which the outermost A-site linewidth is smaller than the B-site linewidth even though there is substantial disorder on the B-site, no disorder on the A-sites and the quadrupole splitting of the B-site pattern is very small. It is also to be noted that the linewidths reported in [78] at 77° K for $0.4 \leq X \leq 0.7$ are about four times larger than those found in the present study.

One surprising result is the rather large deviations between the <u>average</u> canting angles of the <u>average B-site spin moments</u>, determined using neutron diffraction, and the <u>average</u> canting angle of the B-site Fe^{3+} spin moments, determined in the present study using Mössbauer resonance. While the doubtful could raise questions concerning the significance of these differences for angles determined from the Mössbauer spectra on the basis of the

relative intensities of lines 1 and 2 (5 and 6) because of possible saturation effects, the fact that the same variations are obtained from angles deduced from the magnitudes of $H_n(B)$ and $H_{hf}(B)$ definitely establishes these differences as being real. There is, in fact, an obvious difference (as implied above) in the meaning of angles determined by the two techniques, aside from any commitment to the details of the three sub-lattice model used in the neutron diffraction study. From the neutron diffraction measurement one determines the average B-site canting angle, $\bar{\theta}_{YK}$, which includes some weighted sum of the average canting angles of the Ni^{2+} spins, $\bar{\theta}_{YK}(Ni)$ and of the Fe^{3+} spins, $\bar{\theta}_{YK}(Fe)$, i.e. $\theta_{YK}^{ND}(B) = \bar{\theta}_{YK}(B) = C_1\bar{\theta}_{YK}(Fe) + C_2\bar{\theta}_{YK}(Ni)$ where θ_{YK}^{ND} is the canting angle determined using neutron diffraction. The canting angle $\bar{\theta}_{YK}$ determined from the Mössbauer data corresponds to the average canting angle of Fe spins only, i.e. $\bar{\theta}_{YK}^{ME}(B) = \bar{\theta}_{YK}(Fe)$, where $\bar{\theta}_{YK}^{ME}$ is the canting angle determined using Mössbauer spectroscopy.

The smaller value of $\bar{\theta}_{YK}(Fe)$ compared to $\bar{\theta}_{YK}(B)$ can be qualitatively understood on the following basis: since the strength and sign of the B-B exchange interactions relative to the A-B exchange interactions determine the canting angle [91] and since it is also known that the $Fe^{3+}(B)$-$Fe^{3+}(A)$ exchange interactions are three times larger than the $Ni^{2+}(B)$-$Fe^{3+}(A)$ interactions [65] and in addition that the $Fe^{3+}(B)$-$Fe^{3+}(B)$ interactions are ferromagnetic [65, 69, 92], it follows that $\bar{\theta}_{YK}(Ni)$ will in

general be greater than $\bar{\theta}_{YK}(Fe)$. Both the antiferromagnetic $Fe^{3+}(B)$-$Fe^{3+}(A)$ and ferromagnetic $Fe^{3+}(B)$-$Fe^{3+}(B)$ exchange interactions favor a collinear parallel arrangement of the B-site spins. The possibility that the hyperfine field directions are not collinear with the local spin moments need not be given serious consideration for the Fe^{3+} ion, which has little or no orbital contribution to its magnetic moment in the nickel-zinc ferrites.

While the above explanation accounts qualitatively for the relative magnitudes of $\bar{\theta}_{YK}(B)$ and $\bar{\theta}_{YK}(Fe)$ there are still some further points to be considered regarding the magnitudes and precise interpretations of these angles.

If it is true that $\bar{\theta}_{YK}(Ni)$ is different from $\bar{\theta}_{YK}(Fe)$, then the three sublattice model of Satya Murthy is correct only if the Ni and Fe atoms are <u>randomly distributed over the two B-site magnetic sublattices</u>. In this case, the two B magnetic sublattices, B_1 and B_2, will have equal moments and the net B moment will be collinear with the A-site moment. The angle θ between the hyperfine field and external field directions will therefore be equal to $\bar{\theta}_{YK}(B)$, which is not the case. On the other hand, if the Fe^{3+} and Ni^{2+} ions are not randomly distributed on B_1 and B_2, then the moments of B_1 and B_2 will not be equal and their net moment will not be parallel to the A-site moment. In this case the angle between the external field and the hyperfine field directions, θ is not equal to $\bar{\theta}_{YK}(B)$, as observed. This spin arrangement and the resulting angles are depicted schematically in Fig.64. The resultant

magnetization, which lies along the external field direction, is neither parallel to the A-site or B-site spin moments and the two angles, $\overline{\theta}_{Fe}(B)$ and $\overline{\theta}_{Fe}(A)$, must be determined from the Mössbauer data. The analysis of the Mössbauer spectra of $NiCr_{1.7}Fe_{0.3}O_4$ in an external magnetic field was also carried out using a similar spin arrangement. That the above spin arrangement is indeed the correct one for $(Fe_{1-X}Zn_X)[Ni_{1-X}Fe_{1+X}]O_4$ is indicated by the very large widths for lines 2 and 5 relative to lines 1 and 6 and the fact that the widths increase as a strong function of X even though the widths of lines 1 and 6 are only weakly sensitive to changes in X. This is in addition to the very compelling fact that $\overline{\theta}_{YK}(B) \neq \overline{\theta}_{Fe}(B)$. If there is a single angle θ, the widths of lines 2 and 5 should never be greater than those of lines 1 and 6, yet from Table XXI we see that $\Gamma_{2,5}$ is at least as large as $\Gamma_{1,6}$. The lines are also asymmetric indicating again contributions from two or more different lines. For the spin arrangement in $Ni_{1-X}Zn_XFe_2O_4$, at least for large values of X, we prefer that depicted in Fig. 64.

The relatively narrow widths of the Mössbauer spectra for large X values and the faster rate of increase in the A-site linewidths are in qualitative agreement with the predictions of a local molecular field model. What is surprising though is the decrease in the magnitude of the hyperfine field at the B-site Fe^{3+} ion even at 7^{o} K. This result cannot be accounted for on the basis of a local molecular field model. We believe

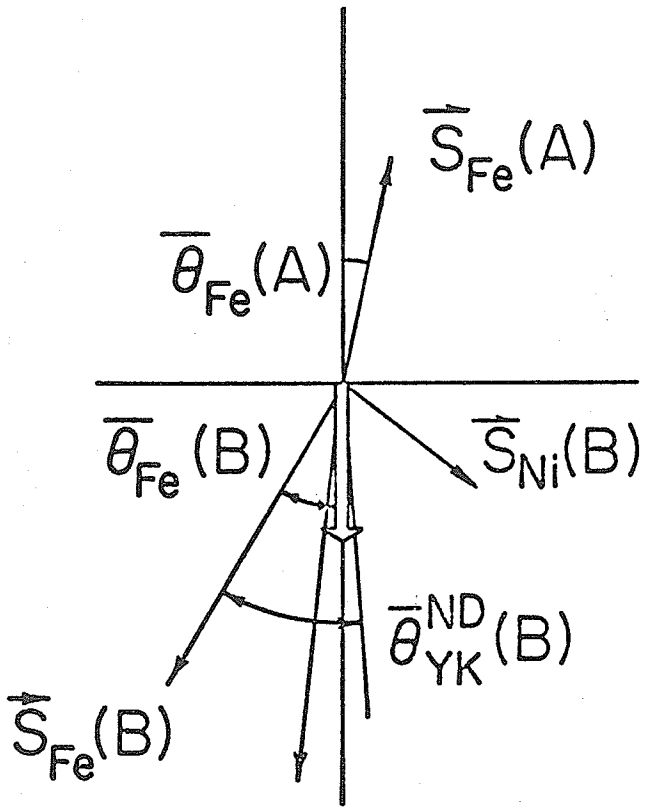

Fig. 64. Schematic diagram of spin arrangement of $Zn_XNi_{1-X}Fe_2O_4$ for X 0.5.

the decrease to be due to a change in the supertransferred hyperfine interactions [93]. This decrease can be understood as resulting from a decrease in the A to B spin transfer as the Fe^{3+} ions are replaced by Zn^{2+} ions. Note that in Fig.61 the decrease is linear for $X \leq 0.5$ but not for $X > 0.5$ and this is also the X value at which the canting of the Fe spins becomes observable. It is reasonable to suspect that this nonlinearity is due to a change in the B-B supertransferred hyperfine interactions as a consequence of the canting of the Fe spins in the

B-sites. From the linear portion, $\Delta H_{STHF}(AB)$ per Zn ion substitution is $\sim$ 12 kOe which agrees well with other published results [87, 89, 79, 90] (20 kOe in $LiFe_5O_8$; 12 kOe in $CuFe_2O_4$; 10 kOe in $NiFe_2O_4$; 17 kOe in $Li_{1.2}Fe_{4.6}Sb_{0.2}O_8$).

From overlap considerations, it is likely that the B-B spin transfer processes are important but unfortunately in this case the Fe^{3+}-O-Fe^{3+} linkage angles are 90^o and very little is known about the spin transfer processes.

V. CONCLUSIONS

5.1 SUMMARY

The NMR spectra together with the high value and thermal dependence of the conductivity at low temperature suggest that the compound $La_{1-X}Pb_XMnO_3$ with $0.26 \leq X \leq 0.44$ is indeed metallic-like and should be described adequately with a conventional band theory. This is further supported by the Mössbauer study on the Fe^{57} doped samples whose hyperfine fields exhibit a behavior similar to that of an alloy with impurity, and can be explained by the concept of d-electron core-polarization from a narrow d-band. An interpretation based on the concept of a " Supertransferred hyperfine field " does not seem to give a consistent explanation in this case. The rapid decrease of the magnetization near the Curie temperature which was interpreted as the collapse of the " Double-exchange " d-band becomes less obvious as the iron substitution increases. This suggests the presence of some other exchange mechanism. This idea is supported by the NMR results which show some electron localization at the Mn^{3+} and Mn^{4+} ion sites due to the Fe substitution. The Mössbauer spectra with an external field and the magnetization measurements indicate that the spins of Mn and Fe^{3+} ions are antiparallel and this is consistent with the superexchange spin arrangement. In other words,

we have here a transition from a collective to a localized behavior.

The system $Ni_{1-X}Zn_XFe_2O_4$ is known to be an insulator with $\rho \sim 10^5$ ohm cm. The decrease of the hyperfine field of the B-site ions as a function of X is explicable in terms of the concept of a " Supertransferred hyperfine field ". The nonlinear decrease at high X values suggests that the canting of the Fe spin has an effect on the hyperfine field. From the area ratios obtained from the well resolved Mössbauer spectra, it has been shown for the first time that the cation distributions of this mixed ferrite follow the formula $(Zn_XFe_{1-X})[Ni_{1-X}Fe_{1+X}]O_4$ with $0 \leq X \leq 1$. Here the symbol (...) denotes ions in the A-sites and [...] the B-sites.

5.2 SUGGESTIONS FOR FURTHER WORK

(i) The Mössbauer and/or NMR study of $La_{1-X}Pb_XMn_{1-Y}Fe_YO_3$ with higher Fe concentration would provide an interesting topic for further research. As pointed out in the discussion section of Chapter III, at $Y \geq 0.45$ the compound is expected to be completely antiferromagnetic and thus the result may give new information on the transition "ferromagnetism $\leftrightarrow$ antiferromagnetism".

(ii) NMR spectra of Fe^{57} doped $(LaPb)MnO_3$ as a function of temperature would certainly furnish some information on the energy of the transition "localized $\leftrightarrow$ collective".

(iii) NMR study of doped $(LaPb)MnO_3$ with diamagnetic or other magnetic ions should provide information on the nature of the d-band.

(iv) The Mössbauer study of Sn^{119} doped $(LaPb)MnO_3$ should also be very informative because Sn^{119} does not have its own moment.

APPENDIX A

THERMODYNAMIC THEORY OF THE MAGNETIC TRANSITION

The transitions between ferromagnetism and paramagnetism and between antiferromagnetism and paramagnetism are considered to be phase transitions of the second kind. This means that at the transition point, not only the thermodynamic potentials of the two phases are equal, but also the first derivatives of the thermodynamic potentials are equal; the second derivatives, however, are not equal and have a discontinuity. The first derivatives include the entropy, volume, spontaneous magnetization, electric polarization etc and the derivatives of these quantities are the second derivatives which are specific heat, expansion coefficients, compressibility etc. We define an ordering parameter $J = \sigma_s/\sigma_o$ where σ_s is the specific spontaneous magnetization at the temperature in question and σ_o is the specific magnetization at 0^oK. According to Landan [17], near a phase transition point of the second kind, where J takes arbitrarily small values, the thermodynamic potentials $\Phi(P,T, J)$ can be expanded in a power series in J, i.e.

$$\Phi = \Phi_o + aJ^2 + bJ^4 + \cdots\cdots$$

(terms in odd powers of J are not included, since the expansion of a scalar function (Φ) in powers of a vector function (J) can

contain only terms of even degrees) Ginzburg [18] has included in this expression the magnetic-field energy JH due to an applied field H, i.e.

$$\Phi = \Phi_o + aJ^2 + bJ^4 - JH$$

From the condition for equilibrium, $\frac{\partial \Phi}{\partial J} = 0$, we get an equation for the description of the true magnetization of a ferromagnetic material near the Curie point

$$\alpha\sigma + \beta\sigma^3 = H$$

where σ is the specific magnetization that is measured experimentally and is equal to $\sigma_S + \sigma_i$, where σ_i is the specific true magnetization caused by the application of the field H; $\alpha = 2a/\sigma_o$ and $\beta = 4b/\sigma_o^3$. Therefore by plotting H/σ versus σ^2 as Fig.9a we can determine the Curie point accurately and at the same time the coefficients α and β which are of great importance from the theoretical point of view because the nature of their temperature dependency is determined by the structural peculiarities of the ferromagnetic material.

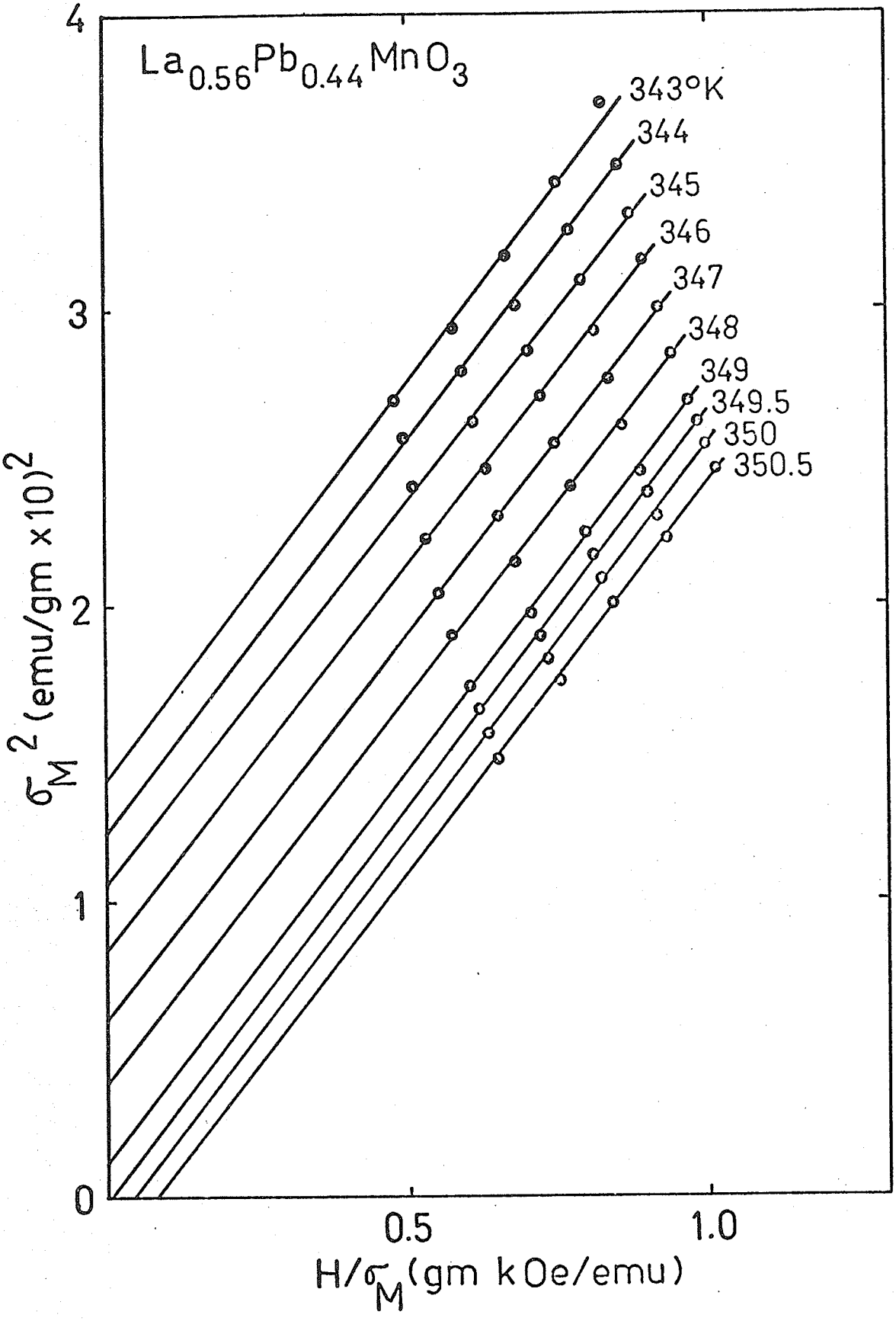

Fig. 9a. A typical plot of the magnetization using the thermodynamic method.

REFERENCES

1. C. Zener, Phys. Rev. 81, 440 (1950); ibid 82, 403 (1951).

2. V. M. Goldschmidt, Geochemische Verteilungsgesetze der Elemente VII, VIII (1927-28).

3. P. W. Anderson and H. Hasegawa, Phys. Rev. 100, 675 (1955).

4. H. A. Kramers, Physica 1, 182 (1934).

5. P. W. Anderson, Phys. Rev. 79, 350 (1950).
J. B. Goodenough and A. L. Loeb, ibid 98, 391 (1955).
J. C. Slater, Quart. Progr. Rept. Res. Lab. Electronics, MIT, July 15 p. 1; Oct 15, p. 1 (1953).
F. Keffer and T. Oguchi, Phys. Rev. 115, 1428 (1959).
J. Yamashita and J. Kondo, ibid 109, 730 (1958).
R. K. Nesbet, ibid 119, 658 (1960).
J. Kanamori, Phys. and Chem. Solids 10, 87 (1959).
J. B. Goodenough, ibid 6, 287 (1958).
J. Kondo, Prog. Theor. Phys. (Kyoto) 22, 41 (1959).

6. J. B. Goodenough, Phys. Rev. 100, 564 (1955).

7. R. K. Nesbet, Ann. Phys. (N.Y.) 4, 87 (1958).

8. P. W. Anderson, Phys. Rev. 115, 2 (1959).

9. G. H. Jonker and J. H. Van Santen, Physica 16, 337 (1950).
J. H. Van Santen and G. H. Jonker, ibid 16, 599 (1950).

10. P. G. de Gennes, Phys. Rev. 118, 141 (1960).

11. J. Volger, Physica 20, 49 (1954).

12. E. O. Wollan and W. C. Koehler, Phys. Rev. 100, 545 (1955).

13. Performed by B. J. Evans.

14. Performed by A. Sawatzky of the Whiteshell Nuclear Research Establishment, Pinawa, Manitoba.

14a. S. Foner, Rev. Sci. Ins. 30, 548 (1959).

14b. S. Akajs and G. R. Dunmyre, Phys. Stat. Sol. 21, 191 (1967).

15. P. Weiss and R. Forrer, Ann. Phys. (Paris) 5, 153 (1926).

16. K. P. Belov, Magnetic Transitions (Boston Technical Publishers, Inc., Cambridge, Mass.) Chapter III (1965).

K. P. Below and A. N. Goryaga, Fiz. Metal. i Metalloved. 2, 441 (1956).

17. L. D. Landau and E. M. Lifshitz, Statistical Physics (Addison-Wesley Publishing Co., Inc. Mass.) (1951).

18. V. L. Ginzburg, Zhur. E'ksp i Teor. Fiz. 17, 833 (1947).

19. J. S. Kouvel and M. E. Fisher, Phys. Rev. 136, A1626 (1964).

20. G. Gorodetsky, S. Shtrikman and D. Treves, Solid St. Comm. 4, 147 (1966).

21. D. O. Smith, Phys. Rev. 102, 959 (1956).

22. D. G. Howard, B. D. Dunlop and J. G. Dash, Phys. Rev. Lett. 15, 628 (1965).

23. D. C. Mattis, The Theory of Magnetism (Harper and Row Publisher, Inc., Ner York 1965) p. 235.

24. E. Collen and H. Collen, J. Appl. Phys. 36, 1140 (1965).

25. L. P. Kadanoff, W. Götze, D. Hamblen, R. Hecht, E. A. S. Lewis, V. V. Palciauskas, M. Rayl, J. Swift, D. Aspnes and J. Kane, Rev. Mod. Phys. 39, 395 (1967).

26. M. J. Oretzki and P. Gaunt, Canad. J. Phys. 48, 346 (1970).

27. C. W. Searle and S. T. Wang, ibid 47, 2703 (1969).

28. L. J. Van der Pauw, Philips Res. Rept. 13, 1 (1958).

29. S. T. Wang, Ph.D. Thesis, University of Manitoba (1970).

30. A. H. Morrish, The Physical Principles of Magnetism (John Wiley and Sons, Inc.) Chapter 4, (1965).

A. Abragam, The Principles of Nuclear Resonance (Oxford University Press, Oxford) (1961).

E. R. Andrew, Nuclear Magnetic Resonance (Cambridge University Press, Cambridge) (1956).

31. H. Zijlstra, Experimental Methods in Magnetism (John Wiley and Sons, Inc., New York) Vol. IX Chapter 6 (1967).

32. E. L. Hahn, Phys. Rev. 80, 580 (1950).

33. J. L. Synge and B. A. Griffith, Principles of Mechanics, 2nd ed. (McGraw-Hill Book Co., New York) p. 347 (1945).

34. H. Y. Carr and E. M. Purcell, Phys. Rev. 94, 630 (1954).

35. I. Solomon, Phys. Rev. 110, 61 (1958).

C. W. Searle and J. Davis, Phys. Rev. Lett. 27, 1380 (1971).

H. Abe, H. Yasuoka and A. Hirai, J. Phys. Soc. Japan 21, 77 (1966).

H. Yasuoka, H. Abe, M. Matsuura and A. Hirai, ibid 18, 1554 (1963).

J. P. Gordon and K. D. Bowers, Phys. Rev. Lett. 1, 368 (1958).

M. Weger, Thesis, University of California, Berkeley (1961) (Unpublished).

36. E. Suhl, Phys. Rev. 109, 606 (1958).

T. Nakamura, Prog. Theor. Phys. 20, 542 (1958).

37. R. F. Jackson, R. G. Scurlock, D. B. Utton and T. H. Wilmshurst, Phys. Rev. Lett. 11, 197 (1964).

38. J. Winter, Phys. Rev. 124, 452 (1961).

39. Suggested by P. D. Loly.

40. C. W. Searle and S. T. Wang, Canad. J. Phys. 48, 2023 (1970).

41. T. Van Peski-Tinbergen and A. J. Dekker, Physica 29, 917 (1963).

T. Kasuya, Prog. Theor. Phys. 16, 45 (1959).

P. G. de Gennes and J. Friedel, Phys. and Chem. Solids 4, 71 (1958).

A. J. Dekker, J. Appl. Phys. 36, 906 (1965).

42. P. W. Anderson, In Magnetism, Vol. I, edited by G. T. Rado and H. Suhl (Academic Press Inc., New York) p. 25.

43. A. M. Portis and R. H. Linquist, In Magnetism, Vol. IIA, edited by G. T. Rado and H. Suhl (Academic Press Inc., New York) p. 360.

44. A. C. Gossard, V. Jaccarino and J. P. Remeika, J. Appl. Phys. 33, 1187 (1962); Phys. Rev. Lett. 7, 122 (1961).

45. R. P. Feynman, R. B. Leighton and M. Sands, The Feynman Lectures on Physics, Vol. II p. 32-11.

46. G. Matsumoto, IBM J. Res. Develop. (1970).

47. S. V. Vonsovskii, Ferromagnetic Resonance (Perganon Press) p. 205.

48. R. L. Mössbauer, Z. Phys. 151, 124 (1958); Naturwiss 45, 538 (1958); Z. Naturforsch. 14a, 211 (1959).

G. K. Wertheim, Mössbauer Effect: Principles and Applications (Academic Press, New York and London, 1964).

H. Frauenfelder, The Mössbauer Effect (W. A. Benjamin, Inc. New York 1962).

V. I. Goldanskii and R. H. Herber, Chemical Applications of Mössbauer Spectroscopy (Academic Press, New York and London, 1968).

I. J. Gruverman, Mössbauer Effect Methodology (Plenum Press, New York).

49. J. G. Stevens and V. E. Stevens, Mössbauer Effect Data Index (Plenum Press, New York, 1969) Appendix C.

50. J. Owen and D. R. Taylor, Phys. Rev. Lett. 16, 1164 (1966); N. L. Huang, R. Orbach and E. Simanek, ibid, 17, 134 (1966); Phys. Rev. 156, 383 (1967).

51. L. R. Walker, G. K. Wertheim and V. Jaccarino, Phys. Rev. Lett. 6, 98 (1961).

52. G. A. Sawatzky, Ph.D. Thesis, University of Manitoba (1969).

J. M. D. Coey, Ph.D. Thesis, University of Manitoba (1971).

53. U. König, E. F. Bertaut, Y. Gros, M. Mitrikov and G. Chol, Solid St. Comm. 8, 759 (1970).

54. M. J. D. Powell, The Computer Journal 5, 147 (1962).

55. T. Kubo, A. Hirai and H. Abe, J. Phys. Soc. Japan 26, 1094 (1969).

56. G. Matsumoto, J. Phys. Soc. Japan 29, 615 (1970).

57. H. G. Andresen, Phys. Rev. 120, 1606 (1960).

58. G. Geschwind et al., Phys. Rev. 126, 1648 (1962).

59. T. Kubo, H. Yasuoka and A. Hirai, J. Phys. Soc. Japan 21, 812 (1966).

60. R. L. Streever, T. R. Aucoin and P. J. Caplan, Phys. and Chem. Solids 32, 519 (1971).

61. J. S. Kouvel, Phys. Rev. 102, 1489 (1956).

62. G. K. Wertheim, V. Jaccarino, J. H. Wermick and D. N. E. Buchanan, Phys. Rev. Lett. 12, 24 (1964); M. B. Stearns and S. S. Wilson, ibid 13, 313 (1964).

63. J. B. Goodenough, In Progress in Solid State Chemistry Vol. 5 edited by H. Reiss (Pergamon Press) p. 342.

65. K. Motida and S. Miyahara, J. Phys. Soc. Japan 28, 1188 (1970).

66. J. Chappert and R. B. Frankel, Phys. Rev. Letters 19, 570 (1967).

67. G. A. Sawatzky, F. van der Woude and A. H. Morrish, Phys. Letters, 25A, 147 (1967).

68. B. J. Evans, Proc. IV Symposium on Mössbauer Effect Methodology (1968) (Plenum Press, New York).

69. L. Cser, I. Dezsi, I. Gladkih, L. Keszthelyi, D. Kulgawczuk, N. A. Eissa and E. Sterk, Phys. Stat. Sol. 27, 131 (1968).

70. E. Wieser, V. A. Povitskii, E. F. Makarov and K. Kleinstück, Phys. Stat. Sol. 25, 607 (1968).

71. I. Nowick, J. Appl. Phys. 40, 872 (1969).

72. U. König, Y. Gros and G. Chol, Phys. Stat. Sol. 33, 811 (1969).

73. V. F. Belov, N. S. Ovanesyan, V. A. Trukhtanov, M. N. Shipko, E. V. Korneev, V. V. Korovushkin and L. N. Korablin, Zh. Eksp. Teor. Fiz. 59, 1484 (1970) (Sov. Phys - JETP 32, 810, 1971).

74. A. Rosencwaig, Can. J. Phys. 48, 2857 (1970).

75. V. C. Wilson and J. S. Kasper, Phys. Rev. 94, 1408 (1954).

76. N. S. Satya Murthy, M. G. Nater, S. I. Yousef, R. J. Begum and C. M. Srivastava, Phys. Rev. 181, 969 (1969).

77. V. I. Goldanskii, V. F. Belov, M. N. Devisheva and V. A. Trukhtanov, Sov. Phys. - JETP 22, 1149 (1966).

78. J. M. Daniels and A. Rosencwaig, Can. J. Phys. 48, 381 (1970).

79. G. A. Sawatzky, F. van der Woude and A. H. Morrish, Phys. Rev. 187, 747 (1969).

80. B. Boucher, R. Buhl and M. Perrin, Phys. Stat. Sol. 40, 171 (1970).

81. U. König, E. F. Bertaut, Y. Gros and G. Chol, Solid State Comm., 8, 759 (1970).

82. Schwarzkoff Microanalytical Laboratory, Woodside, New York, U. S. A.

83. C. Guilland and M. Roux, C. R. Acad. Sci., Paris, 229, 1133 (1949).

84. K. A. Piskarev, Bull. Acad. Sci., U.S.S.R. 23, 282 (1959).

85. J. G. Booth and J. Crangle, Proc. Phys. Soc. 79, 1271 (1962).

86. G. A. Sawatzky, F. van der Woude and A. H. Morrish, Phys. Rev. 183, 383 (1969).

87. B. J. Evans, Ph. D. Thesis, University of Chicago (1968).

88. D. R. Khalafalla, M. Sc. Thesis, University of Manitoba (1971).

89. B. J. Evans, J. Phys. Chem. Solids 29, 1573 (1968).

90. B. J. Evans and L. J. Swartzendouber, J. Appl. Phys. 42, 1628 (1971).

91. Y. Yafet and C. Kittel, Phys. Rev. 87, 290 (1952).

92. H. Bourdonnay, A. Bousquet, J. P. Cotton, D. Bribier, B. Farnonx, R. Fenillatre, B. Hennion, J. Jacquies, G. Jannink, R. Kahn, D. Mons, J. Mons, G. Posette, G. Perpy, L. Rouleau, J. P. Trotin and Mrs. Monssa, J. de Physique 32, C1-1182 (1971) and references therein.

93. E. Simanek, N. L. Huang and R. Orbach, J. Appl. Phys. 38, 1697 (1967).

94. A. H. Morrish, B. J. Evans, J. A. Eaton and L. K. Leung, Canad. J. Phys. 47, 2691 (1969).

95. L. K. Leung, A. H. Morrish and C. W. Searle, Canad. J. Phys. 47, 2697 (1969).

96. L. K. Leung, B. J. Evans and A. H. Morrish, Bull. Am. Phys. Soc. 15, 824 (1970).

97. P. Heller, Progress in Physics 30, 731 (1967)